

# Ion-channeling on nanostructured semiconductors

**Citation for published version (APA):**

Selen, L. J. M. (2001). *Ion-channeling on nanostructured semiconductors*. [Phd Thesis 1 (Research TU/e / Graduation TU/e), Applied Physics and Science Education]. Technische Universiteit Eindhoven.  
<https://doi.org/10.6100/IR544674>

**DOI:**

[10.6100/IR544674](https://doi.org/10.6100/IR544674)

**Document status and date:**

Published: 01/01/2001

**Document Version:**

Publisher's PDF, also known as Version of Record (includes final page, issue and volume numbers)

**Please check the document version of this publication:**

- A submitted manuscript is the version of the article upon submission and before peer-review. There can be important differences between the submitted version and the official published version of record. People interested in the research are advised to contact the author for the final version of the publication, or visit the DOI to the publisher's website.
- The final author version and the galley proof are versions of the publication after peer review.
- The final published version features the final layout of the paper including the volume, issue and page numbers.

[Link to publication](#)

**General rights**

Copyright and moral rights for the publications made accessible in the public portal are retained by the authors and/or other copyright owners and it is a condition of accessing publications that users recognise and abide by the legal requirements associated with these rights.

- Users may download and print one copy of any publication from the public portal for the purpose of private study or research.
- You may not further distribute the material or use it for any profit-making activity or commercial gain
- You may freely distribute the URL identifying the publication in the public portal.

If the publication is distributed under the terms of Article 25fa of the Dutch Copyright Act, indicated by the "Taverne" license above, please follow below link for the End User Agreement:

[www.tue.nl/taverne](http://www.tue.nl/taverne)

**Take down policy**

If you believe that this document breaches copyright please contact us at:

[openaccess@tue.nl](mailto:openaccess@tue.nl)

providing details and we will investigate your claim.

# **Ion-Channeling on Nanostructured Semiconductors**

PROEFSCHRIFT

TER VERKRIJGING VAN DE GRAAD VAN DOCTOR AAN  
DE TECHNISCHE UNIVERSITEIT EINDHOVEN, OP GEZAG  
VAN DE RECTOR MAGNIFICUS, PROF. DR. M. REM, VOOR  
EEN COMMISSIE AANGEWENZEN DOOR HET COLLEGE  
VOOR PROMOTIES IN HET OPENBAAR TE VERDEDIGEN  
OP DONDERDAG 14 JUNI 2001 OM 16.00 UUR

DOOR

**LOUIS JOANNES MARIA SELEN**

GEBOREN TE DÜSSELDORF

DIT PROEFSCHRIFT IS GOEDGEKEURD  
DOOR DE PROMOTOREN:  
PROF.DR. M.J.A. DE VOIGT  
EN  
PROF.DR. J.H. WOLTER

COPROMOTOR:  
DR. L.J. VAN IJZENDOORN

Druk: Universiteitsdrukkerij Technische Universiteit Eindhoven  
Ontwerp omslag: Jan Selen en Jan-Willem Luiten

CIP-DATA LIBRARY TECHNISCHE UNIVERSITEIT EINDHOVEN

Selen, Louis Joannes Maria

Ion-Channeling on Nanostructured Semiconductors / by Louis Joannes Maria Selen. -  
Eindhoven: Technische Universiteit Eindhoven, 2001. - Proefschrift.

ISBN 90-386-1779-8

NUGI 812

Trefw.: 3-5 verbindingen / channeling / ionenbundelanalyse / Monte-Carlo-methoden /  
nano-structuren / silicium

Subject headings: III-V-semiconductors / channeling / Monte-Carlo-methods / nanostruc-  
tures / Rutherford-backscattering / silicon

*Aan mijn ouders*





# Contents

1. Introduction	3
2. Evidence for strain in and around InAs quantum dots in GaAs from ion-channeling experiments	23
3. Ion-channeling for strain analysis in buried nano-films ( $< 6$ nm)	35
4. Planar ion-channeling on buried nano-films discriminates between ion-atom potentials	49
5. Planar ion-channeling measurements on buried nano-films	57
6. Lattice deformation in InAs/GaAs superlattices characterized by MeV ion-channeling	71
7. A channeling study of boron clusters in silicon	85
8. Transmitted ion energy loss distributions to detect cluster formation in silicon	97
Summary	111
Samenvatting	114
List of publications	117
Dankwoord	118
Curriculum Vitae	120



# 1. Introduction

## I General

This thesis describes the characterization of state of the art semiconductor structures by means of MeV ion-channeling in combination with Rutherford backscattering spectrometry (RBS). Usually, MeV ion-channeling is used to characterize films with a thickness of at least 20 nm by measuring angular scans of the crystal structure. The properties of the semiconductor structures presented in this thesis, quantum dots and nanometer thick buried strained films, are however governed by dimensions, which are typically about an order of magnitude smaller.

In this thesis work unorthodox interpretations of ion-channeling measurements have been successfully applied and innovative methods have been developed to characterize the lattice deformations in these semiconductor structures with MeV ion-channeling.

Different types of semiconductor structures will be presented first in this introduction. Furthermore, this chapter introduces the tools, which are needed to perform and understand the ion-channeling measurements. Finally, the ion-channeling technique is compared to X-ray diffraction (XRD) and transmission electron microscopy (TEM), which are two other techniques commonly used to characterize lattice deformations in semiconductor structures. In the remaining chapters of this thesis, the characterization of a number of semiconductor structures is presented in the form of articles, which have been or will be published in international scientific journals.

## II State of the art semiconductor structures

Semiconductors of the III/V group usually exhibit a direct band gap, which makes them favorable in the opto-electronic field for applications in photonic devices like laser diodes and light emitting diodes (LEDs). Furthermore, they find applications in electronic devices like high-electron-mobility transistors (HEMTs) [1]. Particularly interesting is that a great flexibility with respect to the wavelength tuning can be achieved, by applying ternary III/V alloys, like  $\text{Al}_x\text{Ga}_{1-x}\text{As}$  and  $\text{In}_x\text{Ga}_{1-x}\text{As}$ .

Si and Ge, which are the most commonly applied group-IV semiconductors, do not exhibit a direct band gap, and find most of their applications in electronic devices like SiGe metal-oxide-semiconductor modulation-doped field effect transistors (MOS-MODFETs), consisting of  $\text{Si}_{1-x}\text{Ge}_x/\text{Si}_{1-y}\text{Ge}_y$  heterostructures grown on a Si substrate [2], *npn* SiGe heterojunction bipolar transistors, where Ge is employed in the base [3], and *pn* tunnel junctions, which are applied in amorphous SiGe alloy solar cells [4].

Device structures based on III/V or IV semiconductor compounds, are typically grown by techniques such as molecular beam epitaxy (MBE) or chemical vapor deposition

(CVD). In the past decade, the development of these growth techniques and the demand for faster device structures based on III/V or IV semiconductor compounds, has led to continually smaller and low-dimensional structures. This development continuously proceeds, and characterization of the latest generation semiconductor structures with MeV ion-channeling poses interesting challenges.

An important step often used in the fabrication of Si semiconductor structures is ion implantation, which introduces dopants into the semiconductor material [5]. To obtain a higher switching speed, the dimensions of state of the art devices decrease by a factor 2 in size every 2-3 years. This also pushes the development of ion implantation techniques. For shallow junction formation, a decrease of the implantation energy is needed, which can be achieved by implantation of ion clusters [6, 7]. When the average implantation energy per dopant atom decreases, the top concentration of the implanted ions increases. When the top concentration exceeds the maximum concentration which is governed by the solid solubility, this leads to formation of clusters of the implanted ions, which destroy the homogeneity of the semiconductor crystal lattice and the device properties [8, 9]. An example of an implantation profile for boron implanted in Si is shown in Fig. 7.1. Since for ion cluster implantation the redistribution of energy of the fragments is not known exactly, the critical implantation dose plays an important role. It is therefore very interesting to investigate the possibility to determine the presence of dopant clusters by measuring the lattice deformations they induce.

In most of the semiconductor structures grown with MBE or CVD strain is involved due to lattice mismatch, which modifies the band gap and density of states of the charge carriers in the active region, and thereby the device properties [10–13]. Furthermore, the formation of dopant clusters in a semiconductor material after implantation, can also lead to strain fields in the implanted structure. Ion-channeling is a well-known technique to investigate tetragonal distortion in strained crystalline layers. In this thesis, the ion-channeling technique is used to investigate for the first time with success a number of nanostructured semiconductors produced by the methods mentioned above.

## Quantum dots

Most semiconductor devices consist of well-defined, atomically flat epitaxial layers that spatially limit charge carriers in one direction, like in a quantum well diode laser. The charge carriers can occupy a range of electronic states, and consequently, a range of possible transitions occurs, while only one is desired (see Fig. 1.1). Quantum dots (QDs) are semiconductor heterostructures, in which charge carriers are spatially confined in all three directions, and if the dimensions of the QDs are small enough, only particular electronic states can be occupied. The electronic spectrum of QDs prevents the deterioration of the device properties, which is induced by the high injection current and the smearing of charge carriers over an energy window of the order of  $k_B T$  due to the increase of the working temperature. Only particular electronic states that are separated by energies larger than  $k_B T$  can be occupied, and consequently, only one transition occurs (see Fig. 1.1). For a QD diode laser, the advantages are a narrower emission line width due to the discrete energy levels, a lower threshold current due to the absence of spatial separation of electrons and holes, and a higher temperature tolerance also due to the discrete energy

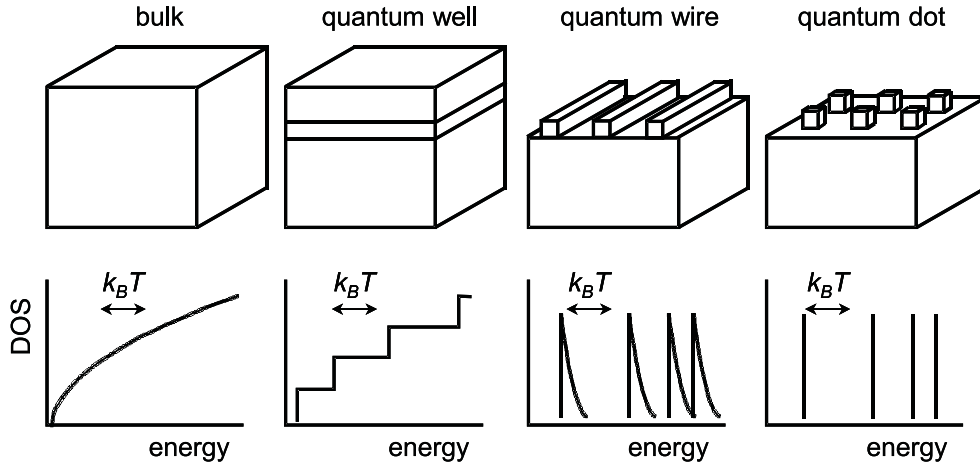


Figure 1.1: Density of states (DOS) of semiconductor structures in which the charge carriers are confined in zero (bulk), one (quantum well), two (quantum wire), and three dimensions (quantum dot). The arrow in the DOS graphs indicates the width of the energy window over which the charge carriers will be smeared out over the available states.

levels (no smearing) [14]. The most common way of fabricating QDs is with molecular beam epitaxy (MBE) via the so-called Stranski-Krastanov growth mode; due to the self-organizing effects of nanostructures in heteroepitaxial semiconductor systems, nanoscale islands are formed induced by lattice mismatch [15].

To calculate the electronic structure of QDs, mostly idealized physical shapes (usually pyramidal) are used, since good structural information is still lacking [16–19]. Most experiments and theoretical calculations on the morphology of QDs point to (truncated) pyramid-like shapes with a square base, although lens- and disk-shaped dots have also been identified [20, 21]. The large lattice mismatch, which is necessary for Stranski-Krastanov growth, will significantly change the band structure of the QDs, since the band structure is influenced by the internal strain distribution in the material.

Photoluminescence spectra point to (partially) strained QDs [22]. Strain analysis with MeV ion-channeling is usually restricted to the analysis of films with a thickness of at least 20 nm, while the typical height of QDs is only about 4 nm [23, 24]. Furthermore, typically about  $10^{10}$  QDs  $\text{cm}^{-2}$  are present, while in our set-up the cross-section of the ion beam on the sample is of the order of a few  $\text{mm}^2$ . This implies that the measured distortions are averaged over many QDs. Also, since the width of the QDs is typically about 12 nm, the surface coverage of the QDs is only about 1%. These factors highly complicate the investigation of strain in QDs with MeV ion-channeling, but in chapter 2 of this thesis experimental evidence is presented for the presence of strain fields, which extend from the InAs QDs into the surrounding GaAs matrix.

## Nano-films

Single-crystalline strained films are applied in group-IV devices like heterojunction bipolar transistors, and  $pn$  tunnel junctions [3, 4], and in III/V semiconductor devices like HEMTs [1]. Growth of high quality heterostructures with optimal structure parameters such as

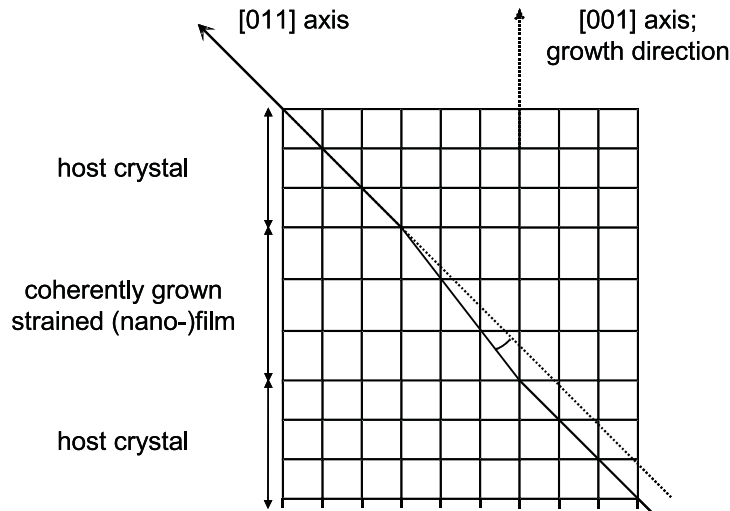


Figure 1.2: Schematic representation of a coherently grown, strained (nano-)film. For the sample shown, the cubic unit cells of the strained film are distorted due to compressive strain.

thickness and doping concentration of the layers has to be achieved, to obtain the desired device properties. The band gap and the band off-sets are very sensitive to both the doping concentration and the strain induced by the lattice mismatch in the heterostructure. Different growth techniques, like molecular beam epitaxy (MBE) [25] and chemical vapor deposition (CVD) [26] are able to produce epitaxial films with a thickness in the nanometer regime now, and characterization of these films is an interesting challenge for the ion-channeling technique. A schematic drawing of a coherent epitaxial buried (nano-)film is depicted in Fig. 1.2.

It was already mentioned that MeV ion-channeling is usually restricted to characterize films with a thickness of at least 20 nm. The nano-films which have been characterized in chapters 3-6 of this thesis have a thickness of only a few nanometers. For such thin films that are situated at the surface, the strain can still be measured by lowering the energy of the ion beam, which is proven with the medium energy ion scattering (MEIS) techniques [27, 28]. This method is however highly specialized and not applicable for the buried films which are commonly applied in devices. Therefore, in this thesis an innovative method is developed in order to characterize the tetragonal distortion in buried strained films with a thickness of only a few nanometer. This method introduces the MeV ion-channeling technique in the field of nano-films as a new technique for the characterization of lattice deformations.

## Ion implantation and clusters

In Si technology, implantation of dopants is the standard procedure for establishing dopant profiles, which determine the electrical characteristics of devices in integrated circuits. Since implantation of energetic ions into a crystalline semiconductor is accompanied by lattice damage and the implanted dopant is generally electrically inactive, rapid thermal annealing (RTA) is widely used to restore lattice order and achieve dopant activation

[7, 29].

In modern electronic devices boron (B) is the most widely used *p*-type dopant of Si, and as technology generations advance and devices become smaller, it is necessary to create sharp, ultra-shallow profiles with high concentrations of electrically active B. Achieving this by ion implantation however is not straightforward due to amongst others the formation of electrically inactive B clusters [8, 9]. Recently, it has been proposed that clustering is the result of the formation of a SiB<sub>4</sub> phase, using electron diffraction measurements upon a crystalline phase produced after very high dose ( $10^{17}$  ions/cm<sup>2</sup>) B<sup>+</sup> implantation and annealing [30]. These B clusters introduce strain in the implanted material, which leads to distortions of the crystal lattice in the form of strain fields around the clusters. Only very little data is available on the shape and dimensions of these lattice distortions, and in chapter 7 of this work MeV ion-channeling is used to investigate strain fields in B implanted Si. Similar to the case with quantum dots, the strain field can not be investigated around a single B cluster for this type of sample, since the cross-section size of the ion beam is many orders of magnitude larger than the size of a single B cluster. Therefore, the effects of the average distortions of the crystal lattice caused by many B clusters are observed simultaneously in the ion-channeling experiments presented in this thesis. A simple but effective model is introduced in Monte Carlo channeling calculations, which supplies a new method to estimate the dimensions of B clusters induced distortions in a Si crystal lattice with satisfactory accuracy from MeV ion-channeling experiments.

## Transmission channeling

Finally, a thin etched silicon wafer with a thickness of about 5.7  $\mu\text{m}$  was used in a feasibility study to investigate whether the methodology of transmission ion-channeling allows to detect the presence of dopant clusters after implantation. Since the range of MeV He<sup>+</sup> ions in silicon is about 10  $\mu\text{m}$  [31], a thin etched silicon wafer with a thickness of about 5.7  $\mu\text{m}$  can be used for transmission channeling experiments, in which case the ions pass through the sample and are detected on the other side. The energy loss of the transmitted ions yields information about the crystalline quality of the sample, since the energy loss for channeled ions is typically about 60% of the energy loss experienced by non-channeled particles [32, 33]. If for example, precipitates or clusters are present in the sample, they will induce lattice deformations, and consequently, part of the channeled fraction of the ion beam will dechannel, which leads to a higher average energy loss of the transmitted ions. This is especially interesting for samples with dopants which have a mass smaller than that of the host lattice. These light dopants are very hard to identify in a Rutherford backscattering spectrometry (RBS) spectrum, because their signal disappears in the statistical noise on the background signal of the matrix due to their low concentration [34]. If the effect of dopant clusters on the morphology of the host crystal is large enough to change the energy distribution of the transmitted ion beam, the critical implantation dose for clustering can be determined with the transmission channeling technique.

In order to obtain detailed information about the morphology of the sample from the transmitted energy distribution, Monte Carlo (MC) calculations are needed. It turns out that the energy distribution of the transmitted beam can only be reproduced with MC



channeling calculations, when the energy loss of ions through the material is handled appropriately. The by far most widely used Monte Carlo channeling simulation program FLUX [35] does not deal with energy dependence of the electronic stopping power, which for MeV ions is the largest contribution to the stopping power. Therefore, an energy dependent electronic stopping power model has been added to FLUX, which is shown in chapter 8 of this thesis. Such an improvement of the stopping power model is necessary to be able to adequately simulate the transmitted energy distribution for a 5.7  $\mu\text{m}$  thick Si wafer.

### III MeV ion-channeling as instrument for materials analysis

#### RBS ion-channeling

Rutherford backscattering spectrometry (RBS) is an ion beam analysis technique which operates in the MeV energy range. When a target is bombarded with MeV ions, binary elastic collisions occur between incoming ions and target nuclei. The energy transfer in the collisions is solely determined by the scattering angle and the mass ratio of the incoming ions and the target nuclei. By applying a mono-energetic ion beam from an accelerator and measuring the kinetic energy of backscattered ions at a well-defined angle, the target atoms can be identified (see Fig. 1.3). RBS is especially suitable for profiling heavy atoms in a light matrix [34]. When the incident ions are scattered at a certain depth beneath the surface, energy loss also occurs along the trajectory in the sample. The energy loss results from interaction with the target electrons (electronic energy loss) and nuclei (nuclear energy loss), and implies that RBS can be used for depth profiling in a depth region up to a few  $\mu\text{m}$ . Examples of a channeled and non-channeled RBS spectrum are shown in Fig. 1.3 for measurements with 4 MeV  $\text{He}^+$  ions on a sample consisting of a 743 nm thick  $\text{Si}_{0.8}\text{Ge}_{0.2}$  epi-layer on a Si substrate. The  $\text{He}^+$  ions scattered on Ge atoms are found at a higher energy in the spectrum than  $\text{He}^+$  ions scattered on Si atoms, due to the higher atomic mass of Ge atoms.  $\text{He}^+$  ions scattered beneath the surface did lose energy traversing the sample on the incoming and outgoing path, and therefore are found at a lower energy in the spectrum. The energy loss can be related to the depth where the  $\text{He}^+$  ions experienced a large angle scattering event, and the corresponding depth scale is indicated in Fig. 1.3. The scattering yield is proportional to the scattering cross-section governed by the Coulomb potential. In the near surface region of the non-channeled spectrum the observed Si yield varies (1.9-2.2 MeV). This is not due to a non-uniformity of composition in the top layer, but is due to a resonance in the  $^{28}\text{Si}(\alpha, \alpha)^{28}\text{Si}$  scattering cross-section which occurs near 3.9 MeV [36]. Furthermore, the scattering cross-section is proportional to the square of the atomic number, which explains why in Fig. 1.3 the yield of  $\text{He}^+$  ions scattered on Ge atoms is about equal to the yield of ions scattered on Si in spite of its lower concentration. The depth resolution achieved with RBS strongly depends on the scattering geometry, and can be as low as 1 nm, when a glancing exit angle geometry is used in the experiment [37].

Channeling is a process which occurs when an ion beam is directed along a major

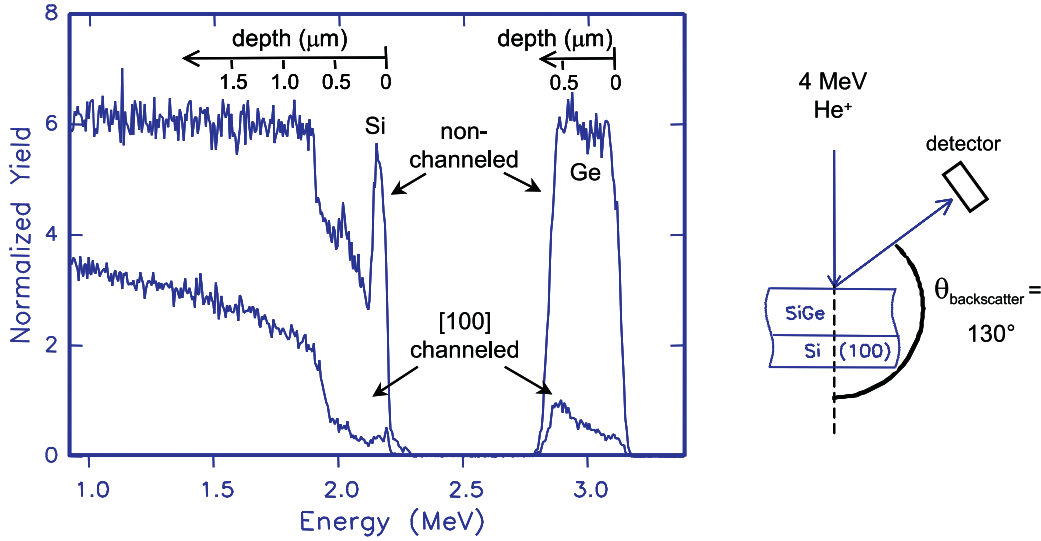


Figure 1.3: RBS spectra for the [001] axial channeling and a non-channeling direction in a sample consisting of a 743 nm thick  $\text{Si}_{0.8}\text{Ge}_{0.2}$  epi-layer on a Si substrate. The scattering geometry is indicated on the right.

crystalline direction of a single crystal. For axial and planar directions, the crystal consists of large open spaces confined by atomic strings and planes, respectively. By a series of small angle collisions the ions are gently steered away from the strings or planes towards the centre of the so-called channel or between the planes. This is indicated in Fig. 1.4 (a). Due to the formation of shadow cones along the strings or planes, the probability of a large angle deflection decreases by almost two orders of magnitude in an ideal case, which is observed as a decrease in the scattering yield in a RBS energy spectrum. This effect is observed in the [100] channelled spectrum of Fig. 1.3. Furthermore, the range of the ions into the target sample is strongly increased. Note, that in Fig. 1.3 the channelled yield increases at the interface of the  $\text{Si}_{0.8}\text{Ge}_{0.2}$  epi-layer and the Si substrate due to the presence of interfacial defects.

A so-called angular scan is obtained by measuring the scattering yield in a certain energy window or depth interval as a function of the angle between the ion beam and the crystal direction. The width of the angular scan is characterized by the half angle  $\psi_{1/2}$  for an ion to become channelled in a major axial or planar direction. Angular scans for Ge in the epi-layer and Si in the substrate are shown in Fig. 1.4 (b), together with the half angle  $\psi_{1/2}$  for the Si angular scan. The angle of incidence for which a minimum occurs in an angular scan, corresponds to the direction of the crystal axis or plane. The shift of the Ge angular scan relative to the Si angular scan is a measure for the tetragonal distortion in the  $\text{Si}_{0.8}\text{Ge}_{0.2}$  epi-layer, which according to elasticity theory can be related to the strain in the epi-layer [38]. This makes ion-channeling in combination with RBS an excellent tool for analyzing lattice deformations in crystalline semiconductor structures.

Interpretation of the characteristic features of channeling experiments, like  $\psi_{1/2}$ , is usually conducted using the model presented in 1965 by Lindhard, in which the deflection of an ion by an atomic string or plane [see Fig. 1.4 (a)] is described with an average of the potentials of the individual atoms [39]. On the basis of this so-called continuum

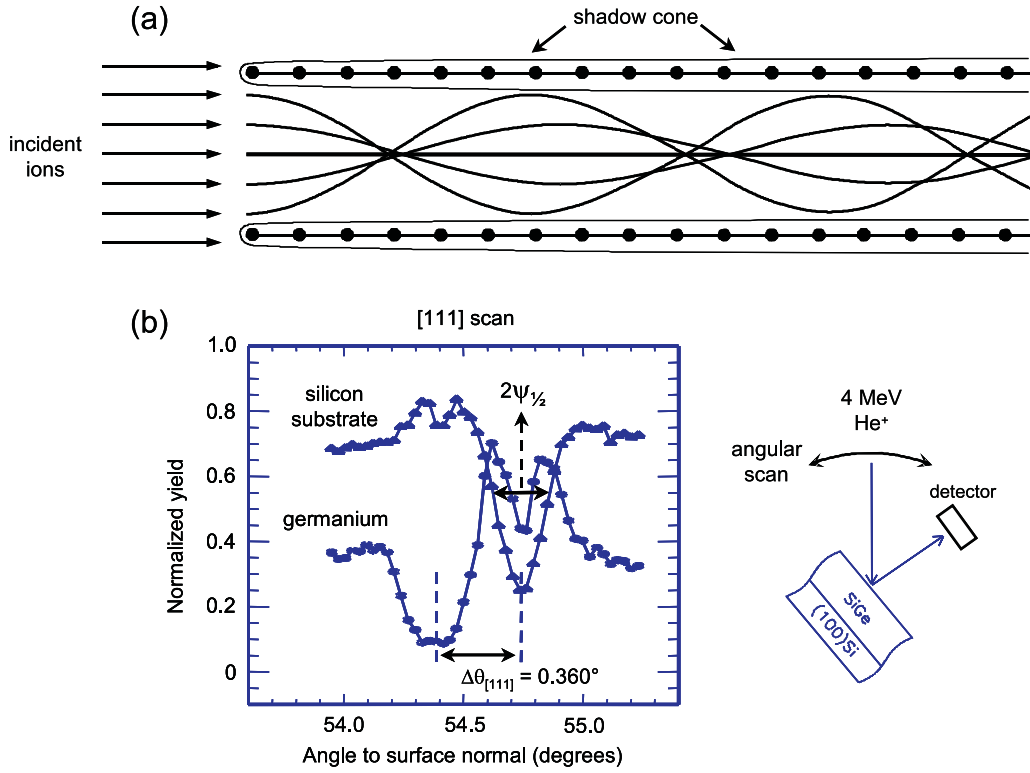


Figure 1.4: Schematic drawing of the channeling effect (a), and the measured Si (substrate) and Ge (epi-layer) angular scans of the [111] axis for the same sample as in Fig. 1.3 (b). The half angle  $\psi_{1/2}$  is indicated for the Si angular scan. Furthermore, the scattering geometry is indicated.

potential, a characteristic angle  $\psi_1$  can be derived, which is closely correlated to the empirical half angle  $\psi_{1/2}$  and correctly predicts the dependence of  $\psi_{1/2}$  on the incoming energy, the nuclear charge of the atoms in the target crystal, and the crystal direction. The characteristic angle is given by:

$$\psi_1 = \left( \frac{2Z_1 Z_2 e^2}{4\pi\epsilon_0 E d} \right)^{1/2}, \quad (1.1)$$

where the atomic number of the incoming particle and the target atom are represented by  $Z_1$  and  $Z_2$  respectively,  $E$  is the energy of the incoming particle and  $d$  is the lattice spacing along the channeling direction. This equation explains for example why the width of the Ge angular scan is larger than that of Si in Fig. 1.4 (b).

As channeled ions penetrate into a perfect crystal, an increasing number of them becomes dechanneled due to a combination of multiple scattering by electrons and scattering by thermally displaced atoms at the channel walls or planes. Furthermore, although the probability of a large angle deflection decreases for target atoms beneath the surface, the target atoms near the surface still have a considerable contribution to the scattering yield, which gives rise to a so-called surface peak. Both these contributions to the scattering yield are indicated in the channeled spectrum of Fig. 1.5 (a), which shows a measurement

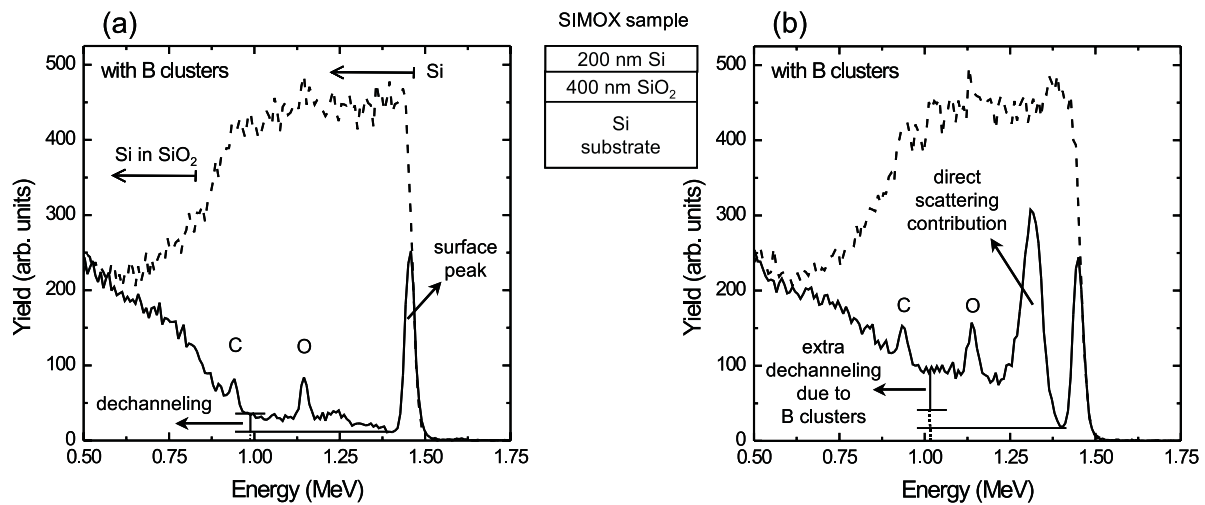


Figure 1.5: RBS spectra for the [001] axial channeling (solid line) and a non-channeling direction (dashed line) in SIMOX samples without (a) and with B clusters present (b). All contributions to the scattering yield are explained in the text.

on a sample consisting of a Si wafer with a 400 nm insulating SiO<sub>2</sub> film, and a 200 nm Si film on top (SIMOX sample). An imperfect crystal contains defects, which introduce distortions in the lattice structure, which in turn lead to a direct scattering contribution and an increase of the dechanneling yield above that for a perfect crystal. Both these effects are visible in the measured spectra of Fig. 1.5 (b), which shows measurements of the same SIMOX sample as in Fig. 1.5 (a) after implantation with B above the solid solubility. This resulted in the formation of B clusters, which in turn lead to lattice distortions. Each type of defect has a particular influence on the trajectory of a passing ion and can be associated with a corresponding dechanneling factor. The partition of the ion trajectories into channeled and dechanneled components by means of a dechanneling factor can be used to determine the number of defects and their depth distribution in the crystal [40].

## Equilibrium flux distribution

A detailed interpretation of the interaction of channeled ion beams with lattice deformations or defects requires knowledge of the channeled ion flux distribution. When ions become channeled, they will start following oscillating trajectories in the channels or between the planes, which results in a depth dependent flux distribution [see Fig. 1.4 (a)]. Since the ion-atom potential is not exactly harmonic, the transverse energy of the ions determines the amplitude and wavelength of the oscillation. Therefore, and due to interaction with the target electrons, the coherency between the oscillating trajectories of the channeled ions will disappear, and at a certain depth the flux distribution of channeled ions will become depth independent (see Fig 1.7). This is called the steady state flux distribution, and it is achieved after typically 100-200 nm for axially channeled MeV He<sup>+</sup> ions, while for planar channeling the steady state flux is reached at greater depth [40].

Feldman *et al.* derived an analytical model to describe the steady state flux distribu-

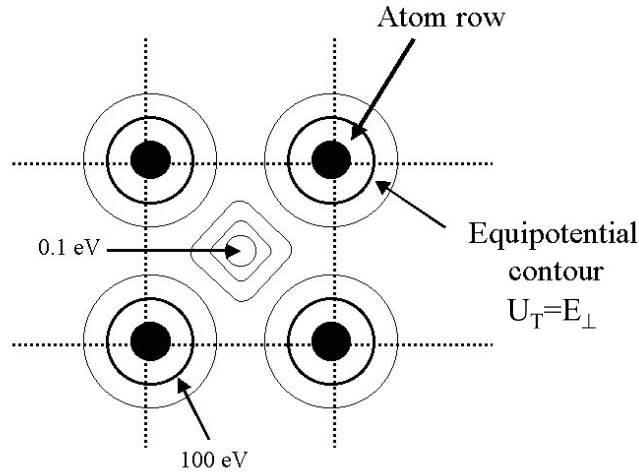


Figure 1.6: Equipotential contours for the axial continuum potential for the case of  $\text{He}^+$  ions in the  $[001]$  direction of tungsten (from Feldman *et al.* [40]).

tion of channeled ions, based on the continuum model of Lindhard [40]. The motion of an ion with a transverse energy  $E_{\perp}$  is confined within the equipotential contour in the channel given by  $U_T = E_{\perp}$  (see Fig. 1.6). The Feldman model assumes that the probability to find the ion within the equipotential contour  $U_T$  is uniform. The flux distribution can then be calculated from integration of contributions from all ions. Assuming that the incoming particles are distributed homogeneously over the channel area, the result is a steady state flux distribution which is peaked in the centre of the channel [see Fig. 1.7 (a)].

Feldman and co-workers also showed that this steady state flux distribution depends on the angle  $\psi$  between the incoming beam and the crystal axis along which channeling takes place. When  $\psi$  is increased, the average transverse energy of the channeled ions will also increase, and the flux density is no longer peaked in the centre of the channel but distributed over a larger area in the channel, since more ions will be able to occupy higher energy potential contours in the channel [see Fig. 1.7 (b)]. The same is applicable to planar channeling. In chapters 3-6 it is demonstrated that the angular dependency of the channeled flux distribution can be used to probe across the crystal channels or planes.

## Monte Carlo simulations

The continuum model from Lindhard has proven to be successful to gain qualitative insight into ion-channeling experiments. In order to introduce more detailed physical models and statistical processes, channeling simulation codes are needed, and those based on Monte Carlo (MC) methods are the most popular. They are particularly useful to obtain insight in channeling phenomena governed by a depth dependent flux distribution.

The most sophisticated and by far most widely used MC channeling simulation code is FLUX [35], which is used for the calculations presented in this thesis. The calculations are based on binary collisions of the incoming particle and the target atoms, described by a screened ion-atom potential. This means that no channeling effects are assumed

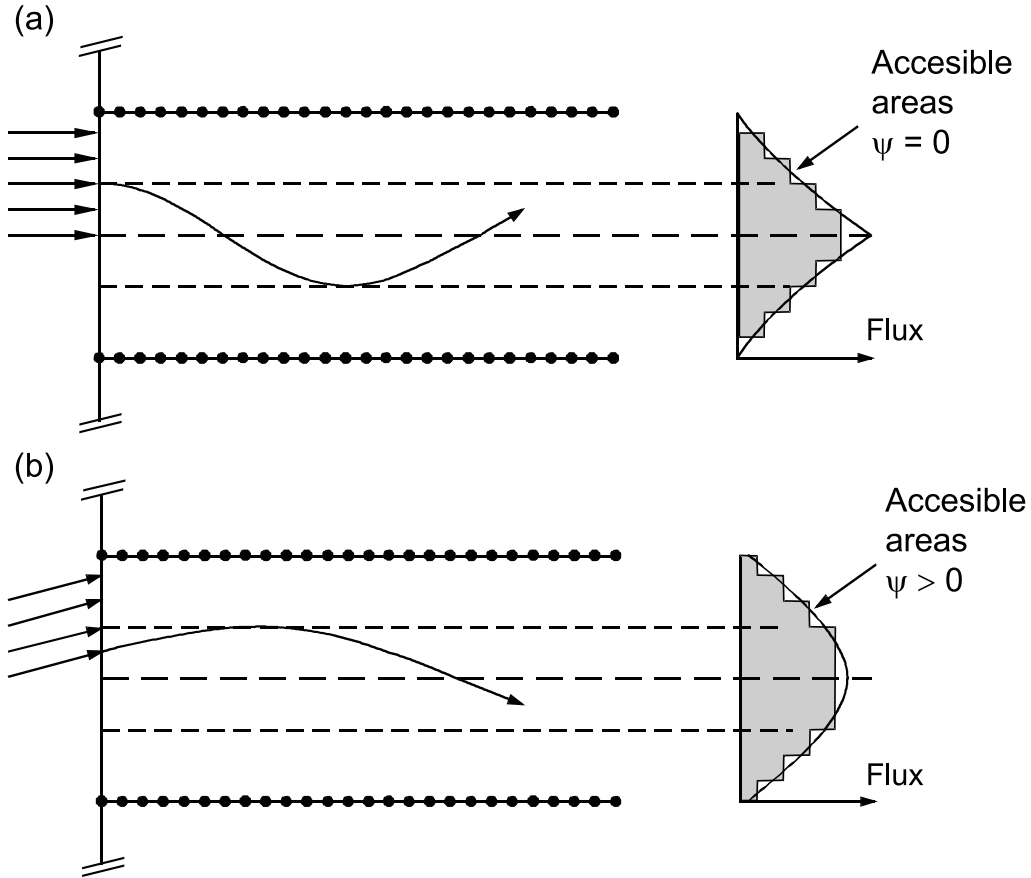


Figure 1.7: Schematic illustration of the origin of the central peaking in the channeled ion flux distribution for ions uniformly incident on an axial channel with  $\psi = 0$  (parallel incidence) (a), and the origin of the flux distribution for the case  $\psi \neq 0$  (b) (from Feldman *et al.* [40]).

*a priori*. Furthermore, the effect of the surrounding strings (see Fig. 1.8) is treated in the continuum model, and thermal vibrations of the target atoms and the stopping of the projectiles by electrons in the solid are incorporated. The thermal vibrations are accounted for by assuming that the target atoms have a Gaussian distribution of positions around their equilibrium position, with  $\langle x^2 \rangle = \langle y^2 \rangle = u_1^2$  obtained from the Debye model [see Fig. 1.8 (b)]. The stopping of MeV ions in the target originates almost entirely from inelastic collisions with target electrons. In FLUX, the ion-electron interaction is split into contributions of the strongly bound inner shell electrons (core electrons) and the loosely bound outer shell electrons (valence electrons). The contribution from the core electrons is a function of the impact parameter. The energy loss due to the valence electrons can be split again into collisions with small impact parameters (the local valence contribution), and interactions with distant electrons in the form of excitation of plasma oscillations. In FLUX, both terms are described assuming a uniform valence electron distribution throughout the target sample.

FLUX confines the calculations to a rectangular unit cell with one atom. This cell is chosen such that the whole  $xy$ -plane, which is the plane perpendicular to the atomic strings along the channeling direction, can be composed of translated and/or rotated

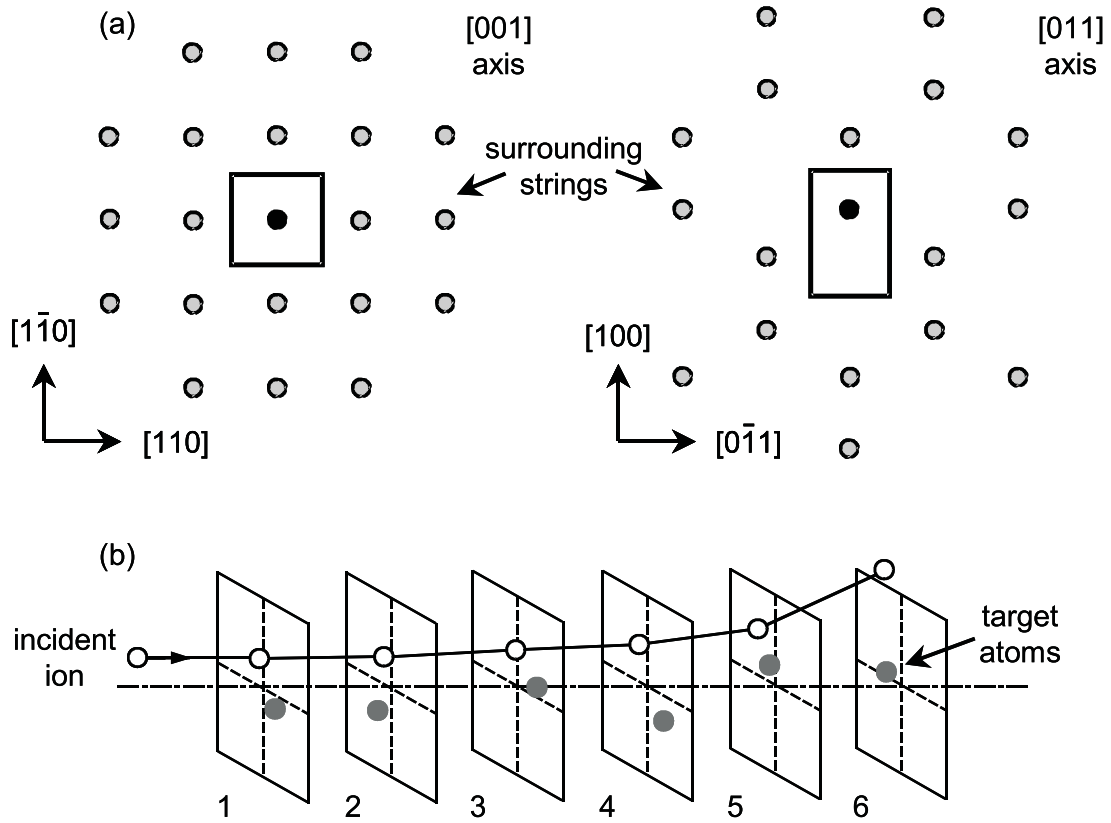


Figure 1.8: Positions of the atoms in the  $xy$ -plane for two main directions of the Zinc-Blende structure. The rectangular cell in which the incoming ions are distributed randomly is indicated. The central atom, indicated by the black dot, undergoes the first binary collision with the incoming ion. The surrounding atom strings are indicated by gray dots (a). The incident ion experiences a sequence of scattering events from target atoms whose equilibrium positions are indicated by the intersection of the dashed lines (b).

cells. This is shown in Fig. 1.8 for two main directions of a zinc-blende structure, which is the crystal structure of  $\text{Si}_{1-x}\text{Ge}_x$  and GaAs. The initial positions of the incoming ions are distributed randomly over the cell, and the first binary collision occurs with the atom in this cell. For every atom in the central string, the ion's angular deflection and energy loss are calculated from contributions of the collision with the target atom, and interaction with the target electrons and the continuum potentials of the surrounding strings. In the distant strings, the continuum potentials describe the Coulomb field of the nuclei screened by electrons. The position of the ion in the  $xy$ -plane for each consecutive binary collision is calculated by considering the trajectory between two collisions as a straight line, as indicated in Fig. 1.8 (b). If during its trajectory the ion leaves the main cell, it is translated back into the main cell at an equivalent position.

For simulations on a wide range of crystalline samples, different types of crystal lattices with different layers containing one or two types of atoms can be given as input. Furthermore, the code is able to introduce strain (rotation of the crystal lattice), stacking faults (shift of the crystal lattice), or curvature (bending of the crystal lattice) in the simulated

sample. The strain in a buried  $\text{Si}_{1-x}\text{Ge}_x$  film grown in between Si layers leads to a kink in the off-normal [011] channel, which can be simulated by rotating the velocity vector of the ions at the beginning and end of the  $\text{Si}_{1-x}\text{Ge}_x$  film. The larger lattice constant in the  $\text{Si}_{1-x}\text{Ge}_x$  film is accounted for by a separate lattice constant in the input file. In the same way, a shift of the crystal lattice induced by a stacking fault can be simulated by adding a component to the  $x$ - and  $y$ -values of the ions at the depth of the stacking fault. Finally, a bent crystal can be simulated by the option 'curvature', which specifies a radius of the curvature and a plane perpendicular to the crystal axis by giving an angle  $\phi$  of the intersection with the  $xy$ -plane.

FLUX is used to calculate amongst others the energy loss and the nuclear encounter probability (NEP) with a target atom to cause an event like large angle scattering (in a simulation of a RBS experiment), which is normalized by the probability for a random medium with the same density of atoms. These are output as a function of depth and can be used to generate RBS yield-energy-spectra. Other output can consist of the exit coordinates and velocity vectors of the ions at the end of a trajectory, the flux distribution, the final velocity and energy distribution, or the  $xy$ -coordinates for the ions throughout the whole trajectory for ion trajectory calculations. Depending on the information needed for a certain experiment, a choice of these parameters can be made to obtain insight in the channeling process.

FLUX is internationally recognized as the leading program to perform Monte Carlo channeling simulations [41–45]. The program is originally written to operate in a UNIX environment, but implementation of the program on a OpenVMS operating system in Eindhoven was achieved to perform all calculations under own administration in order to obtain immediate feedback with the experiments.

For some of the applications treated in this thesis, the program FLUX had to be extended. In chapter 7, B clusters are investigated, which induce strain fields with a 3-dimensional character. In order to simulate the lattice distortions around a B cluster, the option 'curvature' was used. The direction of the curvature is defined by a plane perpendicular to the crystal axis by giving an angle  $\phi$  of the intersection with the  $xy$ -plane. The 3-dimensionality of the lattice distortions is accounted for by choosing a random direction of the curvature. The random direction of the curvature is an extra asset of FLUX programmed in Eindhoven.

Furthermore, in chapter 8 the physical model in FLUX which describes the electronic stopping power had to be improved in order to obtain a satisfactory resemblance of the calculated transmitted energy distributions with the measured transmitted energy distributions obtained from transmission channeling experiments on a  $5.7 \mu\text{m}$  thick Si wafer. This has been obtained by implementation of energy dependence of the stopping power in FLUX. This is an extended feature, which has also been programmed in Eindhoven.

## Comparison with other techniques

X-ray diffraction (XRD) is probably the most common technique for the characterization of lattice deformations [46, 47]. The main advantage of XRD over ion-channeling is a (relatively) cheap set-up, since no accelerator and vacuum system are needed. This also dramatically reduces the size of the set-up. RBS ion-channeling on the other hand, in-



corporates simultaneous elemental analysis. In chapter 3 of this thesis, both techniques are compared to determine the tetragonal distortion in a 2.2 nm thick strained  $\text{Si}_{1-x}\text{Ge}_x$  nano-film, and ion-channeling will appear to be competitive with high resolution XRD.

Another technique which is often used for the characterization of lattice deformations is transmission electron microscopy (TEM). TEM has the advantage of rendering microscopic information [48, 49], which is not available in techniques like XRD [50], or wafer bending [51]. *Transmission* ion-channeling can be combined with a nuclear microprobe, which brings imaging of stacking faults or interface dislocations within reach, as is demonstrated in the channeling scanning transmission ion microscopy (CSTIM) technique [52, 53]. With cross-sectional TEM, the positions of atoms in a lattice can be determined from the electron diffraction pattern. One of the main disadvantages of TEM is the laborious sample preparation, which can take up to days. Furthermore, it has been shown that the thinning geometry (cross-sectional or in plane view) can influence the structure of the layers in the sample [54]. Another disadvantage comes forward when small clusters in a matrix have to be investigated, since the minimum cluster size that can be determined with TEM is 5 nm [46]. The B clusters in Si, which are investigated in chapters 7 and 8 of this thesis, are predicted from molecular dynamics calculations to be much smaller (only 4-5 atoms per cluster) [55].

## Experimental set-up

To perform RBS channeling experiments, basically a particle accelerator, vacuum chamber, goniometer, and energy detector are needed. The particle accelerator in our set-up is the AVF (azimuthally varying field) Cyclotron at the Eindhoven University of Technology, from which  $\text{He}^+$  ion beams were extracted in the energy range of 2-6 MeV. The ions are transported to the scattering chamber through a beam line. In order to preserve a low angular spread in the ion beam, the pressure in the scattering chamber and the beam line is below  $3 \times 10^{-8}$  and  $3 \times 10^{-5}$  mbar, respectively.

Since the half angle for channeling  $\psi_{1/2}$  with MeV  $\text{He}^+$  ions is typically  $0.5\text{-}1^\circ$  [40], a high precision goniometer is needed to obtain proper alignment of the target crystal axes or planes with the ion beam. Such a goniometer was designed and constructed at the Eindhoven University of Technology, with three axes of rotation and three directions of translation. The angular resolution of the goniometer is better than  $0.005^\circ$  [33]. Furthermore, the angular spread of the ion beam has to be smaller than typically 0.3 times the half angle for channeling  $\psi_{1/2}$  to avoid that the measured channeling characteristics are influenced by the beam divergence [33]. This is achieved by two pairs of horizontal and vertical collimator slits in the beam line, 7.68 m apart. No focusing or bending magnets are placed in between the two sets of slits, or in between the goniometer and the slits, which results in a well defined parallel ion beam suitable for ion-channeling experiments. Finally, the detector is mounted on a stepper-motor controlled detector disk to obtain a high flexibility in the detector position and angle, for RBS and transmission channeling experiments. A schematic drawing of the set-up is shown in Fig. 1.9.

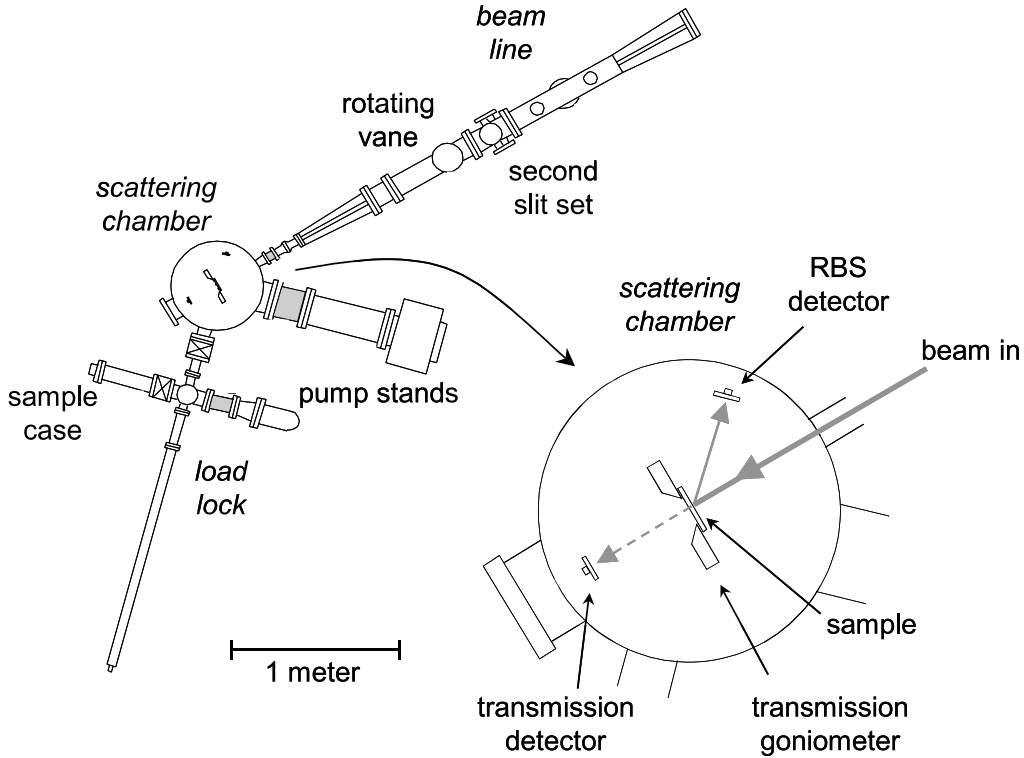


Figure 1.9: Schematic showing the top view of the scattering chamber, beam line, and load lock. The scattering chamber is magnified in the lower right side. In order to compare the experiments quantitatively, a rotating vane with a 88 nm thick gold film is placed in the ion beam to measure the ion dose. The load lock is used for sample transfer without the need of venting the scattering chamber. A sample case is attached to the load lock for measurements on up to 5 samples without the need of venting the load lock.

## IV Outline of this thesis

Chapter 2 deals with strain measurements on InAs/GaAs quantum dots. The distribution of the strain in and around the QDs is rather complex, and the MC calculation program FLUX is not able to incorporate these 3-dimensional strain fields in the simulations. Calculations with FLUX are therefore only used to confirm a few basic assumptions, while determination of the strain is mainly based upon the interpretation of the outcome of the channeling measurements.

In chapter 3, strain measurements on 2.2 nm thick buried  $\text{Si}_{1-x}\text{Ge}_x$  nano-films are presented. Usually, the direction of a main crystal axis is determined by measuring the backscatter yield as a function of the angle between the sample normal and the ion beam. The strain can then be calculated from the shift of such an angular scan of the strained layer relative to that of the capping layer. However, the thickness of the  $\text{Si}_{1-x}\text{Ge}_x$  nano-films is only a few nanometer, which is outside the range of this method. An innovative method is presented which proves to be able to determine the tetragonal distortion in the  $\text{Si}_{1-x}\text{Ge}_x$  nano-films from axial ion-channeling measurements in combination with MC calculations. At the end of chapter 3 this method is compared to the X-ray diffraction

technique (XRD).

Also planar channeling measurements are performed on the buried  $\text{Si}_{1-x}\text{Ge}_x$  nano-films, and the flux distribution turns out to be still oscillating at the depth of the nano-film. MC calculations of these measurements appear to be very sensitive to the choice of ion-atom potential, which determines the wave-length of the oscillating trajectories of the channeled ions. Therefore, in chapter 4, a comparison is made between three well-known ion-atom potentials.

Only one of the ion-atom potentials used in chapter 4 provides satisfactory results. With this potential incorporated in FLUX, the method to determine the tetragonal distortion in the  $\text{Si}_{1-x}\text{Ge}_x$  nano-films is extended to planar channeling in chapter 5. The accuracy of the planar channeling results is compared to that of the axial channeling results from chapter 3.

In chapter 6, the new tetragonal distortion measurement method for nano-films is unleashed at a complex sample with an InAs/GaAs superlattice, of which the tetragonal distortion in the 1.1 monolayer thick InAs films in the superlattice is determined.

Axial channeling measurements and simulations on B implanted Si wafers are discussed in chapter 7. For one of the samples the implantation dose was high enough to create B clusters. The crystal lattice of the implanted region is distorted by those clusters, which can be clearly seen in a channeled RBS spectrum as a direct scattering peak and an increase in the yield due to enhanced dechanneling. The dimensions of the distortions are estimated by comparing the contents of the direct scattering peak and the increase in the scattering yield due to enhanced dechanneling between measurements and MC simulations on a curved crystal lattice.

Finally, in chapter 8 transmission channeling experiments on a thin etched Si wafer are presented. The measurements are performed on a  $5.7 \mu\text{m}$  thick Si sample, which implies that the energy loss of the ions during the transmission can no longer be treated as energy independent. Furthermore, a feasibility study is performed of the possibility to detect lattice distortions induced by clusters, in transmission channeling experiments.

## References

- [1] T. S. Moss, *Handbook on Semiconductors* (North Holland, Amsterdam, 1993).
- [2] L. Wu, S. J. Koester, W. W. Xie, J. O. Chu, P. M. Tso, and I. Adesida, *J. Vac. Sci. & Techn. B* **18**, 3488 (2000).
- [3] P. Mushini and K. P. Roenker, *Sol. State Electr.* **44**, 2239 (2000).
- [4] J. Yang, A. Banerjee, and S. Guha, *Appl. Phys. Lett.* **70**, 2975 (1997).
- [5] E. Rimini, *Ion Implantation: Basics to Device Fabrication* (Kluwer Academic Publishers, Boston, 1995).
- [6] I. Yamada, W. L. Brown, J. A. Norhby, and M. Sosnowski, *Nucl. Instrum. and Meth. B* **79**, 223 (1993).

- 
- [7] A. G. Dirks, P. H. L. Bancken, J. Politiek, N. E. B. Cowern, J. H. M. Snijders, J. G. M. van Berkum, and M. A. Verheijen, in *Proceedings of the International Conference on Ion Implantation Technology, Kyoto, Japan, June 1998*, **Vol. 2**, 1167.
- [8] T. J. Lenosky, B. Sadigh, S. K. Theiss, M. Caturla, and T. D. de la Rubia, *Appl. Phys. Lett.* **77**, 1834 (2000).
- [9] T. Wang, A. G. Cullis, E. J. H. Collart, A. J. Murrell, and M. A. Foad, *Appl. Phys. Lett.* **77**, 3586 (2000).
- [10] L. Fedina, O. I. Lebedev, G. van Tendeloo, J. van Landuyt, O. A. Mironov, and E. H. C. Parker, *Phys. Rev. B* **61**, 10.336 (2000).
- [11] R. D. Twesten, D. M. Folstaedt, S. R. Lee, E. D. Jones, J. L. Reno, J. M. Millunchick, A. G. Norman, S. P. Ahrenkiel, and A. Mascarenhas, *Phys. Rev. B* **60**, 13.619 (1999).
- [12] T. Kamiya, K. Nakahata, K. Ro, C. M. Fortmann, and I. Shimizu, *Jap. J. Appl. Phys. part I* **38**, 5750 (1999).
- [13] K. Shum, P. M. Mooney, L. P. Tilly, and J. O. Chu, *Phys. Rev. B* **55**, 13.058 (1997).
- [14] N. N. Ledentsov, V. M. Ustinov, V. A. Shchukin., P. S. Kop'ev, Zh. I. Alferov, and D. Bimberg, *Semiconductors* **32**, 343 (1998).
- [15] D. Leonard, M. Krishnamurthy, C. M. Reaves, S. P. Denbaars, and P. M. Petroff, *Appl. Phys. Lett.* **63**, 3203 (1993).
- [16] M. Grundmann, O. Stier, and D. Bimberg, *Phys. Rev. B* **52**, 11.969 (1995).
- [17] M. Cusack, P. R. Briddon, and M. Jaros, *Phys. Rev. B* **54**, R2300 (1996).
- [18] C. Pryor, *Phys. Rev. B* **57**, 7190 (1998).
- [19] J. Kim, L. Wang, and A. Zunger, *Phys. Rev. B* **57**, R9408 (1998).
- [20] W. Wu, J. R. Tucker, G. S. Solomon, and J. S. Harris, Jr., *Appl. Phys. Lett.* **71**, 1083 (1997).
- [21] O. Flebbe, H. Eisele, T. Kalka, F. Heingrichsdorff, A. Krost, D. Bimberg, and M. Dähne-Prietsch, *J. Vac. Sci. Technol. B* **17**, 1639 (1999).
- [22] T. Y. Wang, and G. B. Stringfellow, *J. Appl. Phys.* **67**, 344 (1990).
- [23] S. Guha, A. Madhukar, and K. C. Rajkumar, *Appl. Phys. Lett.* **57**, 2110 (1990).
- [24] L. Goldstein, F. Glas, J. Y. Marzin, M. N. Charasse, and G. L. Roux, *Appl. Phys. Lett.* **47**, 1099 (1985).
- [25] J. Brübach, A. Y. Silov, J. E. M. Haverkort, W. v. d. Vleuten, and J. H. Wolter, *Phys. Rev. B* **59**, 10 315 (1999).
- [26] S. Bozzo, J. Lazzari, C. Coudreau, A. Ronda, F. Arnaud d'Avitaya, J. Derrien, S. Mesters, D. Holländer, P. Pergaud, and O. Thomas, *J. Cryst. Growth* **216**, 171 (2000).

- [27] J. F. van der Veen, Surf. Sci. Rep. **5**, 199 (1985).
- [28] T. C. Q. Noakes, P. Bailey, P. K. Hucknall, K. K. Donovan, and M. A. Howson, Phys. Rev. B **58**, 4934 (1998).
- [29] L. Pelaz, V. C. Venezia, H. Gossmann, G. H. Gilmer, A. T. Fiory, C. S. Rafferty, M. Jaraiz, and J. Barbolla, Appl. Phys. Lett. **75**, 662 (1999).
- [30] A. Agarwal, H. Gossmann, D. J. Eaglesham, D. C. Jacobson, T. E. Haynes, J. Jackson, Yu. E. Erokhin, and J. M. Poate, *4th International Workshop on Measurement, Characterization and Modeling of Ultra-Shallow Doping Profiles*, 1997, pp. 39.139.9.
- [31] J. F. Ziegler, J. P. Biersack, and U. Littmark, in *The Stopping and Range of Ions in Solids* (Pergamon Press, New York, 1985).
- [32] F. H. Eisen, G. J. Clark, J. Bottiger, and J. M. Poate, Radiat. Eff. **13**, 93 (1972).
- [33] P. W. L. Van Dijk, Ph.D. thesis, Eindhoven University of Technology, 1997.
- [34] W. K. Chu, J. W. Mayer, and M. A. Nicolet, *Backscattering Spectrometry* (Academic Press, London, 1978).
- [35] P. J. M. Smulders, and D. O. Boerma, Nucl. Instrum. and Meth. B **29**, 471 (1987).
- [36] J. F. Ziegler and J. E. E. Baglin, J. Appl. Phys. **42**, 2031 (1971).
- [37] Y. Tamminga, M. F. C. Willemsen, F. H. P. M. Habraken, and A. E. T. Kuiper, Nucl. Instrum. and Meth. Phys. Rev. **200**, 499 (1982).
- [38] J. Y. Tsao, *Materials Fundamentals of Molecular Beam Epitaxy* (Academic Press, San Diego, 1992).
- [39] J. Lindhard, K. Dan. Vidensk. Selsk. Mat. Fys. Medd. **34** (1965).
- [40] L. C. Feldman, J. W. Mayer, and S. T. Picraux, *Materials Analysis by Ion Channeling* (Academic Press, New York, 1982).
- [41] M. B. H. Breese, D. G. de Kerckhove, P. J. M. Smulders, W. M. Arnold-Bik, and D. O. Boerma, Nucl. Instrum. and Meth. B **171**, 387 (2000).
- [42] K. Lorenz, R. Vianden, R. Birkhahn, A. J. Steckl, M. F. da Silva, J. C. Soares, and E. Alves, Nucl. Instrum. and Meth. B **161-163**, 946 (2000).
- [43] R. Moons, S. Blsler, J. Dekoster, A. Vantomme, J. De Wachter, and G. Langouche, Thin Solid Films **324**, 129 (1998).
- [44] M. B. H. Breese and P. J. M. Smulders, Phys. Rev. Lett. **81**, 5157 (1998).
- [45] A. Vantomme, U. Wahl, M. F. Wu, S. Hogg, H. Pattyn, G. Langouche, and H. Bender, Nucl. Instrum. and Meth. B **136-138**, 471 (1998).
- [46] G. Glass, H. Kim, P. Desjardins, N. Taylor, T. Spila, Q. Lu, and J. E. Greene, Phys. Rev. B **61**, 7628 (2000).

- 
- [47] E. Zolotoyabko, A. Goldner, and Y. Komem, Phys. Rev. B **60**, 11.014 (1999).
- [48] C. Liu, J. M. Gibson, D. G. Cahill, T. I. Kamins, D. P. Basile, and R. S. Williams, Phys. Rev. Lett. **84**, 1958 (2000).
- [49] N. Iizuka, and N. Suzuki, Jap. J. Appl. Phys. **39**, 2376 (2000).
- [50] A. J. Steinfert, P. M. L. O. Scholte, A. Ettema, F. Tuinstra, M. Nielsen, E. Landemark, D. M. Smilgies, R. Feidenhans'l, G. Falkenberg, L. Seehofer, and R. L. Johnson, Phys. Rev. Lett. **77**, 2009 (1996).
- [51] J. A. Floro, E. Chason, L. B. Freund, R. D. Twisten, R. Q. Hwang, G. A. Lucadamo, Phys. Rev. B **59**, 1990 (1999).
- [52] M. B. H. Breese, P. J. C. King, J. Whitehurst, G. R. Booker, G. W. Grime, F. Watt, L. T. Romano, and E. H. C. Parker, J. Appl. Phys. **73**, 2640 (1993).
- [53] P. J. C. King, M. B. H. Breese, P. R. Wilshaw, and G. W. Grime, Phys. Rev. B **51**, 2732 (1995).
- [54] J. Bonevich, and D. Josell, Phys. Rev. Lett. **82**, 2002 (1999).
- [55] U. Beck, T. H. Metzger, J. Peisl, and J. R. Patel, Appl. Phys. Lett. **76**, 2698 (2000).



# 2. Evidence for strain in and around InAs quantum dots in GaAs from ion-channeling experiments

L. J. M. Selen, L. J. van IJzendoorn [\*], and M. J. A. de Voigt  
*Research School CPS, Cyclotron Laboratory, Department of Applied Physics, Eindhoven University of Technology, P.O. Box 513, 5600 MB Eindhoven, The Netherlands*

P. M. Koenraad  
*Research School COBRA, Department of Applied Physics, Eindhoven University of Technology, P.O. Box 513, 5600 MB Eindhoven, The Netherlands*

Strain in and around pyramidal InAs/GaAs quantum dots (QDs) fabricated by molecular beam epitaxy influences the density of states of the confined charge carriers. The presence of strain in QDs is required to explain their optical properties. In this paper MeV ion-channeling experiments are presented which provide evidence for the presence of strain in and around InAs QDs in GaAs. The small dimensions of the QDs (typical height 4 nm) and the presence of a wetting layer complicate the interpretation of channeling measurements, but our experiments show that extended strain fields around the QDs induce ion steering which accounts for the observed channeling behaviour.

## I Introduction

One of the hot topics in semiconductor physics is the production and study of low-dimensional structures, i.e. structures in which the charge carriers are confined to less than 3 dimensions. This confinement of the charge carriers changes the Density Of States (DOS), which leads to sharper optical transitions. The threshold current density and its temperature dependence are reduced and furthermore, the energy of the transition can be controlled by the well thickness. These effects are more pronounced for higher levels of confinement and can be achieved in either quantum wire lasers - charge carriers are free to move in only 1 direction - or quantum box or Quantum Dot (QD) lasers - total confinement with no direction of freedom.

It is very interesting that QDs can be grown without using lithography via so-called self-assembly. Such QDs are manufactured by the deposition of about two MonoLayers (ML) of InAs on GaAs, which results in the formation of InAs islands during growth.



Since the critical layer thickness for the growth of a single coherent strained InAs film on GaAs is only 1.4 ML, island formation becomes favorable as a mechanism to relieve strain. Photoluminescence spectra however point to (partially) strained QDs [1].

MeV ion-channeling is a well-known technique to investigate strain of thin films. Usually it is restricted to the analysis of films with a thickness larger than approximately 20 nanometers. The typical height of QDs, which is only 4 nm, and the low areal density of In in the investigated QD-samples ( $10^{10}$  QDs  $\text{cm}^{-2}$ ,  $11 \times 10^{14}$  In atoms  $\text{cm}^{-2}$ ) complicate an experimental verification of the presence of strain. The goal of this paper is to investigate whether strain in QDs can be measured with MeV ion-channeling.

## II Experimental

The QD samples were grown in a Varian GenII MBE system. A buffer layer consisting of 675 nm GaAs was grown on a [001] oriented GaAs wafer. Subsequently, a layer of 0.66 nm InAs (corresponding to two monolayers) was grown at a temperature of 555°C. Due to the 7% lattice mismatch of InAs (lattice constant of 0.605 nm) with respect to GaAs (lattice constant of 0.565 nm), three-dimensional islands are formed when more than 1.4 ML of InAs are grown. This self-assembly of three-dimensional islands is known as the Stranski-Krastanov growth mode. In between the islands a 1 ML thick wetting layer of InAs containing about 50% of the total In is present. The InAs is capped with 98 nm GaAs, 30 nm  $\text{Al}_{0.33}\text{Ga}_{0.67}\text{As}$  and 17 nm GaAs. The fluctuation in the size of these self-organized quantum dots can be as small as 10% and the InAs QDs are typically 10 nm in diameter and about 4 nm high depending on the growth conditions [2, 3].

For the ion beam analysis experiments, the QD-sample was placed in a 3-axes goniometer with an angular resolution  $< 0.005^\circ$  [4]. Channeling experiments have been performed using 4 MeV  $\text{He}^+$  ions from the 2-30 MeV AVF Cyclotron at the Eindhoven University of Technology. The beam divergence was  $0.09^\circ$  FWHM. Backscattered ions were detected with a 1200  $\text{mm}^2$  Canberra PIPS detector positioned at a scattering angle of  $160^\circ$ . A 11.4  $\mu\text{m}$  thick mylar stopper foil ( $\text{C}_{10}\text{H}_8\text{O}_4$ ) was placed in front of the detector to decrease the count rate of the GaAs substrate and to limit the pile-up. The energy straggling of the ions in the foil was approximately 28 keV. The energy resolution of the system is also determined by the kinematic spread over the detector (26 keV) and its intrinsic energy resolution ( $\sim 40$  keV). The resulting FWHM of the In peak was 55 keV, which is still significantly less than the energy separation of the In peak and the GaAs edge in the backscattering spectrum (168 keV). Consequently, angular scans of In can be recorded by plotting the integrated In yield as a function of angle. A second 10  $\text{mm}^2$  Canberra PIPS detector was positioned at a scattering angle of  $130^\circ$ . This detector was used to obtain angular scans of GaAs from Rutherford Backscattering Spectroscopy (RBS) spectra with a better energy resolution: the kinematic spread over the detector is smaller and energy straggling in a foil is absent. The angular scans through the [011] axes are performed with an angle of  $45^\circ$  between the surface normal of the sample and the incoming beam.

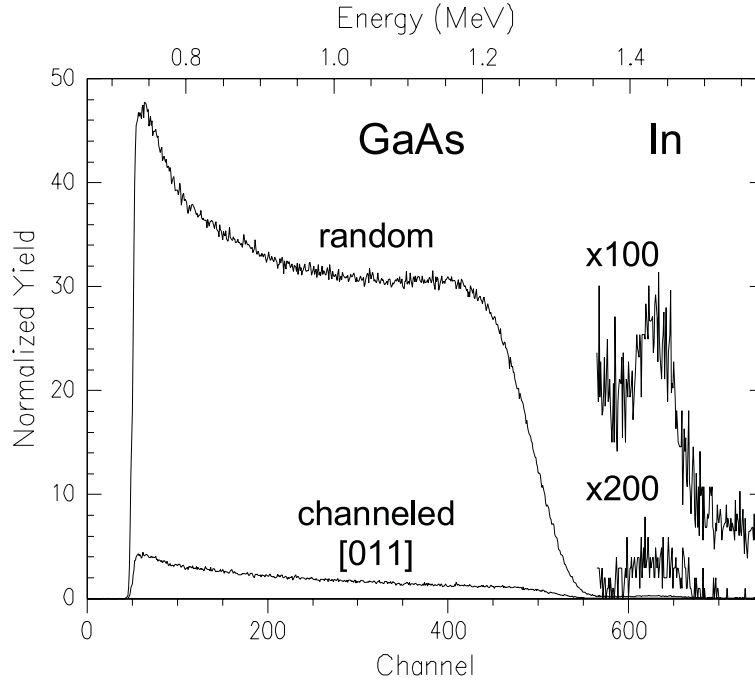


Figure 2.1: The random and [011] channeled RBS spectra of a QD-sample.

### III Results

Ion-channeling is usually applied in combination with RBS. This leads to energy (or depth) - yield spectra as presented in Fig. 2.1. Figure 2.1 shows the random and [011] channeled RBS spectra of a QD-sample measured with the 1200 mm<sup>2</sup> detector. The random spectrum was obtained during spinning the sample 90° around its surface normal after the beam has been tilted away from the [011] axis by 2°. The minimum yield is the ratio between the channeling and random yields. For GaAs these are the integrated yields (from the 10 mm<sup>2</sup> detector) from a depth of 6 to 16 nm in respectively the channeled and the random spectrum, while for In the channeling and random yields are the integrated yields of the entire In peak in respectively the channeling and random spectrum. The minimum yields found in this way are  $\chi_{min} = 3.5\%$  for GaAs and 18.0% for In. The FWHM of the In peak is 54 keV. The energy difference between the ions scattered on Ga and As is too small to identify these contributions separately.

To determine the exact direction of a crystal axis, the yield in a certain depth interval is measured as a function of the angle  $\psi$  between the incoming beam and the crystal axis. These so-called angular scans have been measured through the [011] and the [001] axis of a QD-sample, both in the (100) plane. They are shown in Fig. 2.2 (a) and 2.2 (b), respectively. In the same way as mentioned above the GaAs yield has been determined in the depth interval of 6 to 16 nm and the In yield has been determined from the entire In peak. Table I summarizes the measured half-widths  $\psi_{1/2}$ 's and minimum yields  $\chi_{min}$ 's of GaAs and In for both angular scans.

The interpretation of the angular scans is complicated by the limited height of the QDs of no more than approximately 4 nm and the presence of the InAs wetting layer.

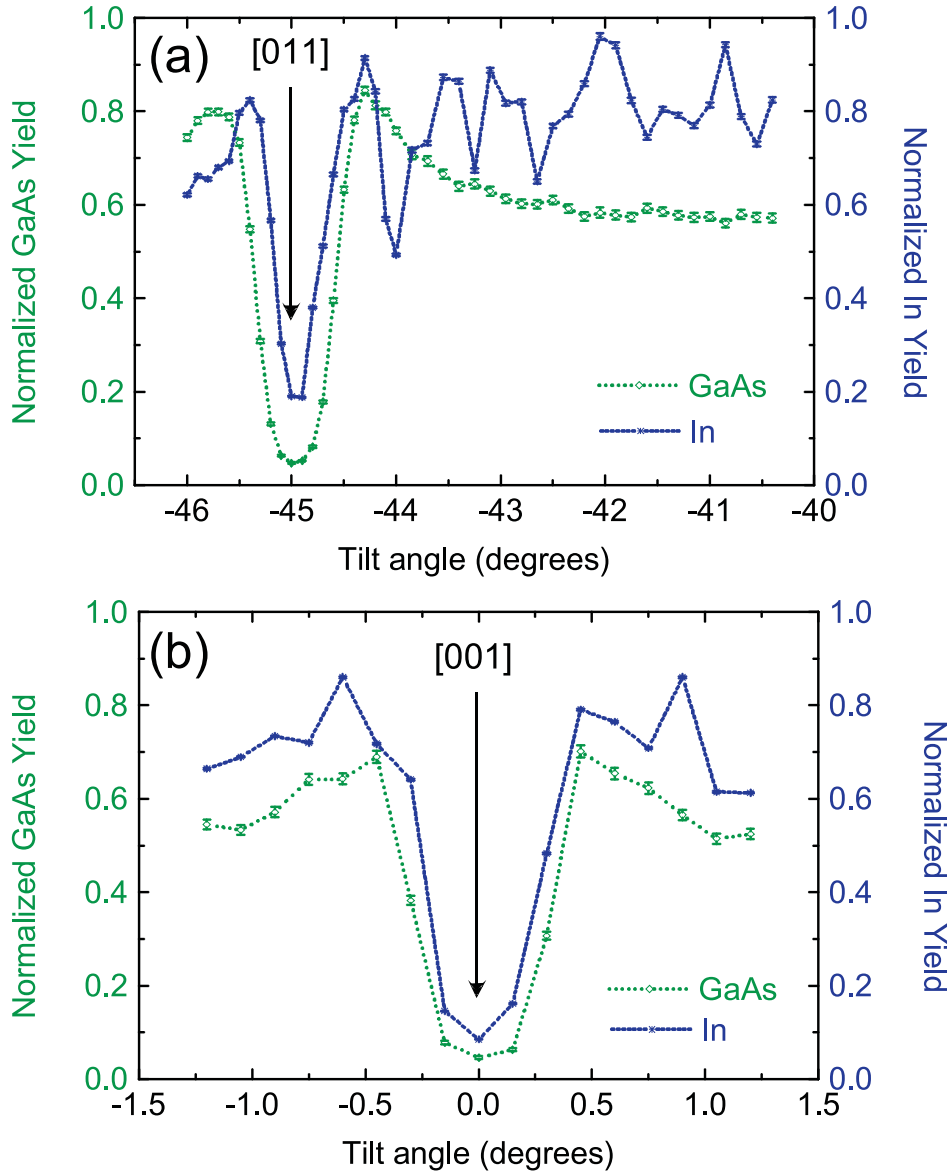


Figure 2.2: The measured scans through the [011] (a) and the [001] axis of a QD-sample (b).

For a buried ultra-thin homogeneous *layer* (4 nm) the length of the atomic strings along which the ion steering occurs is far below the typical lengths ( $\geq 10$  nm for ion energies  $\geq 4$  MeV) required to obtain channeling characteristics representative of the crystal structure of the ultra-thin layer. Consequently, the shape and position of an angular scan is not only representative for the ultra-thin layer (or QDs), but is also determined by the flux pattern (channeled or non-channeled) emerging from the overlying (GaAs) crystal reaching the ultra-thin layer (or QDs).

Furthermore, in the samples containing the QDs, about 50% of the In is in the tetrago-

Table 1: The measured half-widths and minimum yields for the GaAs capping layer and In in the QDs.  $\psi_{1/2}$  is taken from Fig. 2.2, while  $\chi_{min}$  results from comparison with the random yield.

	$\psi_{1/2}$ ( $^{\circ}$ )	$\chi_{min}$ (%)
GaAs [011]	$0.69 \pm 0.02$	$3.3 \pm 0.1$
GaAs [001]	$0.60 \pm 0.02$	$3.5 \pm 0.1$
In [011]	$0.44 \pm 0.02$	$18.0 \pm 2.0$
In [001]	$0.50 \pm 0.02$	$8.6 \pm 1.4$

nally deformed homogeneous wetting layer. Because this wetting layer is only 1 ML thick, the channeling behavior of the In signal from this wetting layer will be determined by the position of the In atoms in the flux pattern emerging from the GaAs capping layer.

## Strain

Using Poisson's ratio  $\nu = 0.35$  for InAs [5] the tetragonal distortion of a fully strained homogeneous InAs film on a GaAs crystal without relaxation (like the wetting layer in the QD samples) is  $\varepsilon_T = 0.10$ . Consequently, for a fully strained InAs layer on GaAs the position of the [011] axis with respect to the [011] axis of the cubic GaAs substrate is shifted by  $4.0^{\circ}$  towards the [001] axis.

To relieve the strain in the InAs layer during growth, QDs are formed, because strain energy can be relieved via surface tension, which in turn can be lowered by enlarging the surface. The surface tension can be minimized by creating crystal planes with the lowest surface energy. Crystal growth will also be lowest perpendicular to these planes and they will become the boundaries of the crystal. For zinc-blende-type of lattices the planes with the lowest surface energy are the {111} planes [6] and although the shape of the QDs is a controversial point in literature, a truncated pyramid shape with the {111} planes as sides is generally accepted [7,8]. When the free-standing QDs are capped with GaAs, the strain energy increases again and the presence of significant tetragonal distortion within the QD can not be excluded. The strain present in the InAs *wetting layer* induces a shift of the [011] axis of  $4.0^{\circ}$ , which is the upper limit for the distortion in the QDs.

Figure 2.2(a) shows that the minimum of the angular scan through the [011] axis in the (100) plane of the In signal coincides with the minimum of the angular scan through the [011] axis in the (100) plane of the GaAs signal. When the channeling behavior is assumed to be determined by the InAs strings, this would imply the absence of tetragonal distortion in the InAs QDs. However, under this assumption, Fig. 2.2 reveals an anomaly in the width of both angular In scans. For a *bulk* InAs crystal the half-width  $\psi_{1/2}$  is proportional to the characteristic angle  $\psi_1$  as defined in the Lindhard model [9]:

$$\Psi_1 = \left( \frac{2Z_1 Z_2 e^2}{4\pi\epsilon_0 E d} \right)^{1/2}, \quad (2.1)$$

in which the atomic number of the incoming particle and the target atom are represented

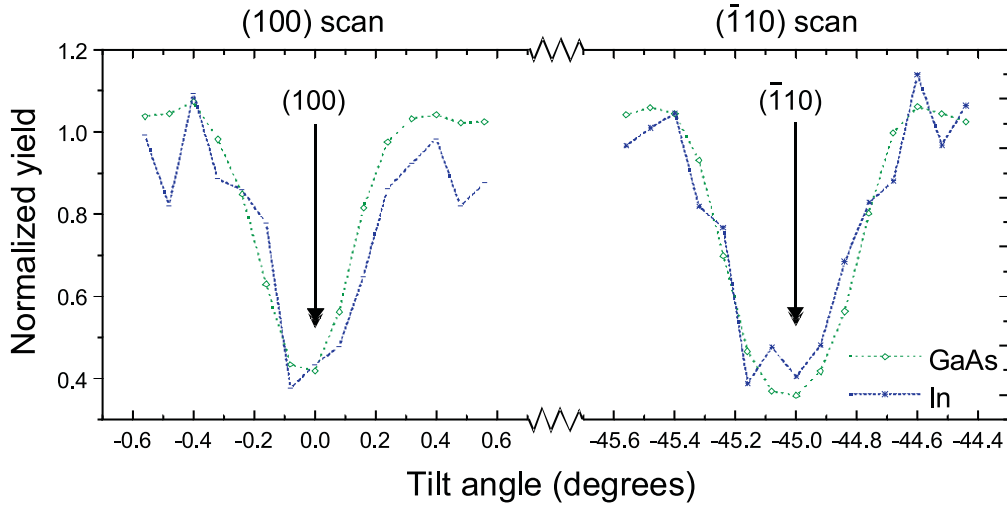


Figure 2.3: The measured scans through the (100) and the  $(\bar{1}10)$  planes of a QD-sample.

by  $Z_1$  and  $Z_2$  respectively,  $E$  is the energy of the incoming particle and  $d$  is the lattice spacing along the channeling direction. The half-width  $\psi_{1/2}$  is related to the characteristic angle  $\psi_1$  by a constant  $C_\psi$  ( $\approx 1$ ), which depends predominantly on the vibrational amplitude of the atoms:  $\psi_{1/2} = C_\psi \psi_1$  [10]. An In angular scan in bulk InAs is thus expected to be broader than a GaAs angular scan in bulk GaAs, because of the larger  $Z_2$ . With a 4 MeV  $\text{He}^+$  beam and an average  $Z_2 = 32$  for GaAs the characteristic angles are  $\psi_1(\langle 001 \rangle) = 0.52^\circ$  ( $d = 0.565$  nm) and  $\psi_1(\langle 011 \rangle) = 0.62^\circ$  ( $d = 0.400$  nm). For the In strings in InAs ( $Z_2 = 49$ ) these characteristic angles are  $\psi_1(\langle 001 \rangle) = 0.62^\circ$  ( $d = 0.606$  nm) and  $\psi_1(\langle 011 \rangle) = 0.74^\circ$  ( $d = 0.429$  nm) respectively.

The characteristic angles for InAs have also been obtained by measurements on a [001] oriented bulk InAs wafer. The measured half-widths are  $\psi_{1/2} = (0.65 \pm 0.02)^\circ$  ( $C_\psi = 1.05$ ) and  $\psi_{1/2} = (0.77 \pm 0.02)^\circ$  ( $C_\psi = 1.04$ ) for the [001] and [011] axes respectively. Undoubtedly, the half-widths for both the [001] and [011] axial direction of the InAs QDs in GaAs are anomalously small compared to both the calculated and measured characteristic angle.

From Table I the ratio of the half-widths of the [001] and [011] angular scans of the GaAs is consistent with the predicted dependence, but the ratio of the  $\psi_{1/2}$  values for the [001] and [011] angular scans of the InAs QDs is opposite to that expected for a bulk InAs crystal. One possible explanation could be that the QDs have a crystal orientation with the [011] axis of the InAs lined up with the [001] axis of the GaAs substrate! Such an orientation can easily be verified by measuring for example the orientation of the  $\{001\}$  and  $\{011\}$  planes and the  $\langle 111 \rangle$  axes relative to the surface normal, because they will be different for [001] and [011] oriented crystals. The [001] axis is intersected by two (011) planes and two (001) planes, symmetrically placed at  $45^\circ$  rotation. The [011] axis has one (011) plane and one (001) plane perpendicular to each other and also two (111) planes at  $35.3^\circ$  on either side of the (011) plane. Figure 2.3 shows the results of measurements on the orientation of the planes in the QD. It can be seen that the orientation of these planes coincides with those of the [001] grown GaAs, thus the InAs seems to be [001] oriented in

spite of the peculiar ratio of the  $\psi_{1/2}$  values from the In angular scans.

Calculations show that small displacements from substitutional sites (which is the case for the position of the In atoms in the wetting layer compared to the strings of the GaAs capping layer) result in a significant narrowing of the angular yield curve [11]. It is however important to realize that for displacements caused by tetragonal distortion this narrowing would only apply for angular scans for off-normal axes, because the In atoms in the wetting layer have a displacement perpendicular to the channeling direction only for off-normal axes. Thus the geometry of the wetting layer influences only the measured half-width of the In angular scan for the [011] axis in the QD sample, being smaller than in a perfect bulk InAs crystal. But, from Fig. 2.2(b) it can be seen that the In angular scan is also smaller than the GaAs angular scan for the [001] axis. This implies that the narrowing is also a result of the specific crystal structure of the InAs in the QDs.

## Minimum yield

In channeling experiments the formation of a shadow cone reduces the nuclear encounter probability for atoms in a string, i.e. the first few atoms in a string shield the underlying atoms from the incoming particles. The first few atoms which have a substantial contribution to the formation of this shadow cone give rise to a surface peak. This is the peak in the yield of a *channeled* RBS spectrum that usually can be seen, because the nuclear encounter probability is much higher for the first few atoms in the strings in case of channeling. The number of atoms with a substantial contribution to this surface peak can be estimated from the number of atoms in a string (in terms of an areal density) contributing to the surface peak, which can be determined according to Feldman *et al.* [12] using the Coulomb shadow cone radius  $R_C$  and the two-dimensional, root-mean-square vibrational amplitude normal to the beam,  $\rho$ , which depends on the temperature. Computer calculations allowed to generate a universal curve, making it possible to calculate the surface peak intensity (atoms/row) from the ratio of  $\rho$  to the Molière radius  $R_M$ , which in turn can be calculated from  $R_C$ .

In our experiments the energy of the incoming particle is  $E = 4$  MeV, the atomic number of the incoming particle is  $Z_1 = 2$  and of the target particle is  $Z_2 = 49$  (In),  $\rho$  is taken 15 pm for InAs [13] and the lattice spacing  $d$  depends on the channeling direction. Under these conditions 5 (whole) atoms/string contribute to the surface peak for In strings along the  $\langle 001 \rangle$  axes and 6 atoms/string for In strings along the  $\langle 011 \rangle$  axes of a perfect InAs crystal [12]. These sums contain substantial contributions (contribution to the total surface peak  $> 1\%$ ) from approximately 9 and 11 atoms in a string respectively. If a uniform flux impinges on a layer that consists of all the atoms that have a substantial contribution to the surface peak, the minimum yield of this layer will be approximately 50%.

Figure 2.4 shows the results of nuclear encounter probability calculations for In atoms in a string along the [011] and the [001] axes of a bulk cubic InAs crystal with 4 MeV  $\text{He}^+$  ions as incoming particles. These calculations were done with the FLUX6 simulation package [14], which calculates the two-dimensional root-mean-square vibrational amplitude normal to the beam using a Debye temperature of 249K [15]. The sum of the nuclear encounter probabilities as a function of the number of atoms in a string is plotted

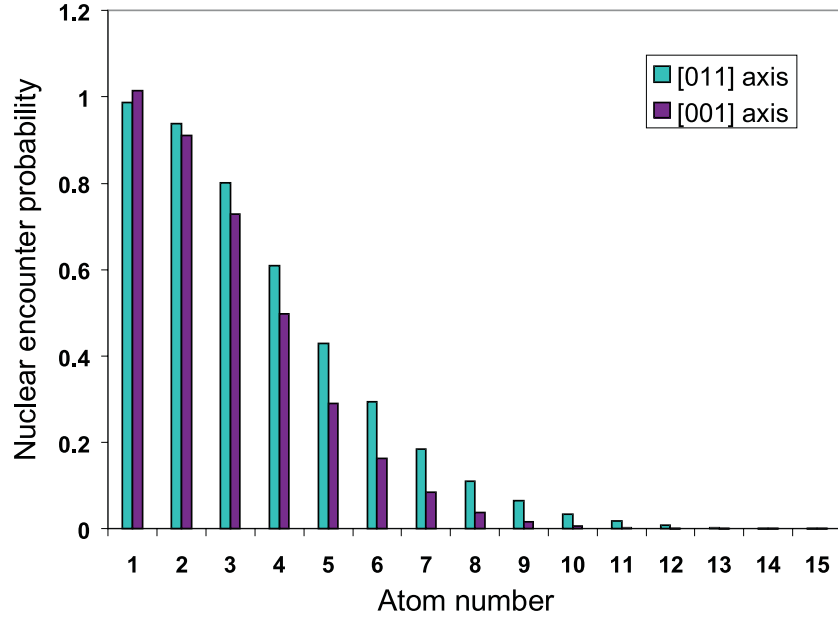


Figure 2.4: The nuclear encounter probability of the atoms in (011) and (001) axes of a cubic InAs lattice as calculated with the FLUX6 simulation package.

in Fig. 2.5. In this graph it can be seen that the contribution of the next atom to the surface peak is smaller than 1% from 8 atoms on for (001) axes and from 10 atoms on for (011) axes. This is in good agreement with the estimation made before.

For zinc-blende-type of lattices the  $60^\circ$  perfect dislocation is the most probable type of misfit dislocation to relieve *compressive* tetragonal strain (epitaxial growth of InAs on GaAs), when the layer is grown thicker than the critical layer thickness [6]. The perfect dislocations glide through the  $\{111\}$  planes and they are called perfect because the stacking sequence of the  $\{111\}$  planes remains intact. At the substrate interface however, dislocation lines are formed. Only 1 ML is involved in the relaxation of compressive tetragonal strain via perfect dislocations in the  $\{111\}$  planes, while the rest of the crystal on both sides of the perfect dislocation is not deformed. If the QDs have the equilibrium cubic InAs lattice structure, the misfit with the GaAs crystal is most likely occurring in the  $\{111\}$  planes, which form the boundaries of the pyramidal QDs. Then, due to the 7% lattice mismatch of InAs with the GaAs the flux pattern emerging from the GaAs averages out and appears as a uniform flux to the buried relaxed InAs QDs. Just like a surface peak occurs for a non-buried InAs surface, an interface peak will occur in this case.

STM and TEM measurements show that the QDs have a height of  $\sim 4$  nm [16]. For the [001] direction this corresponds to a maximum string length of 6.6 atoms. Considering the truncated pyramid shape of the QDs an estimated maximum average string length of about  $4\frac{1}{2}$  atoms InAs is seen by the channeled  $\text{He}^+$  ions, which is far less than the 8 atoms calculated to have a substantial contribution to the interface peak. For the [011] direction the maximum string length is 13.2 atoms and the estimated maximum average string length is about 9 atoms in the QDs, while the first 10 atoms in a string would contribute to the interface peak. Thus, if the InAs in the QDs is fully relaxed via  $60^\circ$

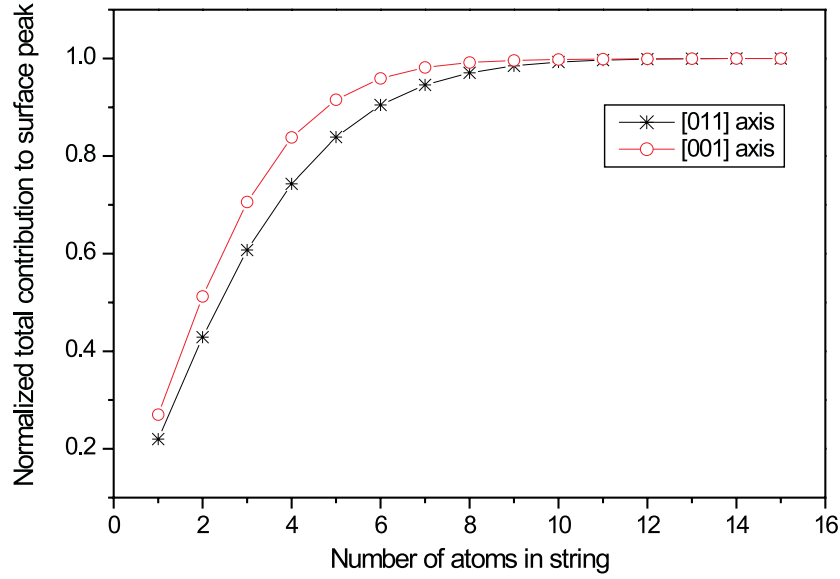


Figure 2.5: The sum of the nuclear encounter probabilities of the first few atoms in (011) and (001) strings of a cubic InAs lattice as calculated with the FLUX6 simulation package.

perfect dislocations, the minimum yield from the In in the QDs is expected to be at least 50% of the random yield for the [011] axis.

The minimum yield from the In atoms in the wetting layer is fully determined by their position in the flux pattern emerging from the GaAs channels in the capping layer. Because the InAs wetting layer is fully strained, for the [011] axis the In atoms will be shifted 28% towards the centre of the GaAs channels. Feldman *et al.* give a model that roughly describes the depth independent spatial flux distribution within the channels as a function of angle of incidence relative to the channel axis assuming cylindrical symmetry and the small  $r$  approximation to the standard potential [17]. From this model for incidence parallel to the channels the flux at 28% of the distance to the centre of the channel is about 10% of the flux for random incidence. Then, the minimum yield of the In atoms in the wetting layer will also be about 10% for the [011] axis. For the [001] axis the In atoms are not shifted and the minimum yield will be a little lower than for the surrounding GaAs, because of the higher atomic number.

Remembering that half of the In atoms are in the QDs and half of them are in the wetting layer, the separate contributions to the minimum yield can be combined. If the QDs would relieve their strain completely via  $60^\circ$  perfect dislocations, the total In minimum yield has to be at least 30% for the [011] axis and 25% for the [001] axis. However, from Table I it is clear that the measured minimum yield values are significantly less for both axes.

## Strain fields

From the discussion presented above it can be concluded that the interface between the InAs QDs and the GaAs capping layer does not behave like the interface between a cubic InAs film and a cubic GaAs capping layer. The minimum yield values must be the result



of deformation in and around the QDs: apparently, the crystal lattices of the capping layer and the QDs are distorted near the interface in such a way that the channeled particles are steered from the GaAs channels into the InAs channels, i.e. the strings in the GaAs capping layer continue in the strings in the InAs QDs! These channeling experiments thus provide evidence for the presence of extended strain fields in the GaAs required to induce steering into the InAs, which typically occurs at a length scale of  $\geq 10$  nm for 4 MeV  $\text{He}^+$  ions in GaAs and InAs. In literature, strain fields in and around the InAs QDs have been suggested [1, 8, 18–20]. It is interesting to note that the experimentally found width of the base of the pyramids ( $\sim 10$  nm) is able to accommodate one unit cell of GaAs more than unit cells of InAs. If the strain would relieve via misfit dislocations, this would result in 2 GaAs half-planes per QD. Although these misfit dislocations can not be excluded from our ion-channeling experiments, the optical performance of the QDs and STM measurements point to absence of these misfit dislocations [16, 21]. Thus, the QD and the surrounding GaAs crystal structure is pseudomorphic and it must be concluded that the difference in lattice constant of the InAs and GaAs induces strain fields which induce steering of the ions in a similar fashion as known to occur in the presence of misfit dislocations.

Furthermore, in the areas of a crystal which induce ion steering the half-widths will be smaller than measured in a perfect crystal: the ions in the flux distribution in the channels which come closest to the strings, will have a greater probability of being dechanneled in a curved crystal, than in a perfect crystal, depending on the curvature. In combination with the channeling behavior in the wetting layer this qualitatively explains the measured half-widths in the In angular scans for both the [001] and [011] directions.

## IV Conclusions

The present measurements confirm previous speculations about possible strain in and around QDs and exclude the presence of  $60^\circ$  perfect dislocations. The lattice mismatch between the InAs islands and the GaAs substrate causes strain fields, which extend from the QDs into the surrounding GaAs matrix over a typical length scale of  $\geq 10$  nm. These extended strain fields induce steering of the channeled particles from the GaAs channels into the InAs channels. This explains the observed channeling behavior, i.e. the measured minimum yields are low, despite that the QDs are too thin for shadow cone formation, and the half-widths of the angular scans are anomalously small.

## Acknowledgements

The authors wish to thank Willem van der Vleuten for growing the samples, Maarten Leys for sharing with us his knowledge on the growth mechanisms of the QDs, and John Davies for fruitful discussions on the interpretation of the measurements.

## References

- [\*] Author to whom correspondence should be addressed. FAX: +31 40 243 80 60. Present address: Cyclotron Laboratory, Department of Applied Physics, Eindhoven University of Technology, P.O. Box 513, 5600 MB Eindhoven, The Netherlands. Electronic address: L.J.van.Ijzendoorn@tue.nl.
- [1] T. Y. Wang, and G. B. Stringfellow, *J. Appl. Phys.* **67**, 344 (1990).
- [2] S. Guha, A. Madhukar, and K. C. Rajkumar, *Appl. Phys. Lett.* **57**, 2110 (1990).
- [3] L. Goldstein, F. Glas, J. Y. Marzin, M. N. Charasse, and G. L. Roux, *Appl. Phys. Lett.* **47**, 1099 (1985).
- [4] P. W. L. Van Dijk, Ph.D. thesis, Eindhoven University of Technology, 1997.
- [5] D. R. Lide, *Handbook of Chemistry and Physics, 75th edition* (CRC Press, Cleveland, 1994), Chap. 12, p. 32.
- [6] J. W. Matthews, *Epitaxial Growth, Part B* (Academic Press, New York, 1975).
- [7] M. Grundmann, N. N. Ledentsov, O. Stier, D. Bimberg, V. M. Ustinov, P. S. Kopev, and Zh. I. Alferov, *Appl. Phys. Lett.* **68**, 979 (1996).
- [8] S. Ruvimov, and K. Scheerschmidt, *Phys. Stat. Sol. (a)* **150**, 471 (1995).
- [9] D. S. Gemmell, *Rev. Mod. Phys.* **46**, 129 (1974).
- [10] J. R. Tesmer, and M. Nastasi, *Handbook of Modern Ion Beam Analysis* (Materials Research Society, Pittsburgh, 1995), Chap.10.
- [11] S. T. Picraux, W. L. Brown, and W. M. Gibson, *Phys. Rev. B* **6**, 1382 (1972).
- [12] L. C. Feldman, J. W. Mayer, and S. T. Picraux, *Materials Analysis by Ion Channeling* (Academic Press, New York, 1982), Chap. 1, p. 18-26.
- [13] J. F. Vetelino, S. P. Gaur and S. S. Mitra, *Phys. Rev. B* **5**, 2360 (1972).
- [14] P. J. M. Smulders, and D. O. Boerma, *Nucl. Instr. and Meth. B* **29**, 471 (1987).
- [15] D. R. Lide, *Handbook of Chemistry and Physics, 75th edition* (CRC Press, Cleveland, 1994), Chap. 12, p. 94.
- [16] W. Warren, J. R. Tucker, G. S. Solomon, and J. S. Harris Jr., *Appl. Phys. Lett.* **71**, 1083 (1997).
- [17] L. C. Feldman, J. W. Mayer, and S. T. Picraux, *Materials Analysis by Ion Channeling* (Academic Press, New York, 1982), Chap. 3, p. 73-79.
- [18] A. Rosenauer, U. Fischer, D. Gerthsen, and A. Förster, *Appl. Phys. Lett.* **71**, 3868 (1997).
- [19] M. Grundman, O. Stier, and D. Bimberg, *Phys. Rev. B* **52** (16), 11.969 (1995).

- [20] Q. Xie, A. Madhukar, P. Chen, and N. P. Kobayashi, *Phys. Rev. Lett.* **75** (13), 2542 (1995).
- [21] A. W. E. Minnaert, A. Y. Silov, J. E. M. Haverkort, and J. H. Wolter, in *Proceedings of the 24th International Conference on the Physics of Semiconductors, Jerusalem, Israel, August 2-7, 1998*, edited by David Gershoni (World Scientific, Jerusalem, 1998), Sect. VII B, 36.

# 3. Ion-channeling for strain analysis in buried nano-films ( $< 6$ nm)

L. J. M. Selen, F. J. J. Janssen, L. J. van IJzendoorn [a], and M. J. A. de Voigt

*Research Institutes CPS and COBRA, Cyclotron Laboratory, Department of Applied Physics, Eindhoven University of Technology, P.O. Box 513, 5600 MB Eindhoven, The Netherlands*

M. J. J. Theunissen

*Materials Science Center, University of Groningen, Groningen, The Netherlands*

P. J. M. Smulders

*Philips Research Laboratories, Eindhoven, The Netherlands*

T. J. Eijkemans

*Research School Cobra, Department of Applied Physics, Eindhoven University of Technology, Eindhoven, The Netherlands*

A new method has been developed to measure the tetragonal distortion in buried strained nano-films ( $< 6$  nm) with MeV ion-channeling. For MeV ion-channeling the presence of a  $2.2 \pm 0.2$  nm thick buried  $\text{Si}_{1-x}\text{Ge}_x$  nano-film leads to a step in the yield of the Si host crystal in an axially channeled Rutherford backscattering spectrum for off-normal crystal axes. The height of this step depends on the angle  $\psi$  between the incoming beam and the crystal axis. Two maxima in the step height appear as a function of the angle  $\psi$  and with Monte Carlo simulations the angular separation between these appearing maxima can be related to the tetragonal distortion in the buried  $\text{Si}_{1-x}\text{Ge}_x$  nano-film. A universal curve is derived which allows to determine the tetragonal distortion from ion-channeling experiments, for a given film thickness. The results are compared with the outcome of XRD measurements.

## I Introduction

In modern semiconductor technology, films with a thickness in the nanometer regime (nano-films) are of increasing importance. Particularly interesting are singly crystalline

metastable strained films, which are applied in semiconductor devices such as high electron mobility transistors, solid state lasers, heterojunction bipolar transistors, and tunnel junctions. In strained films the lattice deformation determines the band gap and the density of states (DOS), and thus the device properties. Characterization of the lattice deformation is therefore of vital importance, and becomes an increasing challenge when the layer thickness decreases.

X-ray diffraction (XRD) is a well-known technique to investigate strain in thin films [1–3]. With high resolution XRD it is possible to characterize depositions of less than one monolayer (ML), when they are grown in a super lattice structure; to analyze a sub-ML-thickness film, sixty periods are needed [4]. However, the semiconductor devices mentioned above contain only one nano-film.

Another well-known technique to investigate strain in thin films is MeV ion-channeling. Usually it is restricted to the analysis of thin films with a thickness typically larger than approximately 20 nm. The tetragonal distortion is measured by the shift of a so-called angular scan of the strained film with respect to the angular scan of the underlying host crystal along off-normal axes. A necessary condition for this procedure is a decrease of the scattering probability in the epitaxial film, induced by shadow cone formation along the atomic strings. When the epitaxial films are situated at the surface and are getting extremely thin ( $< 10$  nm), this can only be pursued by lowering the incident energy as demonstrated by the highly specialized medium energy ion scattering (MEIS) techniques [5–8].

Ion beams with higher energies (2 MeV) are commonly available for standard Rutherford backscattering spectrometry (RBS) analysis, which allows to measure samples with buried nano-films. When in a buried commensurate nano-film the length of the atomic strings is far below the typical lengths required to obtain an angular scan ( $\geq 20$  nm for ion energies  $\approx 2$  MeV), the value of the strain can no longer be determined from the shift of that angular scan. In such a case, the shape and position of an angular scan are not representative for the nano-film, and are primarily determined by the flux distribution (channeled or non-channeled) emerging from the capping crystal reaching the nano-film. Along the off-normal axes of the host crystal, the presence of such a film has the same effect as a stacking fault. Consequently, for channeling along off-normal axes, a sudden increase of the scattering yield can be measured. The strain in the thin film and its thickness determine the increase of the scattering yield. The magnitude of this step depends on the translation of the atomic strings with respect to the flux distribution emerging from the capping layer. Thus, this method basically provides a possibility to investigate nano-films without looking at the atoms in the film. With Monte Carlo simulations the increase in scattering yield can be related to the strain and thickness of the tetragonally deformed film.

Nowadays, singly crystalline layers with a thickness in the nm range can be accurately grown by atmospheric pressure chemical vapor deposition (APCVD). Preliminary measurements on 2.2 nm thick  $\text{Si}_{1-x}\text{Ge}_x$  films in Si grown 280 nm below the surface demonstrated a relation between the translation of the host crystal and the magnitude of the increase of the scattering yield [9]. This paper will describe the coherence between the translation of the host crystal caused by a strained nano-film and the observed magnitude of the increase in the scattering yield for measurements with  $\text{He}^+$  ions in the energy range

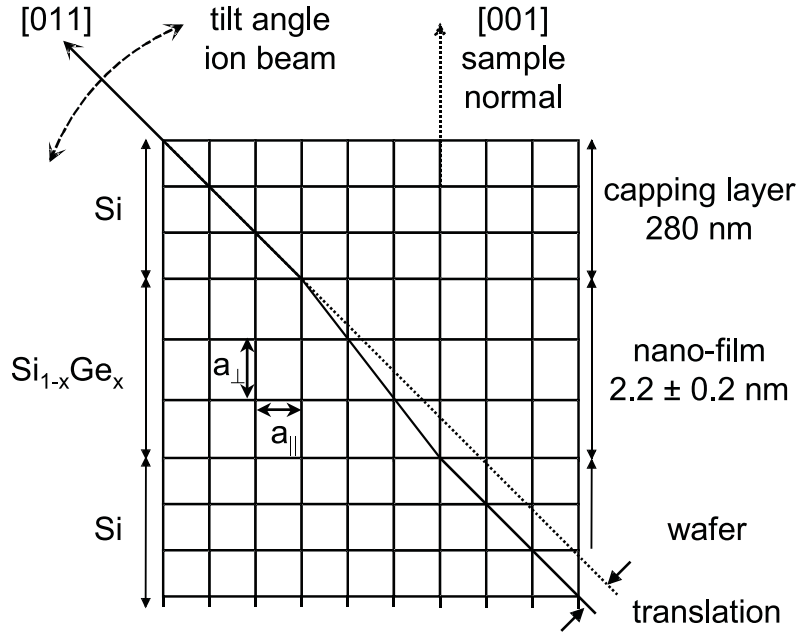


Figure 3.1: Schematic drawing of the sample. The main crystal directions, the direction of the angular scans, the lattice constants, and the translation of the strings of the Si wafer are indicated.

of 2–3.5 MeV. Furthermore, XRD measurements and simulations on the same samples will be presented.

## II Experimental

Buried  $\text{Si}_{1-x}\text{Ge}_x$  nano-films in Si have been grown by APCVD on a 6'' (001) oriented Si wafer at Philips Research Laboratories Eindhoven. At first the wafer was cleaned with  $\text{H}_2$  at a temperature of  $1100^\circ\text{C}$ , and then a 5.0 nm Si buffer layer was grown at  $625^\circ\text{C}$ . Subsequently, a 2.2 nm thick  $\text{Si}_{1-x}\text{Ge}_x$  film was grown by deposition of  $\text{GeH}_4$  and  $\text{SiCl}_2$  at  $625^\circ\text{C}$ . Finally, a 280 nm Si capping layer was deposited at  $700^\circ\text{C}$ . Two different samples were prepared: the first sample contains  $(4.6 \pm 0.3) \times 10^{15}$ , the second sample  $(6.4 \pm 0.3) \times 10^{15}$  Ge/cm<sup>2</sup>, as determined by 2 MeV Rutherford backscattering spectrometry (RBS) analysis. The thickness of the  $\text{Si}_{1-x}\text{Ge}_x$  films was measured by high resolution TEM (HRTEM) to be  $(2.2 \pm 0.2)$  nm for both samples. The Ge concentration of the samples amounts to  $(45 \pm 5)\%$  and  $(63 \pm 6)\%$ , respectively. In the remainder of this paper these samples will be referred to as the 45 and 63% sample. A schematic drawing of the samples is shown in Fig. 3.1.

The tetragonal distortion is a quantity for the strain defined as  $\varepsilon_T = \varepsilon_\perp - \varepsilon_\parallel = (a_\perp - a_\parallel)/a_V$ , where  $a_\perp$  is the perpendicular lattice constant,  $a_\parallel$  the in-plane lattice constant, and  $a_V$  the Vegard crystal lattice constant for a bulk crystal with composition of the commensurate film. The in-plane strain  $\varepsilon_\parallel$  and the perpendicular strain  $\varepsilon_\perp$  are defined as the relative deviations of the lattice constants from the virtual crystal lattice

constant. With the assumption of no dislocations, the tetragonal distortion in the film is  $\varepsilon_T = 0.033$  and  $0.046$  for the 45 and 63% sample, respectively. For a thickness of 2.2 nm, this leads to translations of the substrate  $\langle 011 \rangle$  strings relative to those of the capping layer of 0.051 and 0.072 nm for the 45 and 63% samples, respectively (see Fig. 3.1).

The ion-channeling experiments have been performed with 2-3.5 MeV  $\text{He}^+$  ion beams from the Philips AVF Cyclotron at Eindhoven University of Technology. The beam currents were between 5 and 30 nA. In order to compare the experiments quantitatively, a rotating vane with a 88 nm thick gold film is placed in the ion beam to measure the ion dose. The energy of  $\text{He}^+$  ions scattered from the rotating vane is measured with a 25 mm<sup>2</sup> Canberra Passivated Implanted Planar Silicon (PIPS) detector with an energy resolution of 15 keV.

For the ion-channeling experiments the samples were placed in a 3-axes goniometer with an angular resolution  $< 0.005^\circ$  [10]. With two sets of slits the beam divergence was set to  $0.07^\circ$  FWHM. Backscattered ions were detected with a 100 mm<sup>2</sup> Canberra PIPS detector with a resolution of approximately 17 keV, positioned at a backscattering angle of  $130^\circ$ . For axial channeling measurements a series of channeling spectra was obtained by varying the tilt angle  $\psi$  between the incoming beam and the  $[011]$  axis of the sample (see Fig. 3.1).

XRD measurements were performed with a Bede model 200 high resolution (0.5 arc-second) research diffractometer set-up with a Bede channel cut collimator with a Si  $\langle 111 \rangle$  reference crystal at the Eindhoven University of Technology. The  $K\alpha_1$  X-rays from a 2.2 kW Cu long fine focus source are detected with a NaI scintillation crystal and photomultiplier, which gives a dynamical range of 0.1 - 250,000 counts. In a  $\theta, 2\theta$ -measurement the samples were investigated by glancing incidence measurements on the  $\{113\}$  planes with the detector at  $56^\circ$ .

### III Channeling

Figure 3.2 shows a typical RBS spectrum of the 63% sample with a step in the yield of the channeled spectrum at the depth of the strained nano-film, measured at a backscattering angle of  $130^\circ$ . The spectrum is one of the spectra obtained in an angular scan through the  $[011]$  axis in the  $\{001\}$  plane. The sample was rotated over  $0.16^\circ$  from the  $[011]$  axis of the capping layer towards the  $[001]$  surface normal in the  $\{100\}$  plane. The step in the spectrum due to the presence of the strained nano-film is magnified in Fig. 3.2 (b). Since the stopping power for channeled ions depends on the detailed trajectories in the channels [11], the exact depth in nm at which the nano-film is situated can not be determined easily from spectra in channeling experiments.

The step height in the yield depends on the position of the atomic strings of the Si wafer relative to those of the capping layer. In Fig. 3.3 the step height in the spectrum is plotted as a function of the angle  $\psi$  for both samples. The experimentally found data points in Fig. 3.3 are taken from the channeled spectra after they have been normalized to the counts in the Au peak of the rotating vane and the step heights are normalized to the highest step in the angular scans. Figure 3.3 shows that for both the 45 and 63% samples, two maxima appear in the curve of the step height as a function of the angle

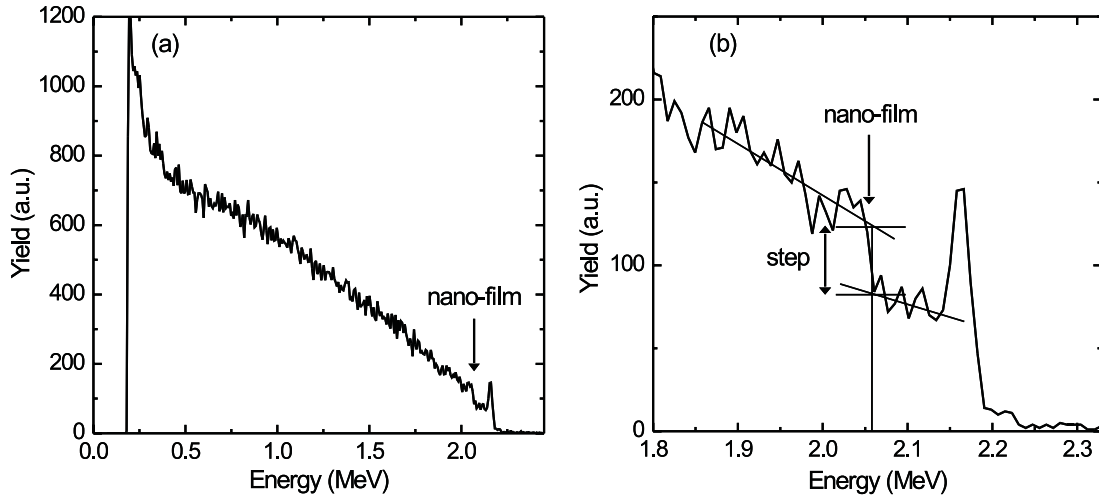


Figure 3.2: RBS spectrum of the 63% sample tilted  $0.16^\circ$  away from the  $[011]$  axis of the Si capping layer using 3.5 MeV  $\text{He}^+$  ions (a). The energy interval around the step in the spectrum is magnified in (b).

$\psi$ . It is remarkable that the angular separation between the two maxima  $\psi_{max}$ , which is estimated with the guiding lines, is larger for the 45% sample, in which the atomic strings of the substrate are translated less. Furthermore, the curves are not completely symmetrical in  $\psi$ .

Similar experiments were performed with 2 MeV  $\text{He}^+$  ions [9], and here too the angular separation  $\psi_{max}$  was larger for the 45% sample and the curves were not completely symmetrical in  $\psi$ . Table I shows the values of  $\psi_{max}$  for both samples and both energies. The values of  $\psi_{max}$  are larger for the measurements at 2 MeV. Notice that the characteristic angle  $\psi_1$ , which is a measure of the maximum incidence angle for ions to be captured in a channel and scales with the energy as  $E^{-1/2}$ , is larger at 2 than at 3.5 MeV. To the first approximation, the angular dependence of the channeled equilibrium flux distribution scales with the critical angle  $\psi_1$  [12], and therefore,  $\psi_{max}$  can be scaled with  $\psi_1$ . The ratios of  $\psi_{max}$  and  $\psi_1$  are given in the fourth and fifth column of Table I, and within the uncertainty of the measurements  $\psi_{max}$  indeed scales with  $\psi_1$ . Thus, the angular separation  $\psi_{max}$  depends on the translation of the crystal axes of the substrate. In the next section, an analytical flux distribution model is used to explain the observed channeling behaviour.

Table I: Values of  $\psi_{max}$  from ion-channeling experiments with 2 and 3.5 MeV  $\text{He}^+$  ions, and these values scaled to the characteristic angle  $\psi_1$ .

	$\psi_{max}(2 \text{ MeV})$	$\psi_{max}(3.5 \text{ MeV})$	$\psi_{max}/\psi_1(2 \text{ MeV})$	$\psi_{max}/\psi_1(3.5 \text{ MeV})$
45% sample	$0.55 \pm 0.02^\circ$	$0.44 \pm 0.02^\circ$	$0.94 \pm 0.03$	$0.99 \pm 0.03$
63% sample	$0.49 \pm 0.02^\circ$	$0.39 \pm 0.02^\circ$	$0.83 \pm 0.03$	$0.88 \pm 0.03$
$\psi_1$	$0.587^\circ$	$0.444^\circ$		



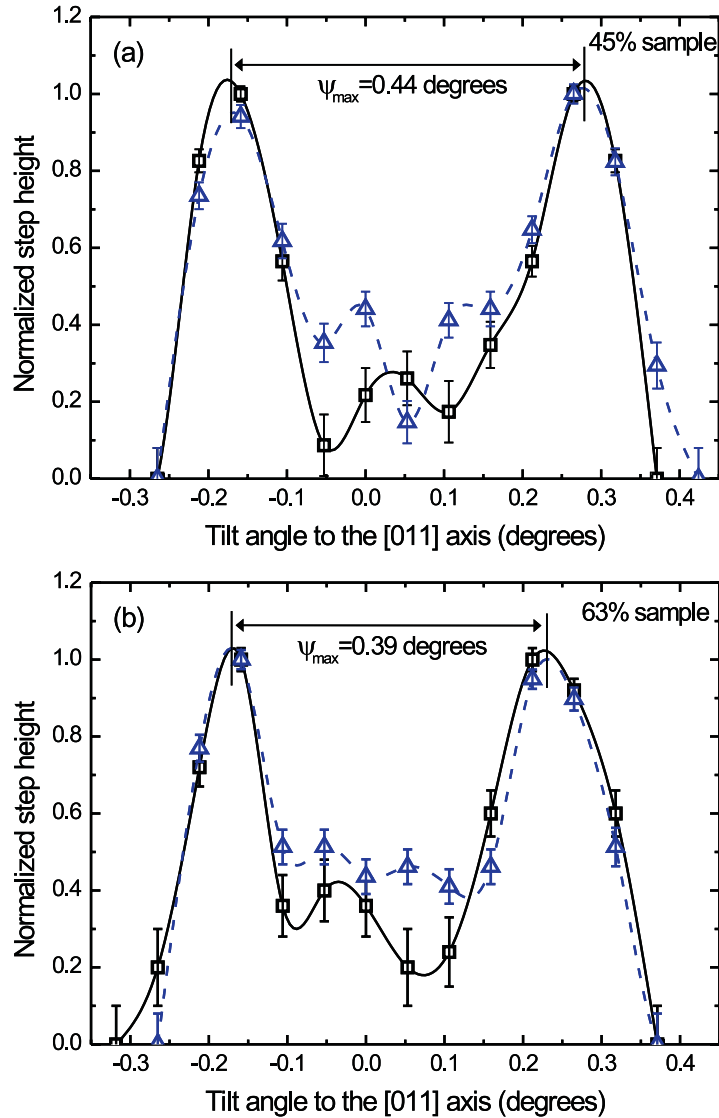


Figure 3.3: Experimental normalized step height in the Si yield (squares) and calculated normalized step in the nuclear encounter probability (triangles) for 3.5 MeV  $\text{He}^+$  ions for the 45 (a) and 63% sample (b) as a function of the angle  $\psi$  between the [011] crystalline axis of the capping layer and the incoming beam. The guiding lines through the measured (solid line) and simulated data points (dotted line) are used to estimate the angular separation between the appearing maxima  $\psi_{max}$ .

## IV Analytical calculation of angular dependent flux distributions

Feldman and co-workers presented an analytical model which describes the dependence of the steady state flux distribution within a channel on the angle  $\psi$  between the incoming beam and the crystal axis. Steady state means that the flux distribution does not change as a function of depth, which is expected at the depth of the nano-films in the samples

Table II: Calculated values of  $\psi_{Feld}$  for 2 and 3.5 MeV  $\text{He}^+$  ions and these values scaled to the experimentally found values.

	2 MeV		3.5 MeV	
	$\psi_{Feld}$	$\psi_{Feld}/\psi_{max}$	$\psi_{Feld}$	$\psi_{Feld}/\psi_{max}$
45% sample	1.36°	2.47 ± 0.07	1.03°	2.34 ± 0.08
63% sample	1.19°	2.43 ± 0.07	0.90°	2.31 ± 0.09

investigated [12].

Under the assumption that the nano-film does not influence the flux distribution emerging from the capping layer, the strings of the wafer will probe this flux distribution for off-normal axes at a certain distance  $r_{trans}$  from the atom rows of the capping layer. The Feldman model based on the Lindhard's theory states that ions with a certain transverse energy  $E_{\perp}$  are distributed homogeneously within an equipotential contour given by  $U_T = E_{\perp}$ . For each angle  $\psi$ , the distance between the atomic row and the border of the equipotential contour with the highest flux is denoted by  $r_T$ . Accordingly, the flux density reaches its maximum at the string position if  $r_T = r_{trans}$ , and the corresponding angle  $\psi = \psi_{Feld}$  yields the angular separation  $\psi_{max}$  according to the Feldman model. The values of  $\psi_{Feld}$  are given in Table II for both samples, for incoming  $\text{He}^+$  ions at 2 and 3.5 MeV. In columns 3 and 5,  $\psi_{Feld}$  is compared to the experimentally found values of  $\psi_{max}$ , and apparently, a scaling factor is needed.

The angular dependence of the curves of the step height is explained qualitatively with this model, but for a steady state flux distribution these are expected to be symmetric in  $\psi$ . The asymmetry and the structure in-between the maxima can not be explained by the model. A more detailed interpretation of the experiments can only be obtained with Monte Carlo simulations. Consequently, the FLUX7 [13] code has been used to obtain a more detailed comparison with the measurements.

## V Monte Carlo simulations of the angular dependence of the step height

The Monte Carlo (MC) channeling calculations are based on binary collisions of the incoming ion and the target nuclei. In addition, the effect of distant rows of target atoms is accounted for by a continuum string potential. Furthermore, the thermal vibrations of the target atoms and the stopping of the projectile ions by target electrons in the solid are incorporated. The simulations were performed with the well-known universal potential of Ziegler, Biersack, and Littmark incorporated [14]. The program FLUX7 is an improved and extended version of FLUX [13]. One of the output parameters of FLUX7 is the nuclear encounter probability (NEP) with a target atom to cause an event such as large angle scattering (in RBS), a high-energy recoil of the target atom, or a nuclear reaction. The NEP is normalized to that of an equal number of randomly oriented trajectories through an equal distance within the lattice.

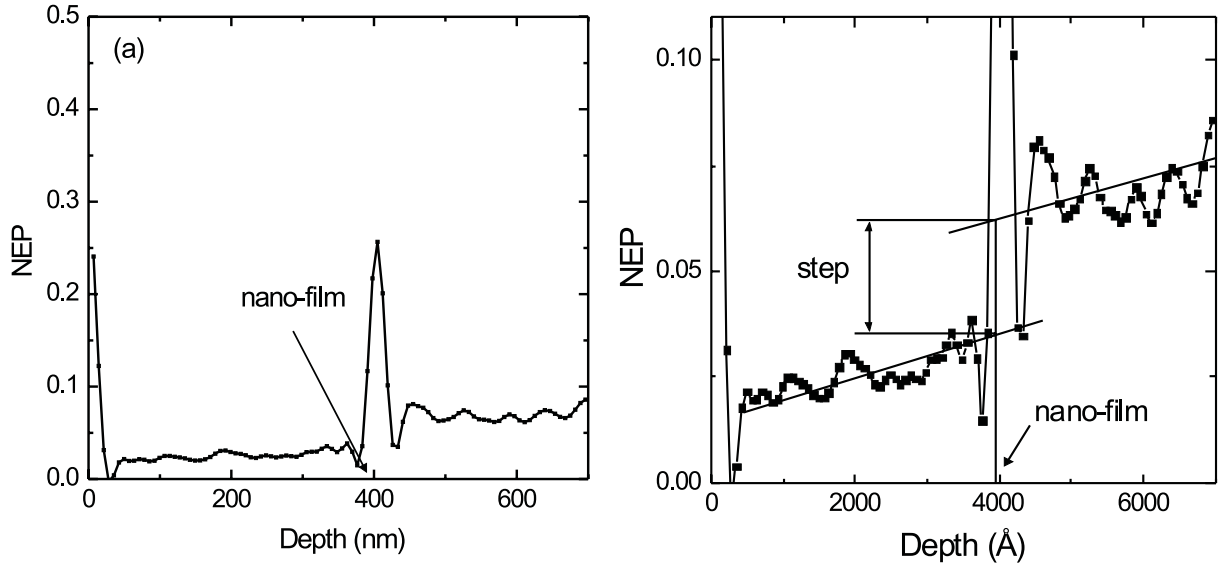


Figure 3.4: NEP (nuclear encounter probability) as a function of depth (a) and a magnification of the step in the NEP (b). The simulation is performed for the 63% sample tilted  $0.21^\circ$  away from the [011] axis using 3.5 MeV  $\text{He}^+$  ions. The total NEP is plotted and, thus, for the nano-film the NEP of Ge is added to the NEP of Si.

The FLUX7 simulation package is used to perform MC calculations of the NEP as a function of depth for the 45 and 63% sample. The strain in the  $\text{Si}_{1-x}\text{Ge}_x$  film leads to a kink in the [011] channel, which can be simulated by rotating the velocity vector of the ions at the beginning and end of the  $\text{Si}_{1-x}\text{Ge}_x$  film. Simulations were done for different translations ( $r_{trans}$ ) of the atomic strings of the substrate. Since in FLUX7 the thickness of a layer can only be varied in discrete steps of one monolayer (ML), a 8 ML thick (2.3 nm)  $\text{Si}_{1-x}\text{Ge}_x$  film is assumed.

In the same way as for the experiments, the step height in the NEP at the depth of the nano-film is determined from the spectra of the NEP as a function of the depth (see Fig. 3.4), and the step height is plotted as a function of the angle  $\psi$  in Fig. 3.3. The angular separation of the two maxima in the yield step height now agrees with the experimentally determined  $\psi_{max}$  for values of  $r_{trans}$  of  $(5.3 \pm 0.5) \times 10^{-2}$  and  $(7.5 \pm 0.6) \times 10^{-2}$  nm for the 45 and 63% sample, respectively. This corresponds to a 8 ML thick nano-film with  $(46 \pm 4)\%$  Ge for the 45% sample and  $(65 \pm 5)\%$  Ge for the 63% sample, resulting in a tetragonal distortion of  $0.034 \pm 0.003$  and  $0.048 \pm 0.004$ , respectively. Note that contrary to the calculations with the Feldman model, no scaling factor is needed to explain the angular separation between the maxima.

The simulations show many detailed similarities with the experimental results: the separations between the appearing maxima in the step height are well within the error margins and the overall trends look very much alike. Furthermore, the angular dependence is not symmetric and this asymmetry agrees very well with that of the measurements. The asymmetry is probably due to the flux distribution not being steady state at the depth of the nano-film. In addition, the Ge concentrations retrieved from the simulations are in good agreement with the values found from the combined RBS and HRTEM

measurements.

Now, with FLUX7, we examine two assumptions which were made before; i.e., the presence of the nano-film is considered as a stacking fault and the nano-film does not influence the flux distribution emerging from the capping layer. To start with the first assumption, FLUX7 allows to simulate a sample consisting of two silicon layers translated with respect to each other without the presence of the  $\text{Si}_{1-x}\text{Ge}_x$  film. Simulations show, that if for such a sample the translation is taken equal to the translation  $r_{trans}$ , which would be caused by the strained  $\text{Si}_{1-x}\text{Ge}_x$  nano-films, the curves of the step height as a function of  $\psi$  are identical for both samples within the statistical error. FLUX7 simulations thus support this assumption.

To investigate the second assumption, i.e., at which thickness will the nano-film start to influence the flux distribution, simulations with combinations of tetragonal distortion and thickness were carried out, resulting in the same  $r_{trans}$ . For layers thicker than  $\approx 6$  nm, the difference between  $\psi_{max}$  of these FLUX7 simulations and that of the experiments is larger than the errors. This suggests that our method can be applied to strained films smaller than 6 nm.

## VI Tetragonal distortion

In the previous section we compared the ion-channeling measurements on the 45 and 63% samples with the FLUX7 simulations. More simulations are performed to relate the measured angular separation  $\psi_{max}$  to  $r_{trans}$  caused by the nano-film, since  $r_{trans}$  is the parameter which is actually determined with the ion-channeling measurements. In these simulations the thickness of the nano-film is kept constant at 2.3 nm, while  $r_{trans}$  is varied. This is done by varying the concentration of Ge in the  $\text{Si}_{1-x}\text{Ge}_x$  nano-film between 30 and 80%, which covers a wide range of physically interesting tetragonal distortions (0.022 to 0.059). To give the results a more universal character,  $\psi_{max}$  has been normalized to  $\psi_1$ , which is  $0.587^\circ$  for this case. Figure 3.5 shows the relation between the normalized  $\psi_{max}$  and the translation  $r_{trans}$ .

The graph in Fig. 3.5 is a universal curve that can be used to retrieve the tetragonal distortion from RBS ion-channeling measurements, when the thickness of the nano-film has been determined with HRTEM. Notice that  $\psi_{max}$  seems to be a linear function of the tetragonal distortion for these combinations of thickness and tetragonal distortion, although the potential in the channel is not a linear function of the distance to the atomic rows [11].

The error in the determination of the tetragonal distortion, resulting from the errors in the measured and the simulated  $\psi_{max}$ , is on average  $\pm 8\%$ . In addition, the error in the HRTEM measurement, which is  $\pm 10\%$  depending on the thickness of the film, must be taken into account.

## VII XRD

The samples have also been investigated with a Bede high resolution XRD (HRXRD) facility at the Eindhoven University of Technology. An asymmetrical  $\theta, 2\theta$ -scan of the  $\{113\}$

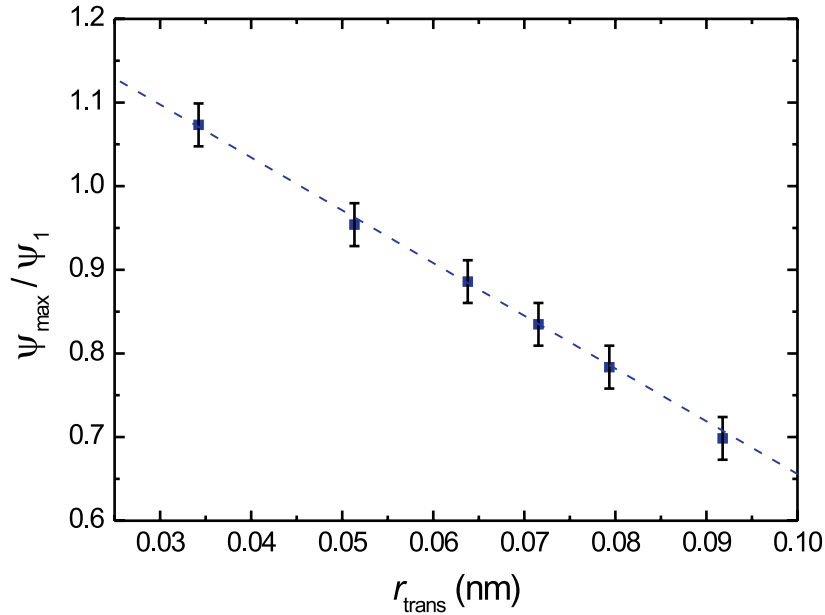


Figure 3.5: Normalized angle  $\psi_{max}/\psi_1$  as a function of the translation  $r_{trans}$ . The points in the graph have been calculated with FLUX7 for 2 MeV  $\text{He}^+$  ions and a silicon sample with a 2.3 nm thick  $\text{Si}_{1-x}\text{Ge}_x$  layer ( $0.3 \leq x \leq 0.8$ ). The line is only to guide the eye.

planes is made with a range of 2000 arcseconds and the grazing incidence configuration is used, since it gives the best results. The resolution is 1 arcsecond and the measuring time per step is 2.5 s. The Bede RADS Mercury package, which is based on dynamical theory simulations, is used to analyze the XRD measurements.

Figure 3.6 shows the results of the measurements and the best fit from the simulations with RADS Mercury for the 45 and the 63% sample. The difference between the two measured curves is very small, but it can be seen that the pattern in the measured curves is translated a little to the left for the 63% sample, which can be expected when a higher compressive strain is present. Note that the parameter measured by XRD is the lattice spacing in the nano-film. For the 45% sample, the best fit through the measured curve is  $(2.8 \pm 0.1)$  nm in thickness and  $(43 \pm 2)\%$  in Ge concentration. For the 63% sample, the best fit parameters are  $(2.7 \pm 0.1)$  nm in thickness and  $(56 \pm 2)\%$  in Ge concentration.

One notices, that the areal Ge density derived from these XRD measurements is  $(5.6 \pm 0.5) \times 10^{15}$  and  $(6.9 \pm 0.5) \times 10^{15}$   $\text{Ge}/\text{cm}^2$  for the 45 and 63% samples, respectively. Since the areal Ge density determined by RBS is considered to be more reliable, we can conclude that the simulation of the XRD measurement on the 45% sample is not satisfactory. Furthermore, in both cases the thickness found in the XRD simulations is much larger than the value determined by HRTEM,  $(2.2 \pm 0.2)$  nm. This, however, might be due to tailing caused by Ge segregation during growth of the Si capping layer. Tailing caused by segregation is a phenomenon that is frequently encountered during growth [15–17]. In the HRXRD simulations tailing can be incorporated by adding an extra layer of  $\text{Si}_{1-x}\text{Ge}_x$  between the nano-film and the capping layer with an exponentially decreasing concentration of Ge atoms.

The graphs of these simulations are not shown, but the best fit parameters and the

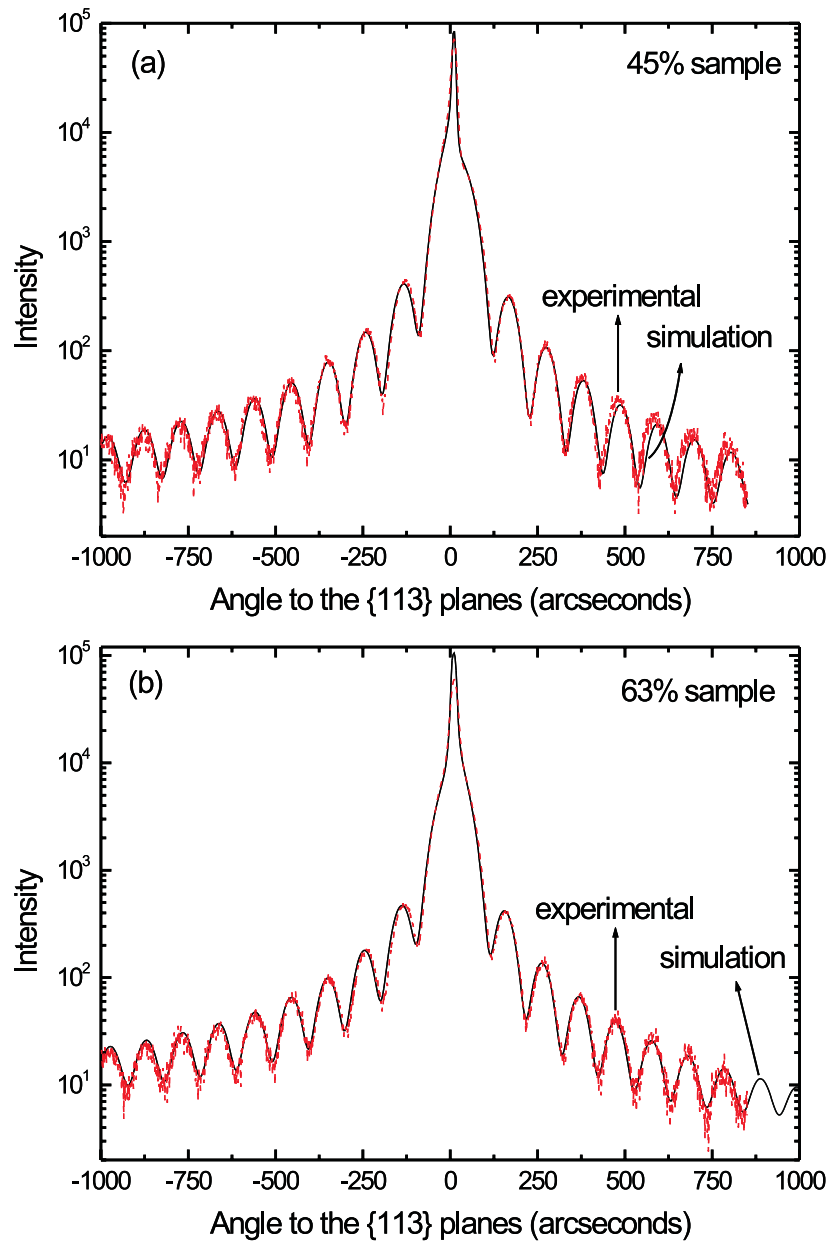


Figure 3.6: Results of the grazing incidence  $\theta, 2\theta$ -scans of the  $\{113\}$  planes of the 45 (a) and 63% sample (b), and the curves of the best fits from the RADS Mercury simulation program.

resulting areal density of Ge and tetragonal distortion in the nano-film are gathered in Table III. The value which is given as the thickness of the layer with the exponentially decaying Ge concentration, is the distance in which the Ge concentration decreases with a factor  $e$ . It is interesting to notice that now for both samples the total Ge areal density is in agreement with the values from the RBS measurements. This implies that HRXRD alone does not provide the correct Ge areal density and the independent measurement of the areal density by RBS is required to obtain an unambiguous interpretation. For the 45% sample the value of the tetragonal distortion found with XRD corresponds to

Table III: Best fit parameters from the RADS mercury simulations with an extra layer added to account for tailing of Ge atoms into the capping layer. Also the resulting areal Ge density and the tetragonal distortion are given.

	thickness nano-film (nm)	Ge concen- tration (%)	thickness tailing layer (nm)	total areal density ( $10^{15}$ Ge/cm $^2$ )	tetragonal distortion
45% sample	$2.2 \pm 0.1$	$44 \pm 2$	$0.8 \pm 0.2$	$5.1 \pm 0.5$	$0.032 \pm 0.002$
63% sample	$2.6 \pm 0.1$	$51 \pm 2$	$0.7 \pm 0.2$	$6.5 \pm 0.4$	$0.038 \pm 0.002$

the value found with ion-channeling, but it doesn't for the measurements on the 63% sample. However, the translation of the strings (which depends on both the tetragonal distortion and thickness), which can be deduced from the XRD measurements on the 63% sample, amounts to  $(6.8 \pm 0.2) \times 10^{-2}$  nm, which again corresponds to the ion-channeling measurements.

Note that the RADS Mercury fitting program provides two ambiguous fits of comparable quality to the measurements on the 63% sample. Apparently, either the RBS areal density or the translation measured with the ion-channeling method outlined in this paper is required as a boundary condition to find an unambiguous interpretation. It is interesting to note that the translation as determined with the ion-channeling method can also be measured for elements in the nano-film with a mass lower than that of the host crystal. It can be concluded that a comprehensive view on the morphology of the nano-film can be obtained by a combination of the RBS channeling method, HRXRD, and HRTEM.

## VIII Conclusions

We have shown that the presence of a strained nano-film in a host crystal leads to a step in the yield of a channeled RBS spectrum for off-normal crystal axes. The height of this step depends on the angle of incidence  $\psi$  of the incoming beam, which influences the flux distribution in the channel. This leads to two maxima in the step height as a function of the angle  $\psi$ .

Measurements on two samples with a  $(2.2 \pm 0.2)$  nm thick buried strained  $\text{Si}_{1-x}\text{Ge}_x$  nano-film in Si show that different Ge concentrations corresponding to different tetragonal distortions, result in different angular separations between the appearing maxima in the yield step height. This can be explained qualitatively with an analytical model from Feldman *et al.*

Furthermore, these experiments can be successfully simulated with Monte Carlo calculations and a universal curve is derived, which relates  $r_{trans}$  with the measured  $\psi_{max}$ . When  $r_{trans}$  is assumed to be determined by a uniform tetragonal distortion and the thickness of the nano-film, and the thickness can be determined with HRTEM, the tetragonal distortion in extremely thin buried films can be measured using MeV ion beams.

The assumption of the uniform tetragonal distortion can be verified with HRXRD. Regarding the areal Ge density determined with RBS as a reliable quantity, HRXRD can

reveal the possible presence of concentration gradients as demonstrated for both samples in this study. It can be concluded that a comprehensive view on the morphology of the nano-film can be obtained by a combination of the RBS ion-channeling method, HRXRD, and HRTEM.

## Acknowledgements

The authors wish to thank Paul Koenraad for his help with the interpretation of the XRD measurements and simulations .

## References

- [a] Author to whom correspondence should be addressed. FAX: +31 40 243 80 60. Present address: Cyclotron Laboratory, Department of Applied Physics, Eindhoven University of Technology, P.O. Box 513, 5600 MB Eindhoven, The Netherlands. Electronic address: L.J.van.IJzendoorn@tue.nl.
- [1] B. D. Cullity, *Elements of X-Ray Diffraction* (Addison-Wesley Publishing Company, Reading, 1976).
- [2] X. S. Wang, Y. J. Zhang, L. Y. Zhang, and X. Yao, *Appl. Phys. A* **68**, 547 (1999).
- [3] S. Yamaguchi, M. Kariya, S. Nitta, T. Takeuchi, C. Wetzel, H. Amano, and I. Akasaki, *J. Appl. Phys.* **85**, 7682 (1999).
- [4] L. Hart, M. R. Fahey, R. C. Newman, and P. F. Fewster, *Appl. Phys. Lett.* **62**, 2218 (1993).
- [5] J. F. van der Veen, *Surf. Sci. Rep.* **5**, 199 (1985).
- [6] J. Vrijmoeth, P. M. Zagwijn, J. W. M. Frenken, and J. F. van der Veen, *Phys. Rev. Lett.* **67**, 1134 (1991).
- [7] T. C. Q. Noakes, P. Bailey, P. K. Hucknall, K. K. Donovan, and M. A. Howson, *Phys. Rev. B* **58**, 4934 (1998).
- [8] H. C. Lu, E. P. Gusev, E. Garfunkel, and T. Gustafsson, *Surf. Sci.* **351**, 111 (1998).
- [9] L. J. M. Selen, F. J. J. Janssen, L. J. van IJzendoorn, M. J. J. Theunissen, P. J. M. Smulders and M. J. A. de Voigt, *Nucl. Instrum. Methods Phys. Res. B* **161-163**, 492 (2000).
- [10] P. W. L. Van Dijk, Ph.D. thesis, Eindhoven University of Technology, 1997.
- [11] L. C. Feldman, J. W. Mayer, and S. T. Picraux, *Materials Analysis by Ion Channeling* (Academic Press, New York, 1982), Chap. 2.
- [12] L. C. Feldman, J. W. Mayer, and S. T. Picraux, *Materials Analysis by Ion Channeling* (Academic Press, New York, 1982), Chap. 3.
- [13] P. J. M. Smulders, and D. O. Boerma, *Nucl. Instrum. Methods Phys. Res. B* **29**, 471 (1987).



- [14] J. F. Ziegler, J. P. Biersack, and U. Littmark, in *The Stopping and Range of Ions in Solids* (Pergamon Press, New York, 1985).
- [15] P. C. Zalm, C. J. Vriezema, D. J. Gravesteijn, G. F. A. van de Walle, and W. B. de Boer, *Surf. Interf. Anal.* **17**, 556 (1991).
- [16] P. C. Zalm, G. F. A. van de Walle, D. J. Gravesteijn, and A. A. van Gorkum, *Appl. Phys. Lett.* **55**, 2520 (1989).
- [17] D. J. Gravesteijn, P. C. Zalm, G. F. A. van de Walle, C. J. Vriezema, A. A. van Gorkum, and L. J. van IJzendoorn, *Thin Solid Films* **183**, 191 (1989).

# 4. Planar ion-channeling on buried nano-films discriminates between ion-atom potentials

L. J. M. Selen, L. J. van IJzendoorn [\*], and M. J. A. de Voigt  
*Research Institutes CPS and COBRA, Cyclotron Laboratory, Department of Applied Physics, Eindhoven University of Technology, P.O. Box 513, 5600 MB Eindhoven, The Netherlands*

P. J. M. Smulders  
*Nuclear Solid State Physics, Materials Science Center, Groningen University, Nijenborgh 4, 9747 AG Groningen, The Netherlands*

Monte Carlo simulations of planar MeV ion-channeling on a very thin buried epi-layer are shown to be extremely sensitive for the ion-atom potential. The presence of the epi-layer leads to enhanced channeling or dechanneling, depending on the angle of incidence of the ion beam. This behaviour is investigated using three different ion-atom potentials, of which the well-known 'universal' potential of Ziegler *et al.* fails to predict the observed behaviour, while only a Hartree-Fock potential is able to satisfactorily reproduce the measurements. The results can be understood with a planar potential model and a phase space model of planar channeling.

When a beam of parallel MeV ions is directed along a set of major lattice planes in a crystal, the ions are steered into regions in between the planes, where the electron density is low. This leads to a reduced nuclear encounter probability, a reduced rate of energy loss, and is called planar channeling [1–3]. The flux distribution of planar channeled ions is strongly depth dependent due to coherent oscillations of the individual ion trajectories. These planar oscillations can be described by a simple phase space model, which correctly predicts catastrophic dechanneling [4, 5] or enhanced channeling [6] in strained layer superlattices, depending on the alternating layer thickness compared to the channeled ion oscillation wavelength  $\lambda$ . The channeled ion flux distribution is also affected by a translation of the lattice planes, as was demonstrated in [7], where MeV protons experienced a blocking to channeling transition when crossing the lattice translation at the fault plane of a stacking fault. The representation in phase space of planar channeled

trajectories is also useful in the interpretation of Monte Carlo simulations, and was used to demonstrate the equivalence of a lattice rotation and a lattice translation [8].

Channeling of MeV ions in single crystals is governed by the ion-atom potential. Most of the attempts which have been made to obtain detailed information on the ion-atom potential involve studies of the wavelength of the transverse flux oscillations and of the breakthrough angles in planar channeling [9–12] and turned out to be rather insensitive to the choice of potential. In 1992 Smulders *et al.* [13] made a detailed study with 1 MeV He ions of the giant focusing peak effect, which occurs in the transition region from [011] axial channeling to {211} planar channeling. They showed that some details of the simulated spectra were sensitive to the assumed ion-atom potential.

This paper presents Monte Carlo simulations of experiments on a Si sample with a buried  $\text{Si}_{0.55}\text{Ge}_{0.45}$  epi-layer, which enable us to discriminate clearly between different ion-atom potentials.

If an epi-layer is coherently grown on a substrate, strain is introduced, and the unit cells in the epi-layer will experience a tetragonal deformation. This leads to a rotation of the lattice planes at the interface between the film and the substrate for off-normal plane directions, which affects planar channeled ions. When a very thin epi-layer of only a few nanometer thickness, which will be called a nano-film in the remainder of this paper, is grown on a substrate, and a layer of the substrate material is grown on top of the nano-film, two opposite rotations of the off-normal lattice planes occur at the beginning and end of the nano-film. Since the nano-film is only a few nanometers thick, the influence of the nano-film on the flux distribution is negligible, and the effect on the channeled ions is the same as for a translation of the host lattice planes at the depth of the nano-film [14]. This means that the buried nano-film can lead to an increase or decrease of the nuclear encounter probability, depending on the depth of the buried nano-film and the angle between the MeV ion beam and the lattice planes.

The sample investigated consists of a Si substrate with a coherently grown 2.2 nm thick  $\text{Si}_{0.55}\text{Ge}_{0.45}$  film, and a 291 nm thick Si capping layer. The rotation angle at the interfaces is  $0.95^\circ$  (which is about 5 times larger than the critical angle for channeling along {011} planes  $\psi_p = 0.19^\circ$ ), and the translation of the planes of the Si substrate relative to those of the Si capping layer is 0.051 nm. The distance between the planes is 0.192 nm.

For the measurement, the sample was placed in a 3-axes goniometer with an angular resolution of  $< 0.005^\circ$  [15]. A 3.5 MeV He ion beam was used, and the scattered particles were detected with a solid state detector with an energy resolution of 40 keV, at a backscattering angle of  $130^\circ$ . The FWHM of the beam divergence was set to  $0.09^\circ$  with two pairs of slits.

For the simulations, the Monte Carlo computer code FLUX [16] was used to calculate the passages of  $2 \times 10^4$  3.5 MeV He ions through the {011} planes, at an angle of  $5^\circ$  away from the [011] axis. For this direction, the distance to the nano-film through the {011} planes of the capping layer is 412 nm. The calculations are based on binary collisions of the incoming particle and the target nuclei. Furthermore, thermal vibrations of the target atoms and the stopping of the projectiles by electrons in the solid are incorporated.

For the analysis with FLUX, three different potentials were used:

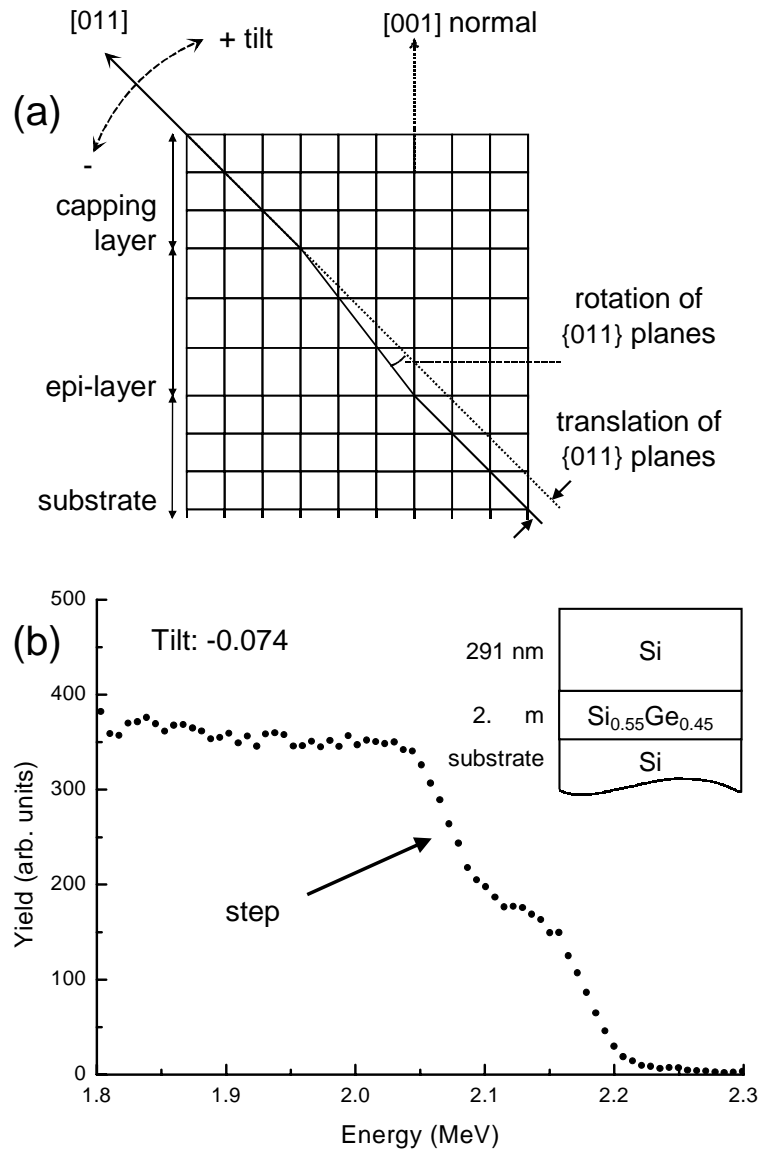


Figure 4.1: Structural schematic of a crystal with a buried strained epi-layer (a), and a measured 3.5 MeV He {011} planar channeled RBS spectrum for a tilt angle of 0.074° (b).

1) The Ziegler-Biersack-Littmark potential, i.e. the universal potential as described in [17].

2) The Molière potential [18], with screening radius  $a = 0.8853a_0(Z_1^{1/2} + Z_2^{1/2})^{-2/3}$ .

3) A Hartree-Fock potential (HF) based on the solid state charge densities, which are tabulated in [17], and assuming a bare He nucleus.

Figure 4.1 shows the composition of the sample with at the interfaces the rotation of the {011} planes (which are the planes through the [011] axis perpendicular to the plane of sight) and the translation of the {011} planes of the Si substrate relative to those of the Si capping layer. Furthermore, a Rutherford backscattering spectrometry (RBS) spectrum resulting from a planar channeling measurement on this sample is shown. The increase in the scattering yield, called 'step' in the remainder of this paper, at the depth

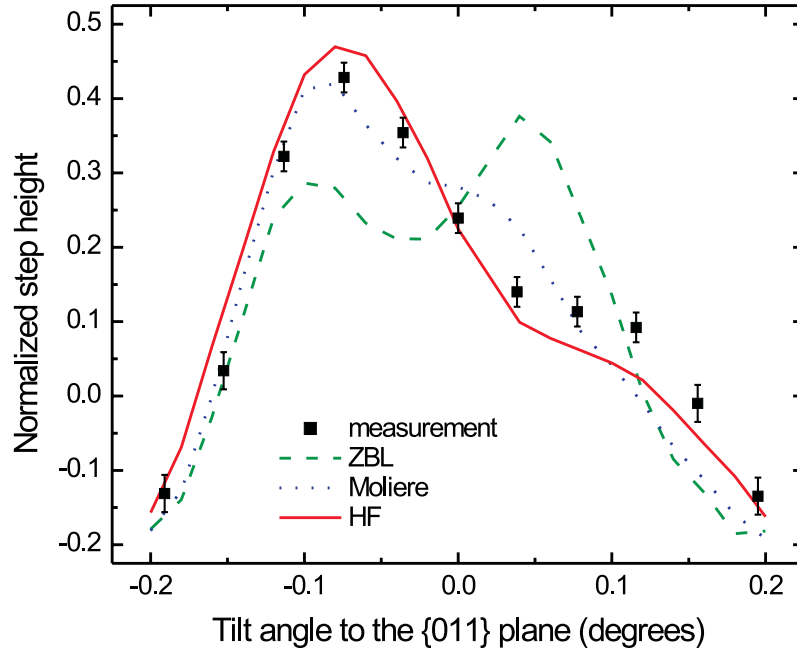


Figure 4.2: Measured (symbols) and simulated normalized step height curves. The dashed line is for the ZBL potential, the dotted line is for the Molière potential, and the solid line is for the HF potential.

of the nano-film is clearly visible in the spectra. The spectrum in Fig. 4.1 is one of the spectra obtained in an angular scan, in which the tilt angle  $\psi$  between the incoming beam and a set of planes is varied.

By varying  $\psi$ , the flux distribution between the planes, and therefore, the step height in the spectrum changes. This results in step height curves as presented in Fig. 4.2. For the measurements (symbols), the step height is taken to be the difference between the average yield in the depth intervals of 500-700 nm and 150-360 nm, i.e. behind and before the nano-film, respectively, which is normalized to the yield for a non-channeling direction.

The step height curves have also been calculated with FLUX and are presented as a solid line (HF potential), a dashed line (ZBL potential), and a dotted line (Molière potential) in Fig. 4.2. The difference between the average normalized nuclear encounter probability in the depth intervals of 482-722 nm and 145-385 nm is taken as the calculated step height.

It is evident that the ZBL potential is not able to correctly reproduce the measured step height curve. A much better fit is obtained for the Molière and HF potential, of which the HF potential reproduces the structure of the measured step height curve best. It seems that the Molière potential leads to a less pronounced step height curve. A figure of merit in the form of a normalized  $\chi^2$  summarizes the quality of agreement obtained for the different potentials. The resulting values are gathered in Table I.

The strong asymmetry in the measured step height curve of Fig. 4.2 can only be achieved, when coherency between the different particle trajectories is preserved at the

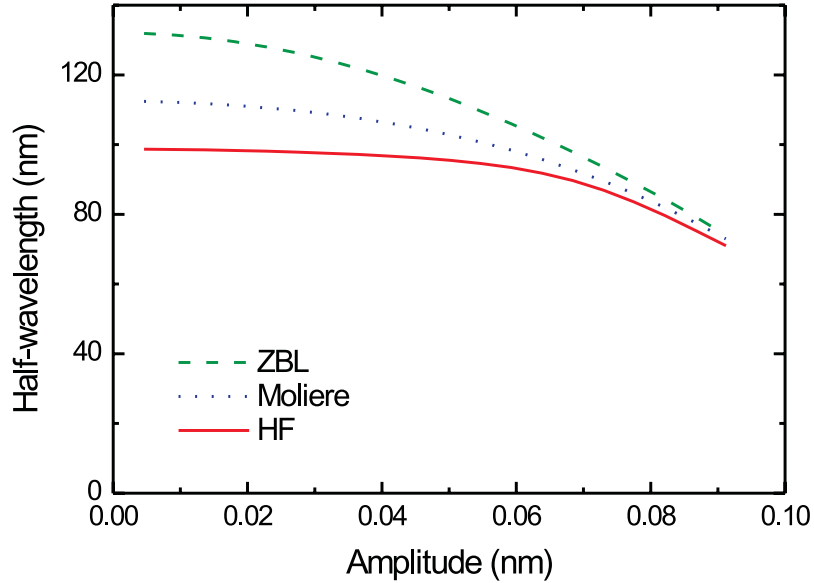


Figure 4.3: Calculated half-wavelength  $\lambda_{1/2}$  of the oscillations of  $\{011\}$  planar channeled He ions versus the oscillation amplitude.

depth of the nano-film. Figure 4.3 depicts the half-wavelength  $\lambda_{1/2}$  of the oscillating trajectory of a channeled ion as a function of the oscillation amplitude, which is determined by the impact parameter and the incident angle of the ion relative to the plane. The half-wavelengths were calculated from the planar potential for He ions between the  $\{011\}$  planes in Si, a static lattice was assumed and thermal vibrations were omitted. The HF potential is the potential which is closest to harmonic, and this is expressed in Fig. 4.3, where the half-wavelengths produced by the HF potential are less amplitude dependent than those produced by the other potentials. Therefore, for the HF potential, the coherency between the He ions with a different oscillation amplitude is better preserved, and apparently, this represents the actual channeling behaviour of the measurements best. Furthermore, the HF potential is the most steep potential of the three, which leads to the shortest half-wavelength for every amplitude. Note that the FLUX simulations do not assume the existence of a planar continuum potential, but are the summarized result of a great number of individual small angle scatters.

To explain the asymmetric step height curve, a phase space model of planar channeling is utilized. The transverse momentum of each He ion in the  $yz$ -plane can be expressed

Table I: Figure of merit (normalized  $\chi^2$ ) for different potentials.

potential	$\chi^2$
ZBL	57
Molière	13
HF	8.2

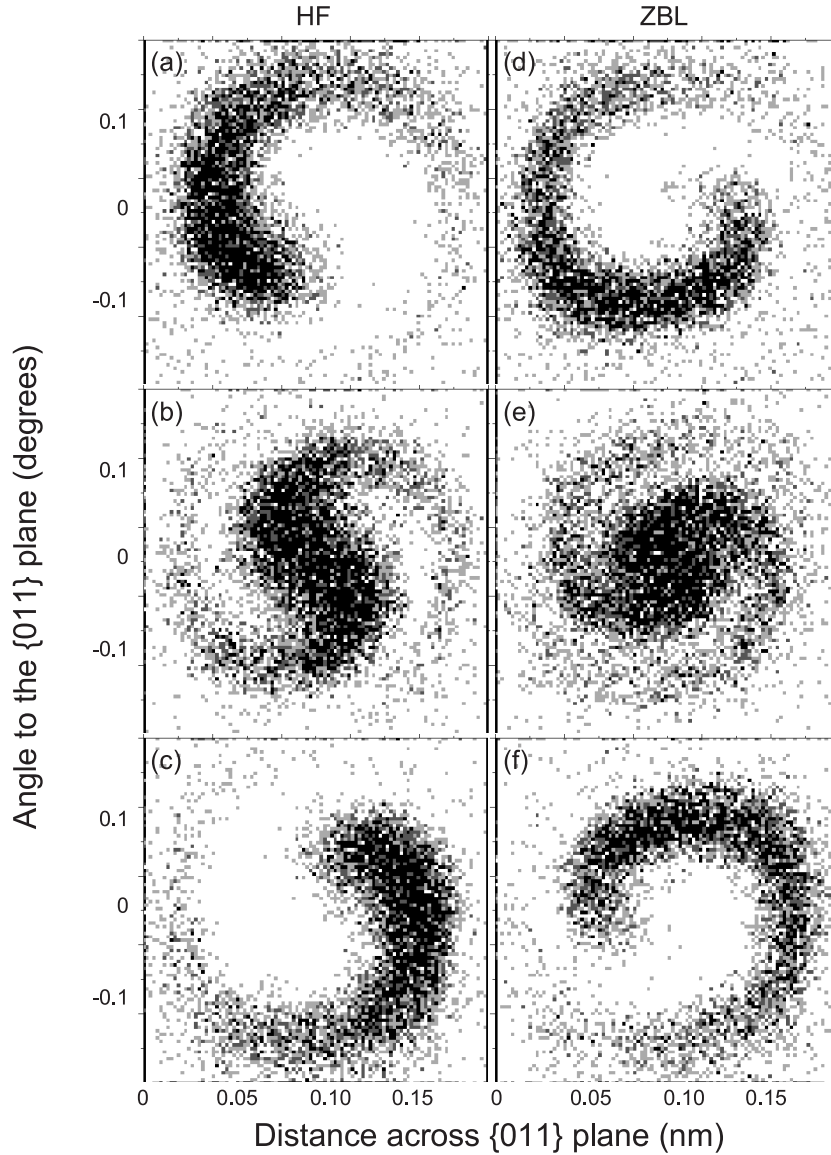


Figure 4.4: A snapshot of the phase space distribution at a depth of 412 nm, of 3.5 MeV He ions in Si, that were incident with a tilt angle of  $-0.1^\circ$  (a) and (d),  $0^\circ$  (b) and (e), and  $0.1^\circ$  (c) and (f), for the HF and ZBL potential, respectively. The ions were originally randomly distributed between two  $\{011\}$  lattice planes (positioned at 0 and 0.192 nm), and only the ions that have stayed in this planar enclosure (roughly 80%) are shown.

as the emergent angle  $\phi$  with the plane at a certain depth  $z$ . In Fig. 4.4 this is plotted versus the position coordinate  $y$  of each ion across the  $\{011\}$  planes for the HF and ZBL potential. The phase space plots presented in Fig. 4.4 are for 3.5 MeV He ions in Si at a depth  $z$  of 412 nm with the beam tilted to  $-0.1^\circ$ ,  $0^\circ$ , and  $0.1^\circ$ , respectively.

Contours of constant transverse energy are closed ellipse-like curves in phase space plots, where it would be exactly an ellipse for a harmonic potential. In case of conservation of transverse energy a particle will follow such a contour in a phase space plot. The channeled part of the beam will fill an elliptical area, which is bounded between the

{011} planes along the horizontal axis, and by the critical angle for channeling along the vertical axis. Not shown here is the initial distribution at the surface, which is confined to a horizontal line across the {011} planes, at a vertical coordinate corresponding to the beam tilt angle. With increasing depth, the center of the phase space distribution rotates within the bounding ellipse, returning to the initial position after one oscillation wavelength. Due to the amplitude dependent wavelength, the distribution deforms, and scattering on electrons leads to a wider distribution.

Due to the presence of the nano-film, the phase space distribution will shift  $-0.051$  nm along the horizontal axis. For the HF potential and a tilt angle of  $-0.1^\circ$  [Fig. 4.4 (a)] a large part of the distribution shifts to a {011} plane, causing a lot of extra dechanneling, which leads to a large step height in a RBS spectrum. For a tilt angle of  $0.1^\circ$  on the other hand [Fig. 4.4 (c)], the distribution shifts to the center between the planes, leading to almost no extra dechanneling, and thus, a relatively small step height. These observations are in good agreement with the shape of the step height curve in Fig. 4.2. Furthermore, we can see that a tilt of  $0.1^\circ$  has about the same effect as a translation of  $0.05$  nm at this depth.

Finally, we will try to understand the difference between the step height curves from calculations with the ZBL and HF potential (see Fig. 4.2). Figure 4.4 also shows phase space distributions for the ZBL potential. Due to the difference in the average half-wavelength, the ZBL flux distribution is about  $90^\circ$  behind in phase compared to the HF distribution at the depth of the nano-film, which leads to a more symmetric dependence on  $\psi$ . Furthermore, the ZBL distribution has a longer tail, which means that it is more spread, which leads to a 'smoothed' step height curve with lower step heights. Thus, the difference between the step height curves from calculations with the ZBL and HF potential is explained qualitatively with the phase space distributions of Fig. 4.4 .

Computer calculations have been proven to be extremely sensitive for simulations of off-normal planar channeling measurements on buried nano-films. The presence of the nano-film causes a translation of the {011} planes of the host crystal, which leads to an increase of the scattering yield in a planar channeled RBS spectrum. Furthermore, the increase in yield depends on the tilt angle between the {011} planes and the incoming beam. The step height curve that is created this way enables us to discriminate between ion-atom potentials. The success of the HF potential for simulations on this system is explained with a planar potential model, which shows that the HF potential is closer to harmonic than the ZBL and Molière potential. Also the shape of the step height curves can be understood using a phase space model of planar channeling, in which the translation of the planes is incorporated as a shift of the channeled phase space distribution.

The agreement of FLUX simulations with the HF potential and planar channeling measurements is quite satisfactory, and establishes the HF potential to be used in MC planar channeling simulations.

## References

- [\*] Author to whom correspondence should be addressed. FAX: +31 40 243 80 60. Present address: Cyclotron Laboratory, Department of Applied Physics, Eindhoven University



of Technology, P.O. Box 513, 5600 MB Eindhoven, The Netherlands. Electronic address: L.J.van.Ijzendoorn@tue.nl.

- [1] J. K. Lindhard, Dan. Vidensk Selsk. Mat. Fys. Medd. **34** (1965).
- [2] *Channeling, Theory, Observation and Applications*, edited by D.V. Morgan (Wiley, London, 1973).
- [3] D. S. Gemmell, Rev. Mod. Phys. **46**, 129 (1974).
- [4] W. K. Chu, J. A. Ellison, S. T. Picraux, R. M. Biefeld, and G. C. Osbourne, Phys. Rev. Lett. **52**, 125 (1984).
- [5] S. T. Picraux, W. R. Allen, R. M. Biefeld, J. A. Ellison, and W. K. Chu, Phys. Rev. Lett. **54**, 2355 (1985).
- [6] W. R. Allen, W. K. Chu, S. T. Picraux, R. M. Biefeld, and J. A. Ellison, Phys. Rev. B **39**, 3954 (1989).
- [7] P. J. C. King, M. B. H. Breese, P. J. M. Smulders, P. R. Wilshaw, and G. W. Grime, Phys. Rev. Lett. **74**, 411 (1995).
- [8] M. B. H. Breese and P. J. M. Smulders, Phys. Rev. Lett. **81**, 5157 (1998).
- [9] J. H. Barrett, Phys. Rev. B **20**, 3535 (1979).
- [10] E. Kührt and F. Täubner, Phys. Status Solidi A **61**, 513 (1980).
- [11] C. D. Moak, J. Gomez del Campo, J. A. Biggerstaff, S. Datz, P. F. Dittner, H. F. Krause, and P. D. Miller, Phys. Rev. B **25**, 4406 (1982).
- [12] B. Schmiedeskamp, P. Jonk, H. E. Roosendaal, and H. O. Lutz, Nucl. Instr. and Meth. B **17**, 309 (1986).
- [13] P. J. M. Smulders, A. Dygo, and D. O. Boerma, Nucl. Instr. and Meth. B **67**, 185 (1992).
- [14] L. J. M. Selen, F. J. J. Janssen, L. J. van IJzendoorn, M. J. J. Theunissen, P. J. M. Smulders, and M. J. A. de Voigt, chapter 3 of this thesis (unpublished).
- [15] P. W. L. Van Dijk, Ph.D. thesis, Eindhoven University of Technology, 1997.
- [16] P. J. M. Smulders and D. O. Boerma, Nucl. Instrum. and Meth. B **29**, 471 (1987).
- [17] J. F. Ziegler, J. P. Biersack, and U. Littmark, in *The Stopping and Range of Ions in Solids* (Pergamon Press, New York, 1985).
- [18] G. Molière, Z. Naturforsch. **2A**, 133 (1947).

# 5. Planar ion-channeling measurements on buried nano-films

L. J. M. Selen, F. J. J. Janssen, L. J. van IJzendoorn [\*], and M. J. A. de Voigt

*Research Institutes CPS and COBRA, Cyclotron Laboratory, Department of Applied Physics, Eindhoven University of Technology, P.O. Box 513, 5600 MB Eindhoven, The Netherlands*

P. J. M. Smulders

*Materials Science Center, University of Groningen, Groningen, The Netherlands*

M. J. J. Theunissen

*Philips Research Laboratories, Eindhoven, The Netherlands*

Planar MeV ion-channeling measurements on 2.2 nm thick  $\text{Si}_{1-x}\text{Ge}_x$  nano-films buried in Si are presented. The presence of the nano-film leads to a step in the yield of the host crystal in a  $\{011\}$  planar channeled RBS spectrum. In previous work we showed that with the help of Monte Carlo simulations the step height in axial channeling measurements provides useful information on the tetragonal distortion in buried nano-films. Since the step height is larger for planar channeling measurements, we extend this method to planar channeling in the present work. The measurements show that the flux distribution of channeled ions is not in statistical equilibrium, but still oscillates at the depth of the buried films (about 280 nm). This is confirmed by simulations performed with the Monte Carlo simulation code FLUX and a qualitative understanding is obtained for the observed phenomena. The accuracy of the calculated step height curves appears much more sensitive to the choice of ion-atom potential than those from axial channeling, which can be attributed to the non-equilibrium distribution of channeled ions between the planes. Consequently, from planar channeling measurements, the tetragonal distortion can be determined with about the same accuracy as from axial channeling measurements in spite of the higher steps.

## I Introduction

At present, single-crystalline layers with a thickness in the nanometer range can be grown accurately by atmospheric pressure chemical vapor deposition (APCVD). Such layers are of growing importance in modern semiconductor technology, where single-crystalline metastable strained films are applied in semiconductor devices such as solid state lasers, heterojunction bipolar transistors and tunnel junctions. Characterization of these strained layers is important, since the lattice deformation in strained films determines the materials and device properties.

MeV ion-channeling is a well-known technique to investigate strain in thin films. The tetragonal distortion is measured by the shift of a so-called angular scan of the strained film with respect to the angular scan of the substrate, along off-normal axes. The thickness of a buried commensurate nano-film is far below the typical thickness required to obtain an angular scan representative of the crystal structure ( $\sim 20$  nm for ion energies  $\sim 2$  MeV). Nevertheless, the value of the strain in a nano-film can be determined with MeV ion-channeling with a method described in Ref. [1]. There we showed that the presence of the nano-film leads to an increase of the scattering yield in an axially channeled Rutherford backscattering spectrum; i.e. a step occurs in the spectrum at the energy corresponding to the depth of the nano-film. The height of this step depends a.o. on the strain in the film and the angle  $\psi$  between the incoming beam and the crystal axes. When the step height is plotted as a function of the angle  $\psi$ , a curve with two maxima is obtained, and with Monte Carlo simulations the angular separation between those maxima can be related to the strain and thickness of the tetragonally deformed film.

Preliminary channeling experiments in  $\{011\}$  planes showed a higher step in planar than in axially channeled spectra. Therefore, planar channeling might be more feasible to determine tetragonal deformation in buried nano-films. In this paper  $\{011\}$  planar channeling measurements and simulations on  $\text{Si}_{1-x}\text{Ge}_x$  nano-films buried in Si are presented and explained using  $\text{He}^+$  ion beams in the energy range of 2 - 3.5 MeV.

## II Experiments

Buried  $\text{Si}_{1-x}\text{Ge}_x$  nano-films in Si have been grown by APCVD on a 6"  $[001]$  oriented Si wafer at Philips Research Laboratories Eindhoven. At first the wafer was cleaned with  $\text{H}_2$  at a temperature of  $1100^\circ\text{C}$ , and then a 5.0 nm Si buffer layer was grown at  $625^\circ\text{C}$ . Subsequently, a 2.2 nm thick  $\text{Si}_{1-x}\text{Ge}_x$  film was grown by deposition of  $\text{GeH}_4$  and  $\text{SiCl}_2$  at  $625^\circ\text{C}$ . Finally, a Si capping layer was deposited at  $700^\circ\text{C}$ . Two different samples were prepared: one sample contains  $(4.6 \pm 0.3) \times 10^{15}$  Ge/cm<sup>2</sup> and the other sample  $(6.4 \pm 0.3) \times 10^{15}$  Ge/cm<sup>2</sup>, as determined by 2 MeV Rutherford backscattering spectrometry (RBS) analysis. With high resolution transmission electron microscopy (HRTEM) the thickness of the  $\text{Si}_{1-x}\text{Ge}_x$  films was measured; for both samples  $2.2 \pm 0.2$  nm was found. The Ge concentration of the samples amounts to 45 and 63%, respectively, and therefore, according to bulk elasticity theory and assuming the absence of dislocations, the tetragonal distortion in the film is  $\varepsilon_T = 0.033$  and  $\varepsilon_T = 0.046$  for the samples containing 45 and 63% Ge, respectively. In the remainder of this paper these samples will be referred to as the

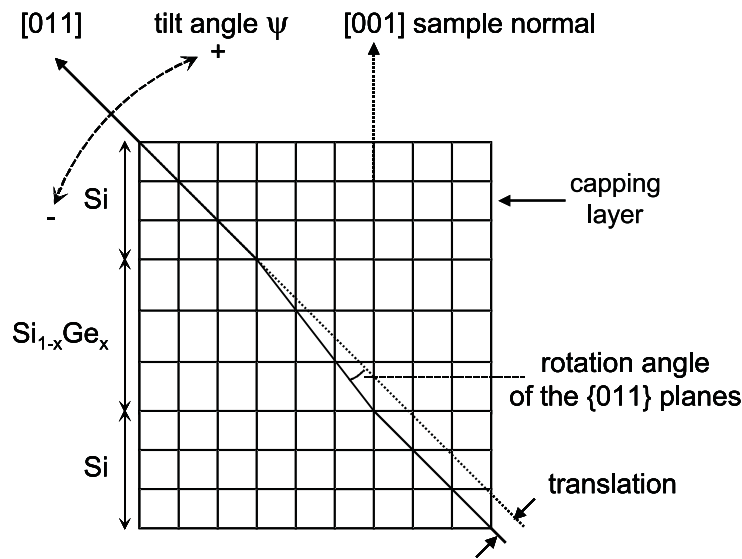


Figure 5.1: Schematic drawing of the investigated samples. The main crystal directions and sample parameters are indicated. The  $\{011\}$  plane is the plane through the  $[011]$  axis perpendicular to the plane of sight. The tilt angle  $\psi$  was varied in the angular scans.

45% and the 63% sample. Furthermore, with XRD measurements the thickness of the capping layer was determined to be  $291 \pm 2$  and  $295 \pm 2$  nm for the 45 and 63% sample, respectively.

Figure 5.1 gives a schematic overview of the samples with the directions of the surface normal ( $[001]$  axis) and the  $[011]$  axis indicated. The  $\{011\}$  plane is the plane through the  $[011]$  axis perpendicular to the plane of sight. Furthermore, the translation of the  $\{011\}$  planes of the substrate, and the rotation angle of the  $\{011\}$  planes of the nano-film relative to those of the capping layer are indicated. The  $\{011\}$  planes in the nano-film are rotated relatively to those of the capping layer with rotation angles of  $0.95^\circ$  and  $1.33^\circ$  for the 45 and 63% sample, respectively. For these values of the thickness and the tetragonal distortion, the translations of the atomic  $\{011\}$  planes of the substrate relative to those of the capping layer are  $0.052$  and  $0.073$  nm for the 45 and 63% sample, respectively. The distance between the  $\{011\}$  planes is  $0.192$  nm.

The ion-channeling experiments have been performed with 2-3.5 MeV  $\text{He}^+$  ion beams from the Philips AVF Cyclotron at the Eindhoven University of Technology, with beam currents varying between 5 and 30 nA. In order to compare the experiments quantitatively, a rotating vane with a gold film was placed in the ion beam. The  $\text{He}^+$  ions scattered from the rotating vane were measured with a  $25 \text{ mm}^2$  Canberra Passivated Implanted Planar Silicon (PIPS) detector with an energy resolution of 15 keV.

For the ion-channeling experiments, the samples were placed in a 3-axes goniometer with an angular resolution  $< 0.005^\circ$  [2]. With two sets of slits the beam divergence was limited to  $0.07^\circ$  FWHM. Backscattered ions were detected with a  $100 \text{ mm}^2$  Canberra PIPS detector positioned at a backscattering angle of  $130^\circ$ . The energy resolution of the detection system is approximately 40 keV. For the planar channeling measurements the beam was tilted  $5^\circ$  to the  $[011]$  axis into the  $\{011\}$  plane and a series of channeling spectra

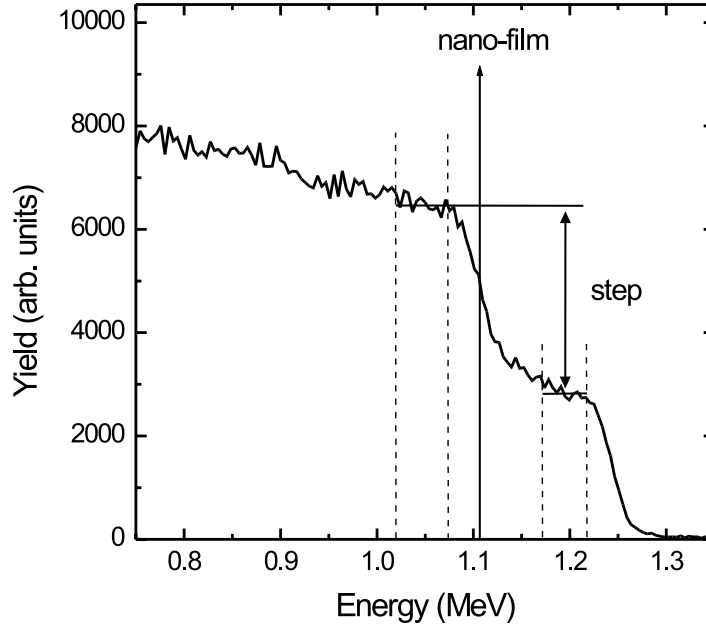


Figure 5.2: Planar channeled RBS spectrum of a measurement corresponding to the 63% sample tilted  $0.02^\circ$  to the  $\{011\}$  plane using 2 MeV  $\text{He}^+$  ions.

was obtained by varying the angle  $\psi$  between the incoming beam and the  $\{011\}$  planes of the sample. The direction of the tilt angle with its sign convention is indicated in Fig. 5.1.

### III Results

Figure 5.2 shows a typical planar channeled RBS spectrum of the 63% sample with a step in the yield at the depth of the strained nano-film, measured at a backscattering angle of  $130^\circ$ . The spectrum is one of the spectra obtained in an angular scan through the  $\{011\}$  plane. The step height is taken to be the difference between the average yield in the energy intervals corresponding to the depth intervals of 350-500 and 105-255 nm, indicated by the dashed lines in Fig. 5.2. The height is normalized to the yield for a non-channeling direction.

The step height in the energy spectrum of a  $\{011\}$  planar channeling experiment resulting from a coherent nano-film is found to be typically 2.5 times larger than the step height in a  $[011]$  axial channeling experiment performed on the same sample [1]. This is due to the distance between the  $\{011\}$  planes, which is half the distance between opposite rows in the  $[011]$  channels (for a zinc-blende type crystal), while the translation of the substrate planes and axes is the same.

The step height in the yield depends on the position of the atomic strings and planes of the substrate, which act as scattering centers in the flux distribution emerging from the capping layer. This flux distribution can be changed by changing the angle  $\psi$  between the incoming beam and the crystal axis or plane, and for *axial* channeling two maxima

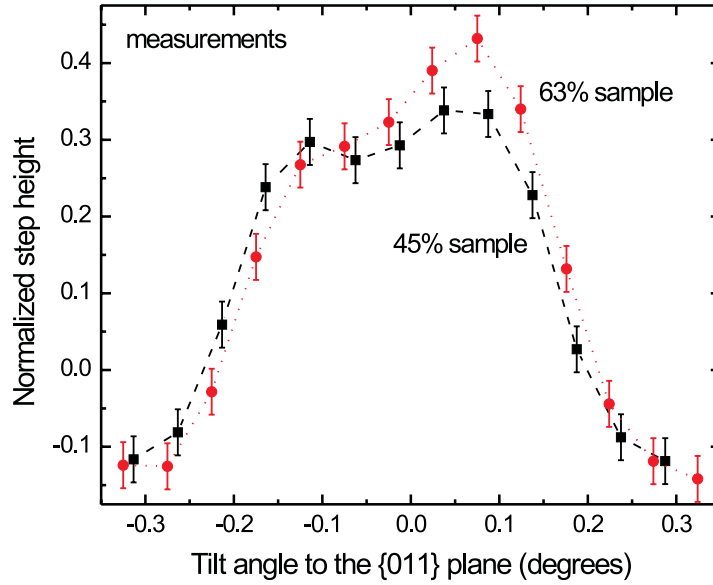


Figure 5.3: Measured step height in the Si yield for 2 MeV  $\text{He}^+$  ions for the 45 and 63% sample as a function of the tilt angle  $\psi$ . The curves are only to guide the eye.

are found in the curve of the step height as a function of the incoming angle  $\psi$  [1]. In Fig. 5.3 the step height in planar channeling spectra is plotted as a function of the angle  $\psi$  for both samples. Two maxima seem to appear for the step height curve of the 45% sample, while for the 63% sample this is clearly not the case.

In *axial* channeling measurements, the angular separation between the appearing maxima scales with the critical angle for channeling,  $\psi_1$ , which in turn scales with the energy of the incoming particles as  $E^{1/2}$  [1]. In Fig. 5.4, *planar* channeling measurements with 2.5, 2.9 and 3.5 MeV  $\text{He}^+$  ions on the 45% sample are presented. In order to compare the step height curves for different energies, the angles  $\psi$  at which the measurements are performed, are scaled to the critical angle for planar channeling,  $\psi_2$ , where  $\psi_2 = \left( \frac{2\pi Z_1 Z_2 e^2 a N d_p}{4\pi \epsilon_0 E} \right)^{1/2}$  with  $Z_1$  and  $Z_2$  the atomic numbers of the incident and target particles respectively,  $a$  the Thomas-Fermi screening distance,  $N$  the number of atoms per unit volume,  $d_p$  the average atomic spacing between planes and  $E$  the kinetic energy of the incident particle [3]. For the case of 2 MeV  $\text{He}^+$  ions, the critical angle for the  $\{011\}$  planes in Si is  $\psi_2 = 0.25^\circ$ . Figure 5.4 shows that the curves are not symmetrical in  $\psi$  and do not always show two maxima. In the next section, a phenomenological flux distribution model is used to explain the observed channeling behaviour.

## IV Angular dependent flux distributions

Feldman and co-workers presented an analytical model which describes qualitatively the dependence of the steady state flux distribution within a *channel* on the angle  $\psi$  between the incoming beam and the crystal axis along which channeling takes place [4]. In this context, steady state means that the flux distribution does not change as a function of

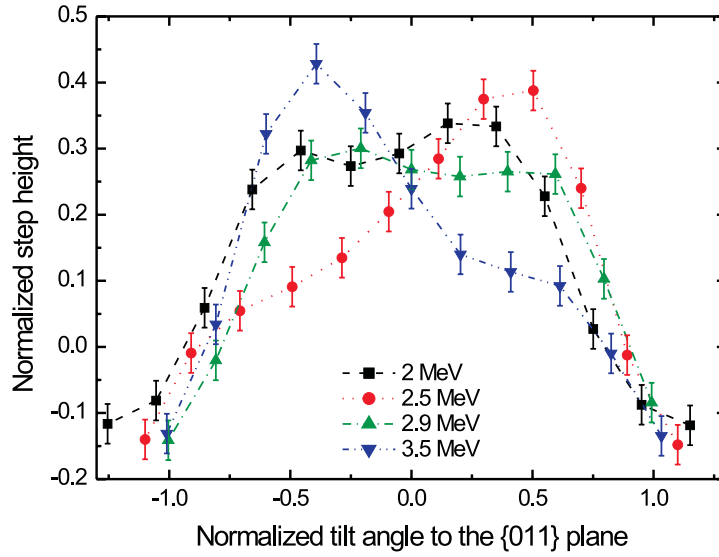


Figure 5.4: Step height curves from the 45% sample for four different energies. The horizontal axis has been scaled with the characteristic angle  $\psi_2$  to compare the different curves.

depth. It was shown that the major part of the channeled ions is distributed over a larger area in the channel if  $\psi$  increases. For *planar* channeling the same principle applies, and thus, by increasing  $\psi$ , the distance across the planes is probed. This implies that the curve of the step height must be symmetric in  $\psi$ , when the flux distribution is steady state at the depth of the nano-film. Figure 5.4 indicates that this is clearly not the case for the measurements with 2.5 MeV and 3.5 MeV  $\text{He}^+$  ions.

The trajectory of a channeled ion in a plane mainly depends on the incoming energy, the entering position (impact parameter to the adjacent plane), the incidence angle with the plane, and the potential of the atomic planes. Assuming a harmonic atomic planar potential, the absence of electronic stopping and thermal vibrations, all channeled particles will describe trajectories with equal wavelengths and a regular pattern of nodes and antinodes will be found [see Fig. 5.5(a)]. For  $|\psi| > 0$ , the nodes of the flux distribution are not expected to be in the centre between the planes, but will change from side to side in between the planes with increasing depth [see Fig. 5.5(b)]. This schematic representation is however of limited significance, since the potential of the atomic planes is not exactly harmonic and, therefore, the wavelength for planar channeling depends on the ion's transverse energy [see Fig. 5.5(c)]. The variation in wavelength is nevertheless small enough to obtain coherency between the individual channeled ion trajectories for several oscillation wavelengths [5].

In our experiments the flux distribution has not reached the steady state phase when the nano-film is reached, and consequently, the scattering yield depends on the thickness of the capping layer and the wavelength of the ion trajectories. If a node in the flux distribution is situated at the depth of the nano-film and at the opposite side of the channel with respect to the translation of the channel, almost no ions will dechannel [Fig. 5.5(d), left]. If the incoming angle is changed from  $\psi$  to  $-\psi$  the node is situated at the same side of the channel as the translation and many ions will dechannel [Fig.

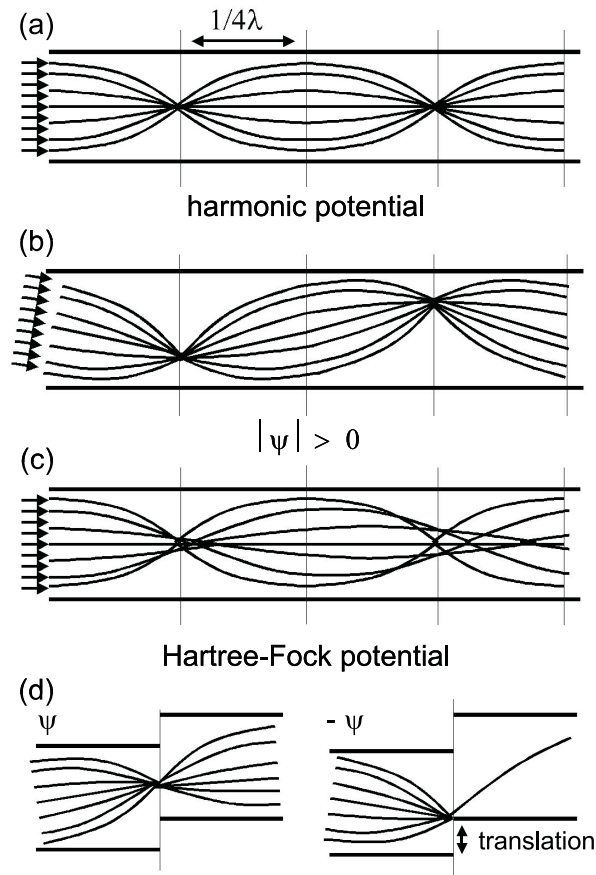


Figure 5.5: Schematic drawing of ion trajectories between two planes for a harmonic potential in the absence of electronic stopping and thermal vibrations (a) and for angles  $|\psi| > 0$  (b), the ion trajectories for a Hartree-Fock potential (c), and a model for the asymmetry of the flux distribution in  $\psi$ , if a node is situated at the depth of the nano-film (d).

5.5(d), right]. Thus, if the nano-film is situated at the same position as a node in the flux distribution, the step height curve will be asymmetric in  $\psi$ . Figure 5.5(b) also shows that due to the absence of focusing, the effect of the translation on the flux distribution will be smaller, when an antinode is situated at the depth of the nano-film. This leads to a more symmetric step height curve in  $\psi$ .

In order to investigate the position of the nodes in the samples under investigation, an estimation of the wavelength averaged over  $10^4$  trajectories is obtained from calculations with the Monte Carlo (MC) channeling simulation program FLUX [6]. The results are summarized in Table I. The number of half-wavelengths that fits in the capping layer of the 45% sample is indicated in the second row of Table I. For  $\{011\}$  planar channeling experiments the distance through the capping layer is 413 nm for the 45% sample. In the simulations a Hartree-Fock potential was used as ion-atom potential (see next section). According to the values in Table I, for each higher energy roughly a quarter of a wavelength less fits in the capping layer. This is confirmed by the shapes of the step height curves in Fig. 5.4, which change from symmetric to asymmetric and vice versa with increasing energy.



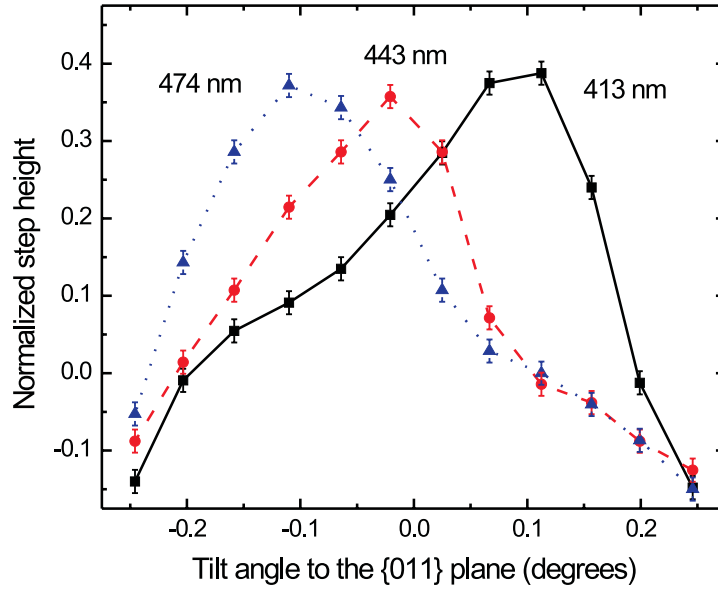


Figure 5.6: Step height curves as a function of the angle relative to the  $\{011\}$  plane for the 45% sample with 2.5 MeV  $\text{He}^+$  ions. The pathlength through the capping layer is enlarged from 413 to 443 and 474 nm.

A pattern of successively nodes and anti-nodes situated at the depth of the nano-film can also be achieved by increasing the length of the paths of the incoming ions through the capping layer. This can be obtained in an experiment by increasing the tilt angle between the ion beam and the  $[011]$  axis while staying in the  $\{011\}$  plane. Experiments with 2.5 MeV  $\text{He}^+$  ions are performed with the ions traveling through 443 nm (0.5 half-wavelength more) and 474 nm (1 half-wavelength more) of the capping layer before the nano-film is reached. In Fig. 5.6 the results of those measurements are shown together with the experiment with the results for 2.5 MeV from Fig. 5.4. For measurements with pathlengths of 413 and 474 nm the maxima of the curves are situated at opposite sides of the  $\{011\}$  plane, which suggests that successive nodes are situated at or very near the nano-film. The curve of the sample with a path through the capping layer of 443 nm is roughly symmetric around  $\psi=0$ , which suggests that an antinode is situated at or near the nano-film in this case.

Although the general scattering behaviour in the experiments is according to the node-

Table I: Estimation of the average wavelength of  $\text{He}^+$  ions for planar channeling in the  $\{011\}$  plane in Si from FLUX7 calculations, and the number of half-wavelengths fitting in the capping layer of the 45% sample.

	2 MeV	2.5 MeV	2.9 MeV	3.5 MeV
half-wavelength (nm)	$60 \pm 2$	$66 \pm 2$	$72 \pm 2$	$80 \pm 2$
no. of half-wavelengths	$6.9 \pm 0.2$	$6.3 \pm 0.2$	$5.7 \pm 0.2$	$5.2 \pm 0.1$

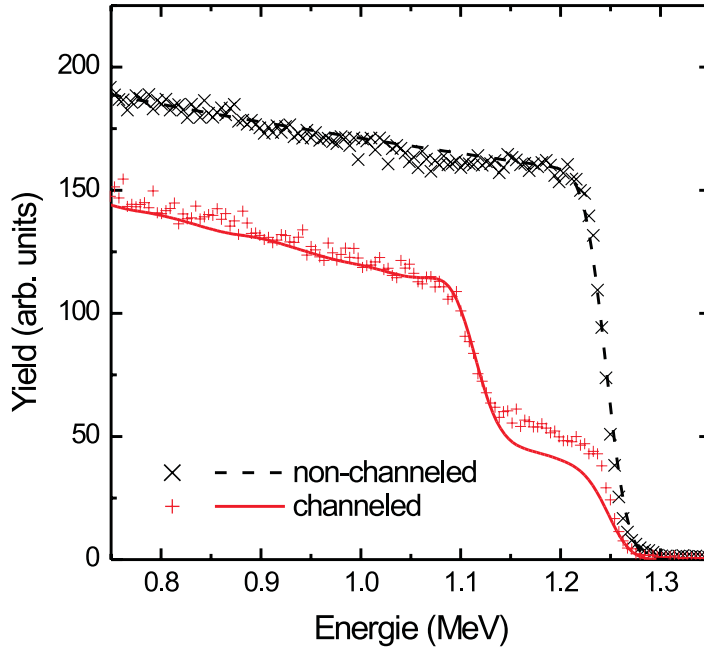


Figure 5.7: Measured (symbols) and calculated (lines) RBS spectra of the 63% sample for a non-channeling direction and for the beam tilted  $0.02^\circ$  to the  $\{011\}$  planes using 2 MeV  $\text{He}^+$  ions.

antinode model, a study with Monte Carlo (MC) simulations is required to find a detailed explanation of the observed step height curves. In the remainder of this paper the FLUX simulation program has been used to evaluate the possibility to retrieve the tetragonal distortion in the buried nano-film from the measured step height curves.

## V Monte Carlo simulations and the ion-atom potential

The Monte Carlo (MC) channeling calculations have been performed using FLUX7, which is an improved and extended version of FLUX [6]. The physical model incorporated in FLUX7 is based on binary collisions of the incoming ion and the target nuclei. One of the output parameters of FLUX7 is the nuclear encounter probability (NEP) with a target atom to cause events like large angle scattering (in RBS), a high-energy recoil of the target atom, or a nuclear reaction. The NEP is normalized by the probability for a random medium with the same density of atoms [6]. The FLUX7 simulation code is used to calculate the NEP as a function of depth for the 45 and 63% samples. The strain in the  $\text{Si}_{1-x}\text{Ge}_x$  film leads to a kink in the  $\{011\}$  plane, which has been simulated by rotating the velocity vector of the ions at the beginning and end of the  $\text{Si}_{1-x}\text{Ge}_x$  film.

The results of the FLUX7 simulations are presented as the NEP as a function of depth, which can be used to generate RBS spectra of scattered ions with the program RBSIM [6]. Figure 5.7 shows the spectrum calculated for 2 MeV  $\text{He}^+$  ions on the 63% sample tilted  $0.02^\circ$  away from the  $\{011\}$  plane and for a non-channeling direction. The same energy

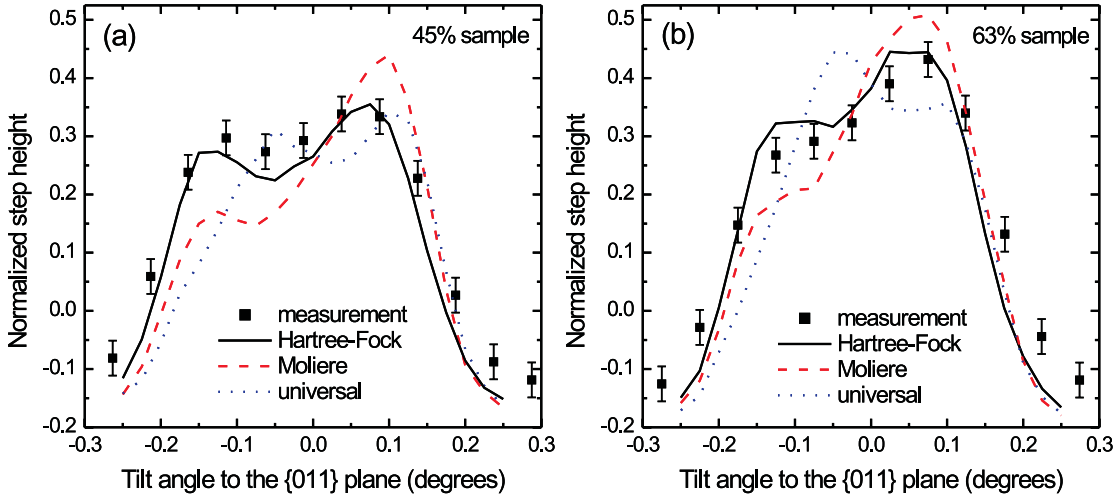


Figure 5.8: Calculated (lines) and measured (symbols) step height curves for the 45 (a) and 63% sample (b), respectively, with 2 MeV He<sup>+</sup> ions. Three ion-atom potentials were used: a Hartree-Fock (solid line), the Molière (dashed line), and the universal potential (dotted line).

resolution is used as in the experiments. For a comparison with the measurement, the spectrum of Fig. 5.2 is added, and for normalization of the measured and calculated spectra the measured spectrum for a non-channeling direction is added.

The step height is derived from the NEP spectrum by subtracting the average yield in a depth interval before the nano-film (103-273 nm) from the average yield in a depth interval behind the nano-film (340-514 nm). The step heights retrieved in this way are plotted as a function of  $\psi$  in Fig. 5.8 together with the outcome of the measurements. Simulations of planar channeling on nano-films are very sensitive to the potential incorporated [7], which can be clearly seen in Fig. 5.8, where simulations with three different ion-atom potentials are shown. These potentials are the well-known universal potential from Ziegler, Biersack, and Littmark [8], the Molière potential [9], and a Hartree-Fock (HF) potential based on the solid state charge densities, which are tabulated in [8], and assuming a bare He nucleus. It is evident from Fig. 5.8 that the HF potential reproduces the measurements best. A figure of merit in the form of a normalized  $\chi^2$  summarizes the quality of agreement obtained for the different potentials. The resulting values for the measurements of Fig. 5.8 and for measurements on the same samples with 3.5 MeV He<sup>+</sup> ions are gathered in Table II.

Table II: Figure of merit (normalized  $\chi^2$ ) for different potentials

potential	$\chi^2$ (45% sample)		$\chi^2$ (63% sample)	
	2 MeV	3.5 MeV	2 MeV	3.5 MeV
universal	41	57	35	60
Molière	30	13	22	14
HF	8.7	8.2	15	8.6

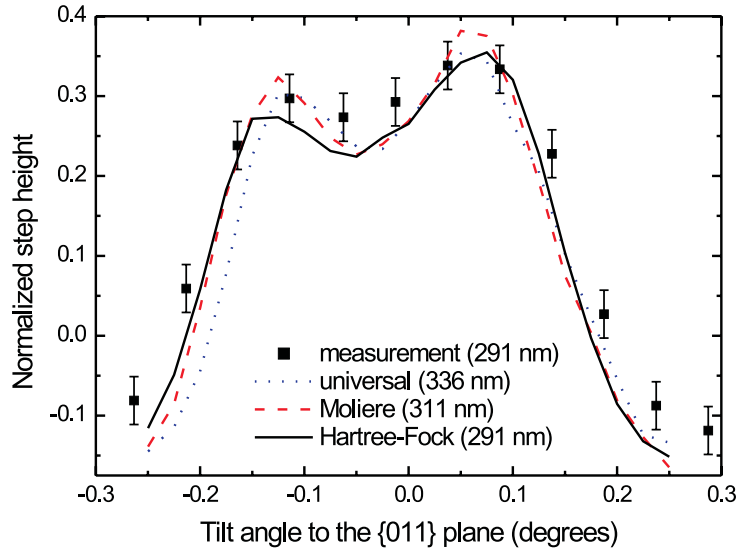


Figure 5.9: Calculated (lines) and measured (symbols) step height curves for the 45% sample with 2 MeV  $\text{He}^+$  ions. For each ion-atom potential a different thickness of the capping layer was used: 291, 311, and 336 nm for the Hartree-Fock (solid line), the Molière (dashed line), and the universal potential (dotted line), respectively.

The difference between these three ion-atom potentials is expressed in the average half-wavelength of the oscillating trajectories of the planar channeled ions, which is shortest for the HF potential and largest for the universal potential [7]. At the depth of the nano-film, the oscillations of channeled ions calculated with the universal and Molière potential are behind in phase relative to those calculated with the HF potential. By increasing the thickness of the capping layer in the simulations with the universal and Molière potential, the phase difference can be counteracted. Simulations were performed, in which the thickness of the capping layer was increased with steps of 5 nm. The step height curves of the simulations that resemble the measurements best are presented in Fig. 5.9. The figures of merit are 8.7, 12, and 17 for the HF, Molière, and universal potential, respectively. The thickness of the capping layer in the simulations shown in Fig. 5.9 with the Molière and universal potential is 311 and 336 nm, respectively. These values do not agree with the value of  $291 \pm 2$  nm found with XRD, and only the simulation with the HF potential resembles the measured structure in the step height curve satisfactorily with this thickness of the capping layer. Therefore, in the remainder of this paper, only simulations with the HF potential are performed to interpret the measured step height curves.

## VI Accuracy of the planar channeling method

The measured step height in planar channeling experiments is higher than in axial channeling measurements, but the accuracy with which the tetragonal distortion can be determined depends on the ability of the MC calculations to reproduce the measured curves. In order to investigate this accuracy, a number of calculations have been carried out in

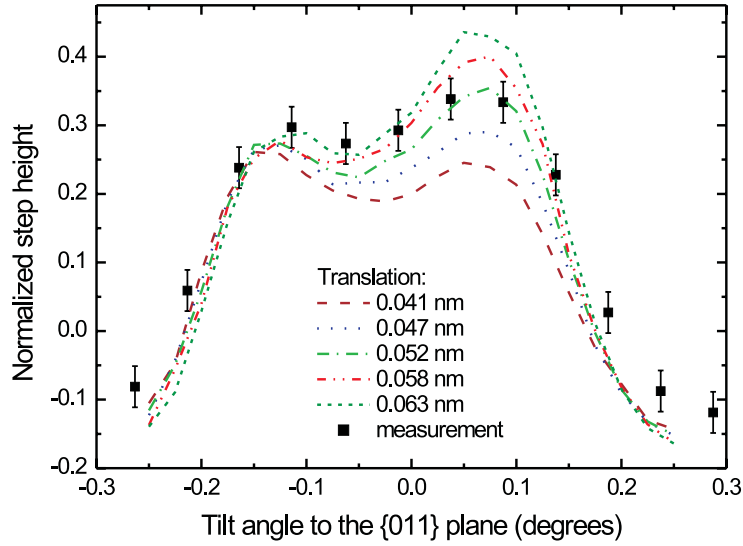


Figure 5.10: Calculated step height curves for the 45% sample with 2 MeV  $\text{He}^+$  ions. The translation of the  $\{011\}$  planes of the substrate is varied from 0.041 to 0.063 nm. The measured step height curve (translation is 0.052 nm) is also indicated (squares).

which the translation has been varied between 0.041 and 0.063 nm in equidistant steps of 0.0055 nm, which corresponds to an increase of the Ge concentration in the nano-film from 35 to 55% in steps of 5%. In Fig. 5.10 the calculated step height curves are shown, for 2 MeV  $\text{He}^+$  ions on Si with a nano-film at a depth of 291 nm. The shape of the curves only changes noticeably on the positive tilt angle side. Apparently, the supposed anti-node is not situated exactly at the depth of the nano-film. Figure 5.10 shows that the translation can be determined with an accuracy of about 10%, which is comparable to the accuracy obtained in *axial* channeling measurements [1]. On balance, the accuracy of the determination of the translation and thus the tetragonal distortion is not improved compared to axial channeling measurements, in spite of the larger step in planar channeling experiments.

Another parameter that has a large impact on the step height curve is the thickness of the capping layer, due to the oscillating flux distribution. Therefore, the thickness of the capping layer has been slightly varied to obtain insight in the sensitivity of the simulations to this parameter. In Fig. 5.11 step height curves are shown for simulations performed on the 45% sample with 2 MeV  $\text{He}^+$  ions. The thickness of the capping layers is 280, 286, 291 and 296 nm, respectively. Figure 5.11 shows that the curves change from almost completely asymmetric to about symmetric in  $\psi$ , when the thickness of the capping layer is increased from 280 to 296 nm. This would correspond to a shift from a node to an antinode situated at the depth of the nano-film. Figure 5.11 shows that the thickness of the capping layer has to be known with an accuracy better than 5 nm. Furthermore, Fig. 5.10 and 5.11 show that some ambiguity exists in the influence of the translation and the thickness of the capping layer on the shape of the step height curve.

Finally, we want to show the results of calculations for different energies. Simulations were performed with 2.5, 2.9 and 3.5 MeV  $\text{He}^+$  ions, respectively, for a capping layer of

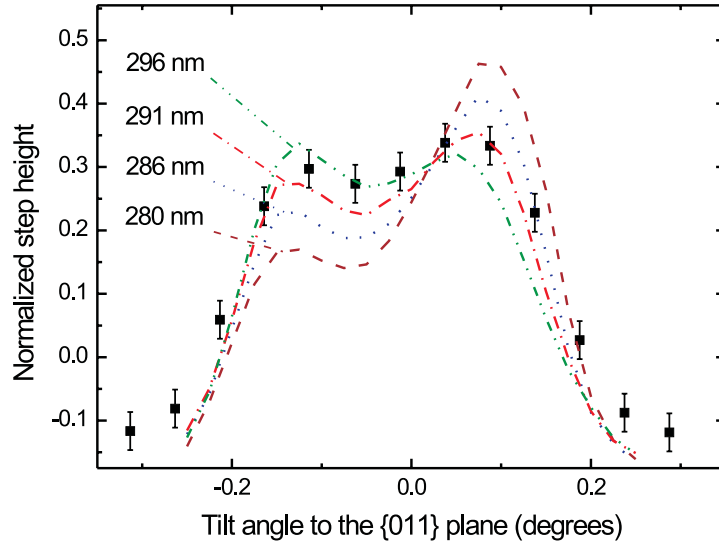


Figure 5.11: Calculated step height curves for the 45% sample with 2 MeV  $\text{He}^+$  ions. The thickness of the capping layer is varied from 280 to 296 nm. The measured step height curve is also indicated (squares).

291 nm and a translation of 0.052 nm, and the results are plotted in Fig. 5.12 together with the measurements. The shapes of the calculated and measured step height curves are very much alike, as was the case for 2 MeV (Fig. 5.8).

## VII Conclusions

Planar channeling measurements on silicon samples with nano-films result in a relatively high step in the energy spectrum compared with axial channeling measurements. The step height depends on the angle between the incoming ion beam and the crystal plane, and also on the energy of the incoming particles, since the ion flux distribution between the crystal planes is not yet steady state when the nano-film is reached.

To be able to extract the tetragonal distortion in an arbitrary nano-film from planar channeling measurements, the step height curves must be simulated with FLUX7. The accuracy of the calculated step height curves appears much more sensitive to the choice of ion-atom potential than those from axial channeling, which can be attributed to the non-equilibrium distribution of channeled ions between the planes. Consequently, from planar channeling measurements, the tetragonal distortion can be determined with about the same accuracy as from axial channeling measurements in spite of the higher steps.

Furthermore, for planar channeling measurements the shape of the step height curves not only depends on the structure of the nano-film, but also on the exact position of the buried nano-film relative to the oscillating flux distribution. It is shown that the thickness of the capping layer has to be known with an accuracy better than 5 nm to obtain the correct value for the tetragonal distortion in the nano-film.

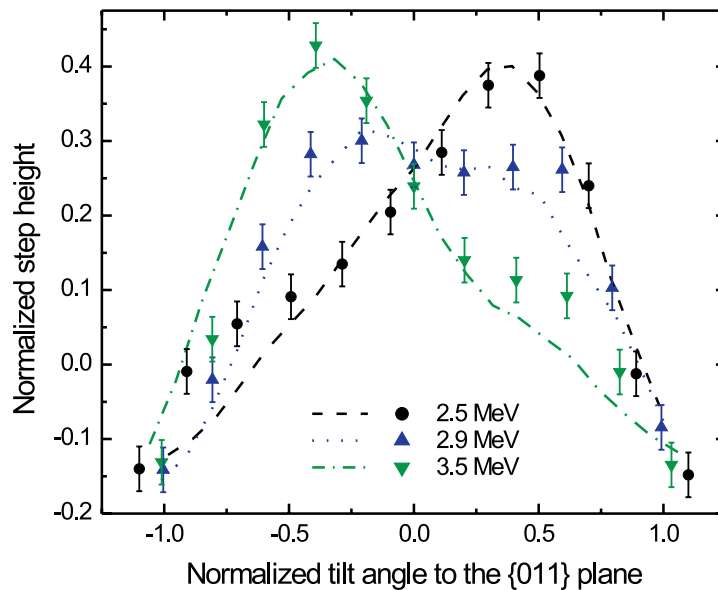


Figure 5.12: Calculated (lines) and measured (symbols) normalized step height curves for 2.5, 2.9, and 3.5 MeV  $\text{He}^+$  ions on the 45% sample. The tilt angle is normalized to the characteristic angle for planar channeling  $\psi_2$ .

## References

- [\*] Author to whom correspondence should be addressed. FAX: +31 40 243 80 60. Present address: Cyclotron Laboratory, Department of Applied Physics, Eindhoven University of Technology, P.O. Box 513, 5600 MB Eindhoven, The Netherlands. Electronic address: L.J.van.IJzendoorn@tue.nl.
- [1] L. J. M. Selen, F. J. J. Janssen, L. J. van IJzendoorn, M. J. J. Theunissen, P. J. M. Smulders, and M. J. A. de Voigt, chapter 3 of this thesis (unpublished).
  - [2] P. W. L. Van Dijk, Ph.D. thesis, Eindhoven University of Technology, 1997.
  - [3] L. C. Feldman, J. W. Mayer, and S. T. Picraux, *Materials Analysis by Ion Channeling* (Academic Press, New York, 1982), Chap. 2.
  - [4] L. C. Feldman, J. W. Mayer, and S. T. Picraux, *Materials Analysis by Ion Channeling* (Academic Press, New York, 1982), Chap. 3.
  - [5] J. A. Ellison, S. T. Picraux, W. R. Allen, and W. K. Chu, *Phys. Rev. B* **37**, 7290 (1988).
  - [6] P. J. M. Smulders, and D. O. Boerma, *Nucl. Instrum. and Meth. B* **29**, 471 (1987).
  - [7] L. J. M. Selen, P. J. M. Smulders, L. J. van IJzendoorn, and M. J. A. de Voigt, chapter 4 of this thesis (unpublished).
  - [8] J. F. Ziegler, J. P. Biersack, and U. Littmark, in *The Stopping and Range of Ions in Solids* (Pergamon Press, New York, 1985).
  - [9] G. Molière, *Z. Naturforsch.* **2A**, 133 (1947).

# 6. Lattice deformation in InAs/GaAs superlattices characterized by MeV ion-channeling

L. J. M. Selen, L. J. van IJzendoorn [\*], F. J. J. Janssen, and M. J. A. de  
Voigt

*Research Institutes CPS and COBRA, Cyclotron Laboratory, Department of Applied  
Physics, Eindhoven University of Technology, P.O. Box 513, 5600 MB Eindhoven, The  
Netherlands*

P. J. M. Smulders

*Materials Science Center, University of Groningen, Groningen, The Netherlands*

Axial and planar MeV ion-channeling experiments are performed on a InAs/GaAs superlattice with ten coherent buried InAs nano-films in GaAs. The presence of the nano-films leads to a step in the channeled RBS spectrum, and the step height depends on the incidence angle of the ions. In combination with Monte Carlo simulations, the average tetragonal distortion in the nano-films can be determined from axial channeling measurements, although the separate contributions of each individual nano-film can not be resolved in the measured spectra. Planar channeling measurements show a higher step, but a detailed resemblance between measurements and simulations of the higher step can not be achieved. The planar channeling simulations appear to be rather insensitive to the choice of ion-atom potential.

## I Introduction

In modern semiconductor technology, the application of buried single-crystalline metastable strained films with a thickness in the nanometer range is increasing. Examples are semi-conductor devices such as solid state lasers, heterojunction bipolar transistors and tunnel junctions. Characterization of these strained layers is important, since the lattice deformation in strained films determines the materials and device properties.

The presence of such a strained nano-film leads to a step in the yield of the host crystal in a channeled RBS spectrum. In previous work we showed that the step height as a function of incident beam direction combined with Monte Carlo simulations, provides useful information on the tetragonal distortion in the buried nano-film [1, 2].



In this work we extend this method to more complex samples. For that purpose we performed [011] axial and {011} planar channeling measurements on an InAs/GaAs superlattice structure of ten buried InAs nano-films in GaAs. In the past Picraux *et al.* used planar channeling to investigate strain in superlattices under conditions of catastrophic dechanneling [3, 4]. Their method is extremely sensitive to the relative strain between the superlattice layers, but is limited to superlattices with layers of equal thickness. The method presented in this paper does not have that limitation.

## II Experimental

The InAs/GaAs samples were grown in a Varian GenII molecular beam epitaxy system at Eindhoven University of Technology. First a 675 nm thick GaAs buffer layer is grown on a [001] oriented GaAs substrate. On top of this a 0.36 nm thick InAs layer, i.e. 1.1 monolayer (ML) InAs, and a 18.08 nm thick GaAs barrier layer were grown pseudomorphically, both at 410°C [5]. This combination of an InAs and GaAs layer is repeated 8 times, subsequently another InAs layer of 0.36 nm is grown. This superlattice structure is capped with 97.9 nm GaAs at 650°C, a 30.0 nm thick  $\text{Al}_{0.33}\text{Ga}_{0.67}\text{As}$  layer, and a 17.0 nm thick GaAs layer, both grown at 700°C.

The tetragonal distortion is a quantity for the strain defined as  $\varepsilon_T = \varepsilon_{\perp} - \varepsilon_{\parallel} = (a_{\perp} - a_{\parallel})/a_V$ , where  $a_{\perp}$  is the perpendicular lattice constant,  $a_{\parallel}$  the in-plane lattice constant, and  $a_V$  the Vegard crystal lattice constant, which according to Vegard's law is a linear combination of the lattice constants of the components weighted with their concentration. The in-plane strain  $\varepsilon_{\parallel}$  and the perpendicular strain  $\varepsilon_{\perp}$  are defined as the relative deviations of the lattice constants from the Vegard crystal lattice constant. Assuming the absence of dislocations, the tetragonal distortion in each InAs film is  $\varepsilon_T = 0.14$ . For a thickness of 1.1 ML, this leads to a translation of 0.033 nm of the GaAs  $\langle 011 \rangle$  strings and {011} planes traversing each InAs layer (see Fig. 6.1). The rotation angle at the interfaces is  $3.98^\circ$ , which is about eight times larger than the critical angle for channeling in our experiments (typically  $0.5^\circ$ ).

Figure 6.1 shows a schematic drawing of the sample. The incoming ion beam is aligned with the [011] axis of the capping layer for axial channeling experiments. For planar channeling experiments, the beam is tilted  $5^\circ$  away from the [011] axis into the {011} plane, which is the plane through the [011] axis perpendicular to the plane of sight in Fig. 6.1. To obtain an angular scan, the ion beam is tilted along the angle  $\psi$  between the ion beam and the [011] axes or {011} planes as indicated in Fig. 6.1. Every incorporated InAs layer is in fact a tetragonally deformed nano-film, which is expected to induce an increase of the scattering yield in a channeled spectrum for off-normal axes or planes [1, 2].

Ion-channeling experiments have been performed with 2-6 MeV  $\text{He}^+$  ion beams from the 2-30 MeV Philips AVF Cyclotron at Eindhoven University of Technology. In order to compare the scattering yield in the experiments quantitatively, a rotating vane with a 88 nm thick gold film is placed in the ion beam. The yield of  $\text{He}^+$  ions scattered from the gold film is measured with a 25 mm<sup>2</sup> Canberra Passivated Implanted Planar Silicon (PIPS) detector with a total energy resolution of 20 keV.

The samples were placed in a 3-axes goniometer with an angular resolution  $< 0.005^\circ$  [6].

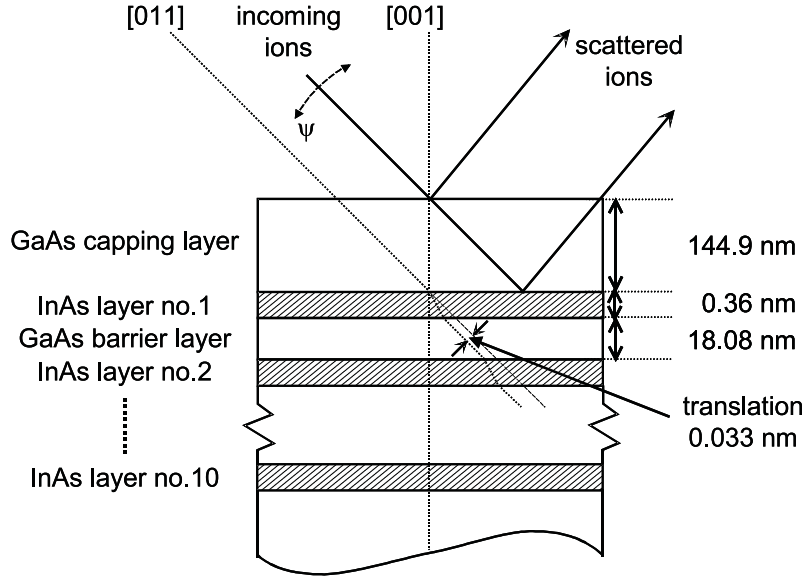


Figure 6.1: Schematic drawing of the sample. The directions of the  $[001]$  surface normal, the  $[011]$  axis, the incoming ion beam, and the tilt angle of the ion beam are indicated.

With two sets of slits the beam divergence was limited to  $0.07^\circ$  FWHM. Backscattered ions were detected with a  $100 \text{ mm}^2$  Canberra PIPS detector also with a total energy resolution of approximately 20 keV, positioned at a backscattering angle of  $130^\circ$ . Axial scans through the  $[011]$  axis were obtained by varying the angle  $\psi$  between the incoming beam and the  $[011]$  axis of the sample in the  $\{001\}$  plane (see Fig. 6.1). For the planar channeling measurements the beam was tilted  $5^\circ$  away from the  $[011]$  axis into the  $\{011\}$  plane, and a series of channeling spectra was obtained by varying the angle  $\psi$  between the incoming beam and the  $\{011\}$  planes of the sample. The  $\{011\}$  plane is the plane through the  $[011]$  axis perpendicular to the plane of sight in Fig. 6.1.

A study with Monte Carlo (MC) simulations is required to relate the observed step height curves to the tetragonal distortion in the InAs layers. For that purpose the MC channeling simulation program FLUX7 is used, which is an improved and extended version of FLUX [7]. The calculations are based on binary collisions of the incoming ion and the target nuclei. In addition, the effect of distant rows of target atoms is accounted for by a continuum string potential. Furthermore, the thermal vibrations of the target atoms and the stopping of the projectiles by electrons in the solid are incorporated. In contrast to axial channeling, simulations of planar channeling on buried nano-films have been proven to be very sensitive to the ion-atom potential [8]. Only a Hartree-Fock potential provided satisfactory results, but at this moment FLUX7 can combine a Hartree-Fock potential only with a lattice structure containing one type of atom. Therefore, the well-known universal potential of Ziegler, Biersack, and Littmark is used in this work [9]. It should also be noted that FLUX7 can handle only two different types of atoms in one layer, which poses problems with the capping layer which contains  $\text{Al}_{0.33}\text{Ga}_{0.67}\text{As}$ . However, the difference in lattice constant between  $\text{Al}_{0.33}\text{Ga}_{0.67}\text{As}$  and GaAs is only 0.3%, which leads to a negligible tetragonal distortion of only 0.001 and a kink angle of  $0.03^\circ$  at the GaAs/ $\text{Al}_{0.33}\text{Ga}_{0.67}\text{As}$  interfaces along the  $[011]$  axes and  $\{011\}$  planes in the capping layer. Since this kink

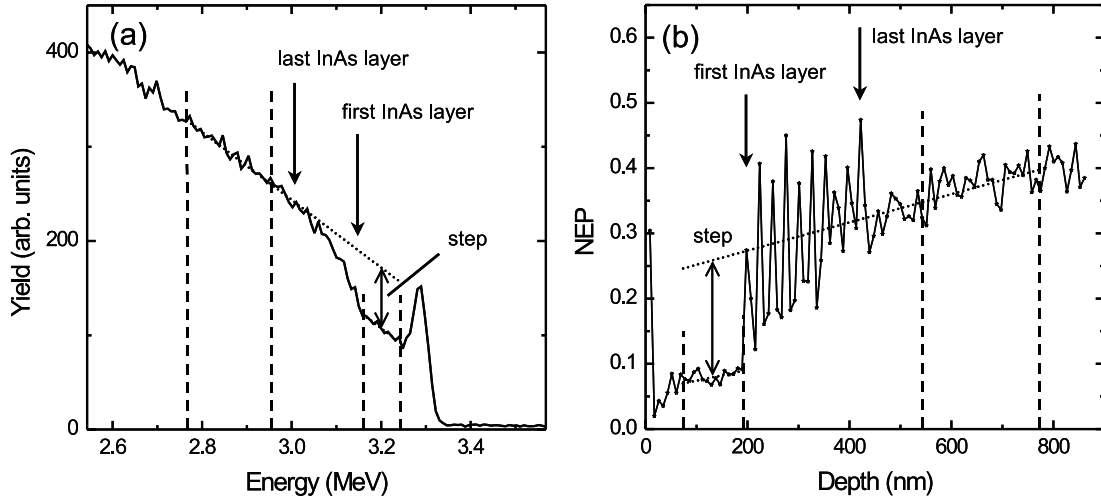


Figure 6.2: Measured RBS spectrum (a) and calculated NEP spectrum (b) of a measurement corresponding to the sample tilted  $0.20^\circ$  to the  $[011]$  axis using  $3.5 \text{ MeV He}^+$  ions.

angle is only small compared to the critical angles for channeling of  $6 \text{ MeV He}^+$  ions in the  $[011]$  axes ( $0.50^\circ$ ) and  $\{011\}$  planes of GaAs ( $0.19^\circ$ ), and the kink angle at the GaAs/InAs interfaces ( $3.98^\circ$ ), the influences on the channeling experiments are assumed negligible. Therefore, the  $\text{Al}_{0.33}\text{Ga}_{0.67}\text{As}$  in the capping layer is substituted by GaAs in the simulations. The strain in each InAs layer leads to a kink of  $3.98^\circ$  in the  $[011]$  axes and  $\{011\}$  planes at the GaAs/InAs interfaces, which can be simulated by rotating the velocity vector of the ions at the beginning and end of each InAs layer.

One of the output parameters of FLUX7 is the nuclear encounter probability (NEP) with a target atom to cause an event such as large angle scattering (in RBS), a high-energy recoil of the target atom, or a nuclear reaction. The NEP is normalized by the probability for a random medium with the same density of atoms [7]. The FLUX7 simulation code is used to perform MC calculations of the NEP as a function of the depth for the InAs/GaAs sample.

### III Axial channeling measurements

Figure 6.2 (a) shows a typical axially channeled RBS spectrum of the InAs/GaAs sample with a step in the yield in the depth-interval of the superlattice, measured with the detector at a forward scattering angle of  $65^\circ$ . The spectrum is one of the spectra obtained in an angular scan through the  $[011]$  axis. The spectrum shown in Fig. 6.2 (a) corresponds to the sample tilted  $0.20^\circ$  away from the  $[011]$  axis in the  $\{001\}$  plane. The energy of the ions scattered at the first and last InAs layer are indicated. In the spectrum the total step height corresponds to the summed effect of contributions from the 10 separate InAs layers. The step height is taken to be the difference between the average yield in the depth intervals of 380-550 and 60-140 nm [indicated by the dashed lines in Fig. 6.2 (a)], i.e. behind and before the superlattice structure, respectively. To correct for the angular dependent dechanneling rate, the average yield in the interval behind the superlattice

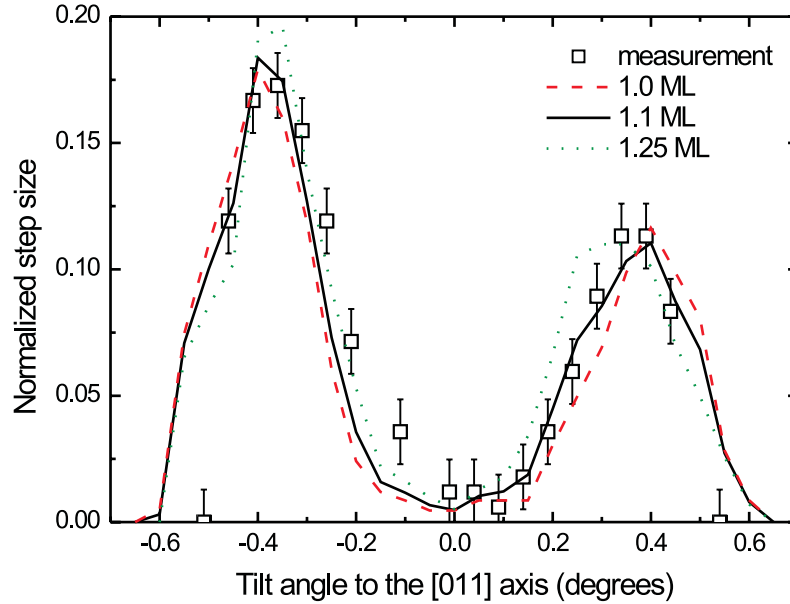


Figure 6.3: Measured (squares) and calculated (lines) [011] axial step height curves for 3.5 MeV  $\text{He}^+$  ions. Calculations were done assuming InAs layers with a thickness of 1.0 (dashed line), 1.1 (solid line), and 1.25 ML (dotted line).

structure is linearly extrapolated to the interval before the superlattice structure, and the slope of the extrapolation corresponds to the increase in dechanneling [see Fig. 6.2 (a)].

Since the difference between the kinematic factors of the interaction of  $\text{He}^+$  ions with Ga and As is small for the configuration used, the difference in the measured energy between  $\text{He}^+$  ions that interacted with Ga and As is only 15 keV. With the detector resolution of 20 keV, only one surface peak can be distinguished in the energy spectrum. Since the stopping power of channeled 3.5 MeV  $\text{He}^+$  ions in GaAs is approximately 1.0 keV/nm [9], the depth resolution for this measurement configuration is about 20 nm. Due to this depth resolution, energy straggling effects, and the small difference in the kinematic factors of Ga and As, the individual step heights in the spectra resulting from each InAs layer cannot be distinguished in Fig. 6.2 (a). Therefore, the tetragonal distortion of the individual layers was not measured separately, and the obtained characteristics involve the summed effect of all InAs layers.

In Fig. 6.2 (b) a plot of the NEP as a function of the depth is shown for a FLUX7 simulation of the InAs/GaAs sample with a beam of 3.5 MeV  $\text{He}^+$  ions tilted  $0.20^\circ$  away from the [011] axis in the {001} plane. The lattice mismatch between the InAs and GaAs layers is assumed to be fully accommodated by an elastic distortion of the InAs layer, and the depth steps in the calculations are chosen small enough to distinguish the increase in scattering yield resulting from the 10 individual InAs layers in the NEP spectrum. The extrapolated difference between the average NEP in the depth intervals of 84-200 and 545-782 nm is taken as the calculated step height [see Fig. 6.2 (b)]. These intervals correspond to depths of 59-141 and 385-553 nm, respectively, for the [001] oriented sample.

The step height in the yield depends on the angle  $\psi$  between the crystal axis and the ion beam. In Fig. 6.3 the step height from the experiments and calculations is plotted

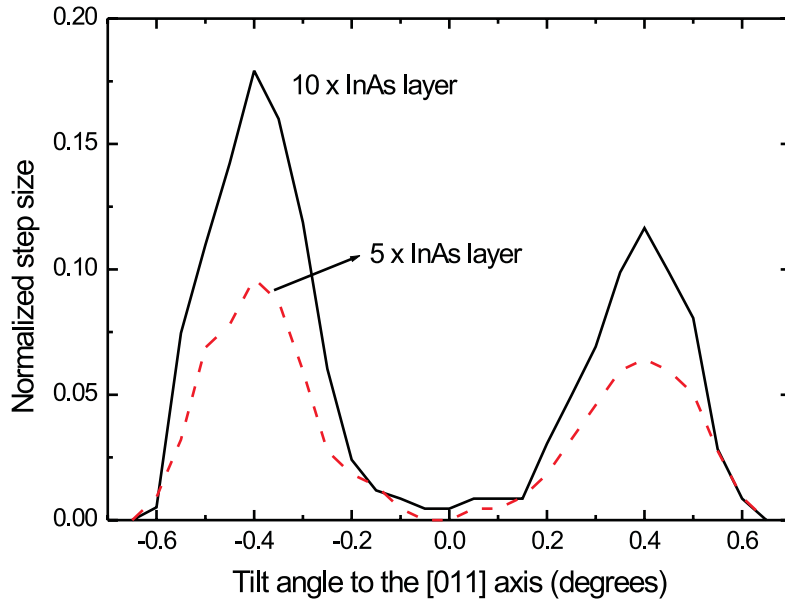


Figure 6.4: Calculated [011] axial step height curves for samples with 10 (solid line) and 5 (dashed line) InAs layers, respectively.

as a function of the angle  $\psi$  for 3.5 MeV  $\text{He}^+$  ions. The step heights in Fig. 6.3 are normalized to the yield for a non-channeling direction. Note that this method does not directly determine the tetragonal distortion, but measures the translation of the [011] axes across the strained nano-film. When the thickness of the nano-film is known, the tetragonal distortion can be retrieved from the translation of the [011] axes. Simulations were performed with three different translations of the atomic [011] strings corresponding to fully deformed InAs layers with a thickness of 1.0, 1.1, and 1.25 ML. The simulations with a translation corresponding to 1.1 ML thick InAs layers shows the best resemblance with the measurements. Two maxima appear in the step height curves, which is also observed in case of a single  $\text{Si}_{1-x}\text{Ge}_x$  nano-film [1]. Furthermore, in Fig. 6.3 the step height in between the maxima almost goes to zero, which is not the case in the measured step height curves on a single  $\text{Si}_{1-x}\text{Ge}_x$  nano-film [1]. The reason is probably that the width of angular scans in Si are smaller due to the smaller nuclear charge of Si. For a single nano-film the step height depends on the interaction of the channeled flux with the translated atom strings of the layer behind the nano-film. With a steady state flux distribution, the channeled flux does not change with depth, and when  $\psi$  is increased, the contour containing the highest flux of channeled particles covers an increasing part of the channel area. The observed step height in a channeled RBS spectrum will be highest for the angle  $\psi$ , at which the border of that highest flux contour is just positioned at the position of the translated atom strings. The translation of the atom strings is related with the tetragonal distortion in the nano-film, and the angular separation between the maxima can be related to the distortion in the nano-film in combination with MC calculations [1].

Since for measurements on a single buried nano-film the angular distance between the maxima in the step height curve depends on the translation of the [011] strings of the substrate, it is important to investigate whether the angular dependence of the step height

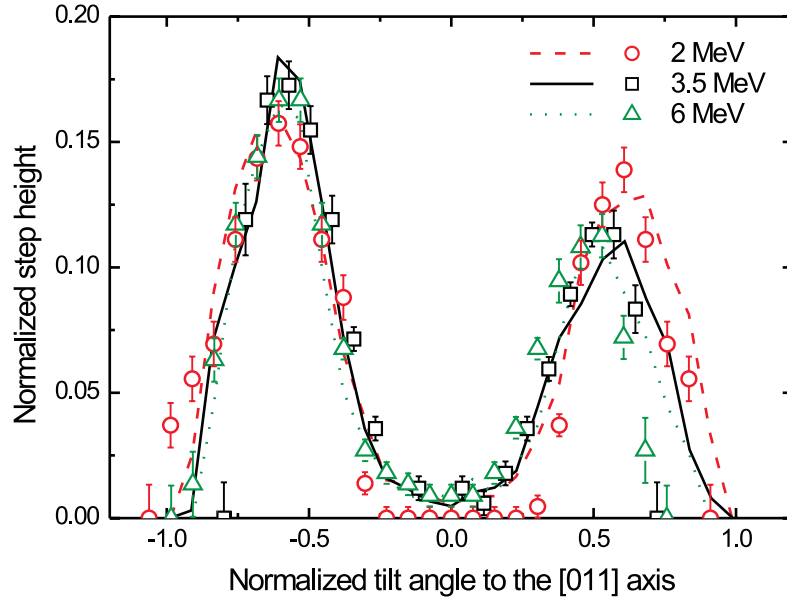


Figure 6.5: Measured (symbols) and calculated (lines) [011] axial step height curves for 2, 3.5, and 6 MeV  $\text{He}^+$  ions.

curves of Fig. 6.3 is determined by the separate contributions due to the translation at each InAs layer, or by a collective effect of the total superlattice structure. Therefore, simulations are performed on an equivalent InAs/GaAs sample containing 5 InAs layers instead of 10, and the results are depicted in Fig. 6.4. Clearly, the angular dependence of the step height curve is the same for both samples, and furthermore, the step height curve for the sample with 5 InAs layers is generally half the height of the curve for the sample with 10 InAs films. This shows that the angular dependence of the step height curve is determined by the separate contributions from the individual InAs films. When the step height due to the presence of a single strained nano-film in a sample is too small to determine a step height curve, a superlattice structure with multiple equal nano-films can be grown from which the tetragonal distortion can still be determined for the separate nano-films.

Note that in Fig. 6.3 and 6.4 the height of the two maxima is not equal, which suggests that a steady state flux distribution is not reached, when the channeled ions reach the superlattice structure. Channeled ions start with oscillating trajectories within a channel, and the coherency between the trajectories of different ions disappears typically within 100-200 nm due to energy straggling and interaction with target electrons [10]. The capping layer of our sample is 145 nm thick. To investigate if the flux distribution is steady state at the superlattice, experiments and simulations have been performed with 2 and 6 MeV  $\text{He}^+$  ions, since the oscillation wavelength of the ion trajectories depends on the energy of the incoming ions. To compare the step height curves for different energies, the tilt angles are scaled with the critical angles for channeling, which for the [011] axis of GaAs are  $0.87^\circ$ ,  $0.66^\circ$  and  $0.50^\circ$  with 2, 3.5, and 6 MeV  $\text{He}^+$  ions, respectively. The results are presented in Fig. 6.5, which shows that the step height curves for negative tilt angles are the same within the experimental error. For positive tilt angles, the maximum in the

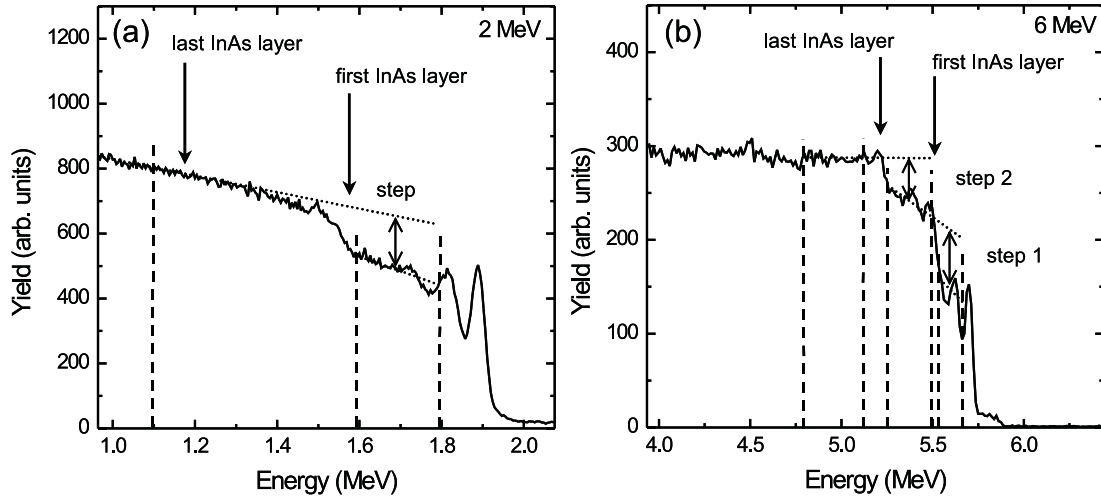


Figure 6.6: Measured planar channeled RBS spectra for 2 MeV  $\text{He}^+$  ions with the sample tilted  $0.10^\circ$  to the  $\{011\}$  plane (a) and 6 MeV  $\text{He}^+$  ions with the sample tilted  $-0.02^\circ$  to the  $\{011\}$  plane (b).

step height curves changes for different energies, which means that the flux distribution is not steady state at the superlattice.

Figure 6.3 shows calculations for InAs layers with a thickness of 1.0, 1.1, and 1.25 ML, which corresponds to a translation of the  $[011]$  strings of 0.030, 0.033, and 0.037 nm, respectively. The sensitivity of the angular separation of the step height curves to the translation of the atom strings can be seen, and the translation due to the InAs layers can be determined with an accuracy almost twice as good as that for experiments and simulations on a single nano-film, which is about 0.006 nm [1]. Furthermore, the thickness of the InAs layers found with this method agrees with the thickness of  $1.1 \pm 0.1$  ML, which was determined with high resolution X-ray diffraction (see section II). This implies that the InAs layers are deformed in accordance with elasticity theory to accommodate the difference in lattice constants of GaAs and InAs.

## IV Planar channeling measurements

The sensitivity for measuring tetragonal deformation in nano-films depends on the magnitude of the translation of the channeling axes or planes across the nano-film [1,2]. Planar channeling experiments show a more pronounced step in the channeled RBS spectrum, due to the relatively small distance between the  $\{011\}$  planes compared to the distance between opposite rows in the  $[011]$  channels, which is 0.200 and 0.400 nm, respectively, for a zinc-blende type crystal.

In a previous paper [2] it was shown that for planar channeling, oscillations in the flux distribution are still present at a depth corresponding to the depth of the buried InAs films. Consequently, the interpretation of the measurements is complicated and MC simulations are required to explain the step height curves. The wavelength of the oscillations in the flux distribution is energy dependent, and for a sample with a *single*

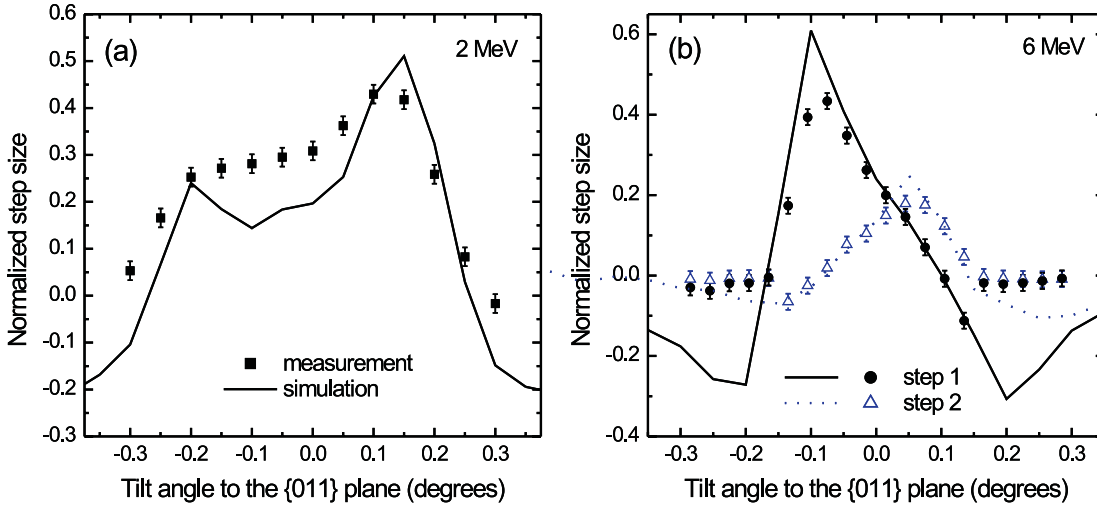


Figure 6.7: Measured (symbols) and calculated (lines) {011} planar step height curves for 2 (a) and 6 MeV He<sup>+</sup> ions (b).

nano-film this leads to symmetric or asymmetric step height curves, depending on whether a node or an anti-node of the oscillating flux distribution is situated at the nano-film, respectively [8]. Planar channeling step height curves are measured on the InAs/GaAs sample to investigate the energy dependence for a sample with multiple nano-films.

Figure 6.6 shows two measured planar channeled spectra of the InAs/GaAs sample with a step in the yield at the depth of the superlattice structure. The spectrum in Fig. 6.6 (a) is measured with He<sup>+</sup> ions of 2 MeV and the detector at a forward scattering angle of 55°. In this spectrum the total step height is clearly not equally distributed over the 10 separate InAs layers. The spectrum in Fig. 6.6 (b) corresponds to a measurement with 6 MeV He<sup>+</sup> ions also at a scattering angle of 55°. It is remarkable that the spectrum measured at 6 MeV contains two steps, approximately at the energy of the first and last InAs film in the sample. The same effect is observed in the calculated NEP spectrum for 6 MeV He<sup>+</sup> ions at the same tilt angle. Note that a double step is not observed in the measurements with 2 MeV He<sup>+</sup> ions. The double step for 6 MeV He<sup>+</sup> ions might be specific for the combination of the wavelength of the oscillating trajectories of the channeled ions for 6 MeV and the thickness of the GaAs barrier layers. In order to check this hypothesis, simulations were performed on a sample with 10 InAs layers with GaAs barrier layers of 15 and 22, instead of 18.08 nm. In some of the NEP spectra calculated for the sample with 15 nm thick barrier layers, also 2 steps can be distinguished but the effect is less pronounced than for the sample investigated. Furthermore, in none of the NEP spectra calculated for the sample with 22 nm thick barrier layers 2 steps can be distinguished. The effect of 2 steps in the spectrum thus indeed seems to be specific for the combination of thickness of the barrier layers and the wavelength of the oscillating trajectories for 6 MeV He<sup>+</sup> ions in GaAs.

The measured and calculated step height curves of the single step with 2 MeV and the two separate steps with 6 MeV are plotted in Fig. 6.7. For both the measurements and the simulations, the steps are determined from the difference in the extrapolated average



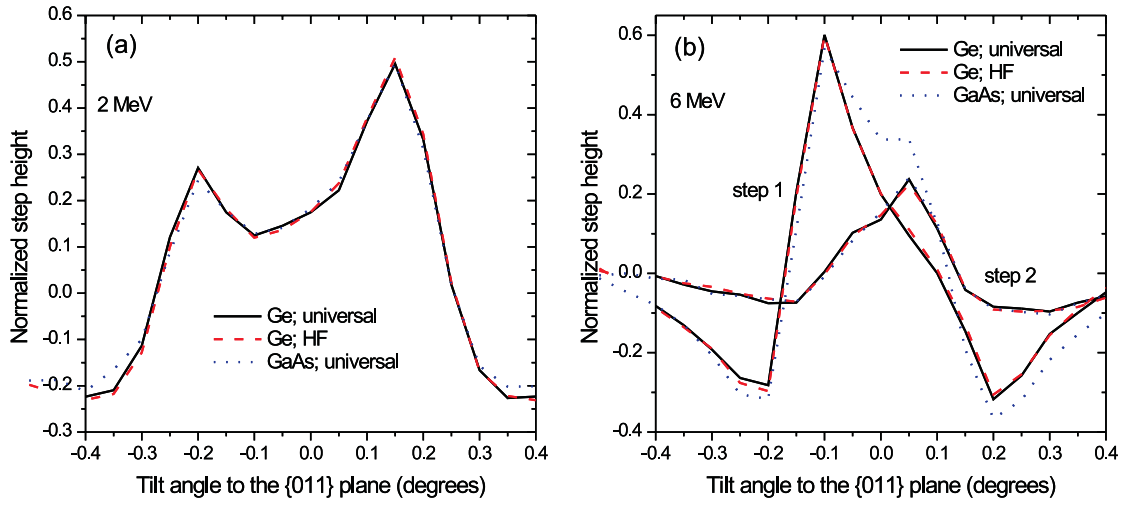


Figure 6.8: Calculated  $\{011\}$  planar step height curves for the HF and the universal potential with a Ge instead of a GaAs lattice for 2 (a) and 6 MeV  $\text{He}^+$  ions (b). The calculations of Fig. 6.7 are also added.

yield in the depth intervals of 380-550 and 60-140 nm for 2 MeV, and 380-550, 210-310, and 60-140 nm for 6 MeV (see Fig. 6.6). For 6 MeV the general shape of the simulated step height curves is in good agreement with the measurements, except for the negative step heights, which do not appear for the measurements. For 2 MeV the agreement is worse.

For a single  $\text{Si}_{1-x}\text{Ge}_x$  nano-film it has been demonstrated that simulations of planar channeling measurements on single nano-films are very sensitive to the ion-atom potential [8]. We will try to determine the influence of the choice of ion-atom potential on the calculations on the sample investigated in this paper. At this moment FLUX7 is not able to combine a 2-atomic lattice structure with the Hartree-Fock potential. In order to estimate the influence of the ion-atom potential anyway, an artificial sample is defined with exactly the same structure, but each Ga, As, and In atom is replaced by a Ge atom, which is the next neighbor of both Ga and As in the periodic system. First, the planar step height curves at 2 and 6 MeV have been calculated with the artificial sample with Ge, with the universal potential incorporated. The results are shown in Fig. 6.8 together with the calculations on the original InAs/GaAs sample (from Fig. 6.7), which are also carried out with the universal potential. Only for the simulations with 6 MeV  $\text{He}^+$  ions some deviation is observed for the step height curve of the first step, but the replacement of Ga, As, and In with Ge does not result in significantly different step height curves. Next, the planar step height curves for the artificial sample with Ge have been calculated with the Hartree-Fock potential, and the results are also shown in Fig. 6.8. The difference between the step height curves of the artificial Ge sample calculated with the universal and the Hartree-Fock potential is negligible small. Apparently, the ion-atom potential is almost insensitive for simulations of planar channeling on the sample under investigation. This is confirmed by calculations on the half-wavelength as a function of the amplitude, from the planar potential for  $\text{He}^+$  ions between the  $\{011\}$  planes of Ga and As. These calculations show that the difference in half-wavelength from the Hartree-Fock and universal potential

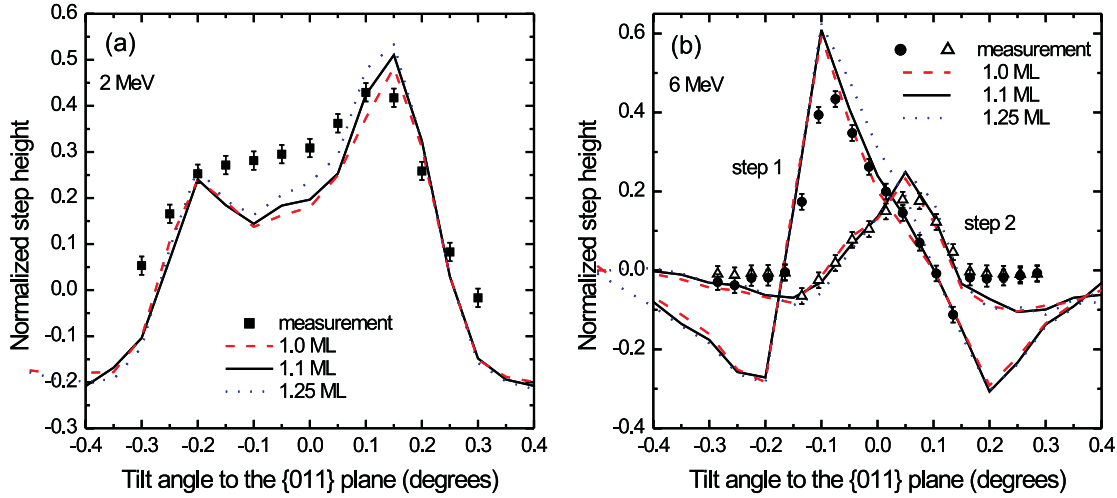


Figure 6.9: Calculated {011} planar step height curves for InAs layers with a thickness of 1.0, 1.1, and 1.25 ML for 2 (a) and 6 MeV  $\text{He}^+$  ions (b). The measured step height curves are also shown.

is much smaller for Ga and As (6 and 0.8% difference in half-wavelength, respectively), than it is for Si (23% difference), for which case the step height curves clearly depend on the ion-atom potential [8].

Finally, the dependence of the shape of the planar step height curves on the thickness of the layers in the InAs/GaAs superlattice is investigated. The thickness of the layers as mentioned in section II were determined with high resolution X-ray diffraction. The thickness of the capping layer was determined with an accuracy of 5 nm, the thickness of the barrier layers is accurate within 2 nanometers, and that of the InAs layers is known with an accuracy of about 0.1 ML, i.e., 0.03 nm [5].

For the axial case, the calculated step height curves for InAs layers with a thickness of 1.0, 1.1, and 1.25 ML could be distinguished, which allowed to determine the translation of the GaAs [011] strings. Just as for the axial case, additional planar channeling simulations are performed with a thickness of 1.0 and 1.25 ML for the InAs layers. The calculated step height curves are shown in Fig. 6.9 together with the measured curves. The differences in the calculated step height curves are small compared to the difference with the measured step height curves, and the resemblance of all the calculated step height curves with the measurements is about equal.

For planar channeling measurements on a single buried nano-film, the shape of the step height curve is determined by the thickness of the capping layer, since this determines the phase of the oscillations [2]. Oscillations in the channeled flux distribution are expected to be still present at the depth of the InAs/GaAs superlattice structure, and therefore, the thickness of the capping layer and barrier layers is expected to influence the measured step height curves. To investigate this presumption, simulations are performed in which the thickness of the capping layer and the barrier layers is varied. The results are presented in Fig. 6.10 for simulations with 2 MeV  $\text{He}^+$  ions. Figure 6.10 (a) indeed shows that the shape of the step height curve depends on the thickness of the capping layer, but again, the differences between the simulated step height curves are small compared to the

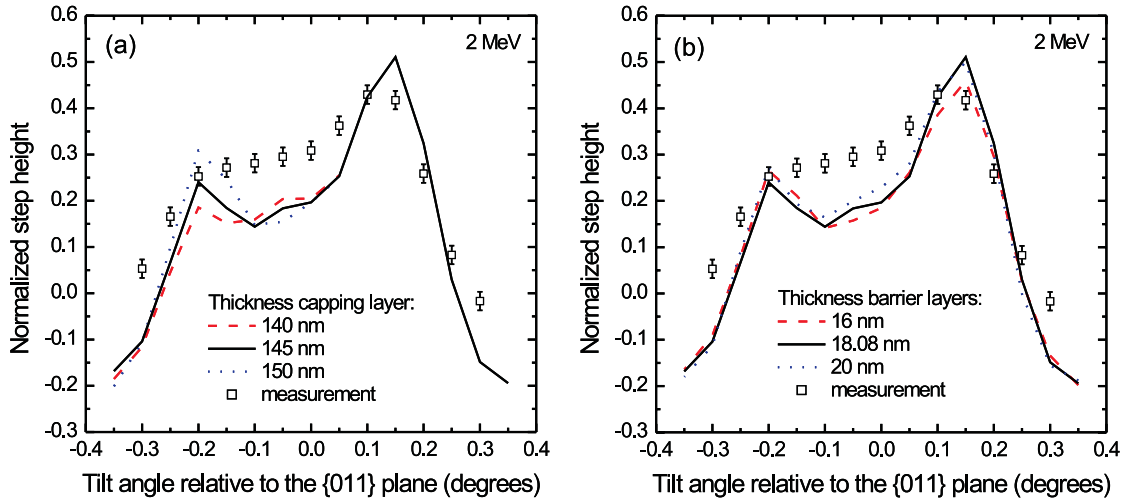


Figure 6.10: Calculated  $\{011\}$  planar step height curves with capping layers with a thickness of 140, 144.9, and 150 nm (a), and with barrier layers with a thickness of 16, 18.08, and 20 nm (b) for 2 MeV  $\text{He}^+$  ions. The measured step height curve is also shown.

differences with the measured step height curve. Also variations in the thickness of the barrier layers result in only small differences in the step height curves compared to the difference with the measurements, see Fig. 6.10 (b). Simulations with 6 MeV  $\text{He}^+$  ions are not presented here, but exactly the same conclusions can be drawn.

Thus, simulations of planar channeling on the InAs/GaAs sample reproduce the correct overall shape of the step height curves, but they are inadequate to obtain a detailed resemblance with the measurements. Furthermore, the outcome of a comparison of a number of simulations with the measurements is not unambiguous, and that implies that for this sample, the translation of the  $\{011\}$  planes can not be determined from planar channeling measurements and MC simulations.

## V Conclusions

Axial and planar channeling measurements and simulations are performed on a InAs/GaAs sample with ten coherent InAs nano-films, to determine the lattice deformation of the buried nano-films.

The axial channeling measurements can be simulated adequately with the Monte Carlo simulation program FLUX7, and the translation of the GaAs  $\{011\}$  lattice strings across each InAs layer can be determined with an accuracy of 0.004 nm. The contributions of the separate InAs layers to the step in a channeled RBS spectrum can not be resolved, but the angular dependence of the height of this step is an average of the tetragonal distortion in the individual InAs layers.

Also planar channeling measurements are presented, which show two step heights in the spectra for experiments with 6 MeV  $\text{He}^+$  ions. This behaviour is caused by the specific combination of the thickness of the barrier layers in between the InAs nano-films and the wavelength of the oscillating trajectories of the channeled ions. The general

outcome of the measurements can be reproduced satisfactorily with the MC simulations, but a detailed agreement is not achieved. Changing the ion-atom potential does not lead to an improvement of the simulations, which also seem to be rather insensitive to the ion-atom potential for the sample under investigation. Furthermore, the calculated step height curves also are insensitive to changes in the translation of the  $\{011\}$  planes, which implies that for this sample the tetragonal distortion can not be determined from planar channeling measurements, in contrast to the results for axial channeling measurements.

## Acknowledgements

The authors wish to thank Willem van der Vleuten and Paul Koenraad for providing the InAs/GaAs sample.

## References

- [\*] Author to whom correspondence should be addressed. FAX: +31 40 243 80 60. Present address: Cyclotron Laboratory, Department of Applied Physics, Eindhoven University of Technology, P.O. Box 513, 5600 MB Eindhoven, The Netherlands. Electronic address: L.J.van.Ijzendoorn@tue.nl.
- [1] L. J. M. Selen, F. J. J. Janssen, L. J. van IJzendoorn, M. J. J. Theunissen, P. J. M. Smulders, and M. J. A. de Voigt, chapter 3 of this thesis (unpublished).
- [2] L. J. M. Selen, F. J. J. Janssen, L. J. van IJzendoorn, M. J. J. Theunissen, P. J. M. Smulders, and M. J. A. de Voigt, chapter 5 of this thesis (unpublished).
- [3] S. T. Picraux, W. K. Chu, W. R. Allen, and J. A. Ellison, *Nucl. Instrum. and Meth. B* **15**, 306 (1986).
- [4] S. T. Picraux, R. M. Bielefeld, W. R. Allen, W. K. Chu, and J. A. Ellison, *Phys. Rev. B* **38**, 11 086 (1988).
- [5] J. Brübach, A. Y. Silov, J. E. M. Haverkort, W. v. d. Vleuten, and J. H. Wolter, *Phys. Rev. B* **59**, 10 315 (1999).
- [6] P. W. L. Van Dijk, Ph.D. thesis, Eindhoven University of Technology, 1997.
- [7] P. J. M. Smulders, and D. O. Boerma, *Nucl. Instrum. and Meth. B* **29**, 471 (1987).
- [8] L. J. M. Selen, L. J. van IJzendoorn, P. J. M. Smulders, and M. J. A. de Voigt, chapter 4 of this thesis (unpublished).
- [9] J. F. Ziegler, J. P. Biersack, and U. Littmark, in *The Stopping and Range of Ions in Solids* (Pergamon Press, New York, 1985).
- [10] L. C. Feldman, J. W. Mayer, and S. T. Picraux, *Materials Analysis by Ion Channeling* (Academic Press, New York, 1982), Chap. 3.



# 7. A channeling study of boron clusters in silicon

L. J. M. Selen, L. J. van IJzendoorn [\*], A. van Loon, and M. J. A. de Voigt

*Research Institutes CPS and COBRA, Cyclotron Laboratory, Department of Applied Physics, Eindhoven University of Technology, P.O. Box 513, 5600 MB Eindhoven, The Netherlands*

Low energy ion implantation at high doses of boron ( $> 10^{15} \text{ cm}^{-2}$ ) in Si is necessary for the fabrication of ultra-shallow junctions, but can result in the undesired presence of boron clusters. These lead to enhanced dechanneling and a direct scattering peak in a channeled RBS spectrum. Values for the dimensions of the lattice distortions in the implanted Si are obtained, by comparing the dechanneling and the direct scattering in the region with clusters to those from Monte Carlo calculations on a curved crystal structure. In the calculations, the direction of the curvature is chosen randomly at the beginning of each ion trajectory. The curved crystal is only a crude estimation of the 3-dimensionally distorted crystal around a cluster. By comparing the outcome of the calculations with the measurements, values of about 0.17 and 65 nm are found for the maximum deformation and the length of the distortions in the crystal, respectively. This implies that the lattice distortions extend significantly outside the layer in which the B clusters are supposed to be present.

## I Introduction

In the development of semiconductor devices, the dimensions of implanted layers keep on decreasing. For the formation of ultra-shallow junctions, low-energy implantation is required, and for boron (B) doping in Si this is suitably achieved by implanting decaborane ( $\text{B}_{10}\text{H}_{14}^+$ ) ions [1,2]. For implantation doses typically higher than  $10^{15} \text{ cm}^{-2}$ , B clusters are introduced in silicon. The threshold for cluster formation is however not easily established due to the small cluster size.

Ion-channeling in combination with Rutherford backscattering spectrometry (RBS) is a well-known technique to investigate strain and defects in thin films. Defects lead to dechanneling and direct scattering in a channeled RBS spectrum, and the relationship between both depends on the type of defect. For point defects, dislocations, and stacking faults this relation is straightforward, which makes it possible to calculate the number of defects from a measured channeling spectrum, but for clusters no definite relation

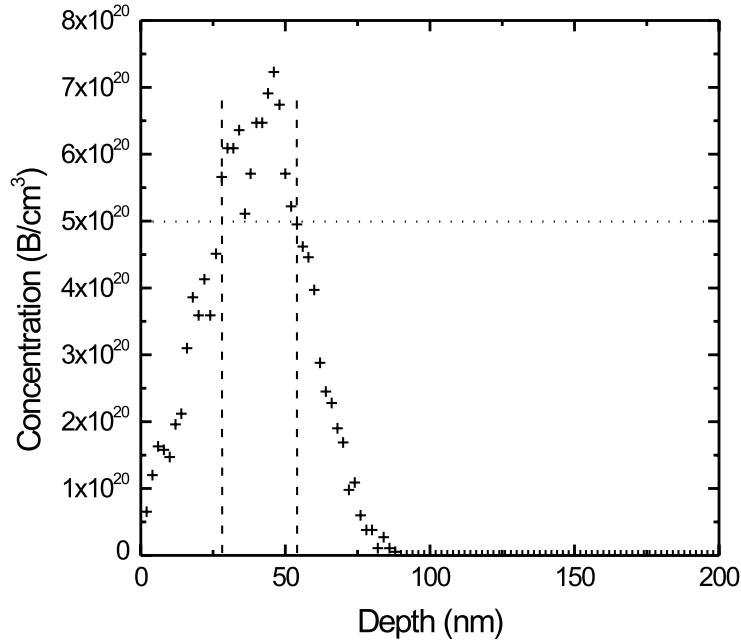


Figure 7.1: The concentration profile of  $3 \times 10^{15} \text{ cm}^{-2}$  10 keV implanted B in Si estimated from calculations with SRIM.

is available [3]. Clusters also induce lattice distortions in the host crystal, and in this paper we intend to obtain information about the dimensions of these lattice distortions by comparing RBS ion-channeling measurements with Monte Carlo calculations.

## II Experiments

Using a high-voltage research implanter, decaborane ( $\text{B}_{10}\text{H}_{14}^+$ ) ion implantation has been performed at an energy of 120 keV, which corresponds to  $\sim 10$  keV per B-atom, at Philips Research Laboratories Eindhoven. The decaborane was implanted in (001) oriented Si wafers with a 400 nm thick  $\text{SiO}_2$  layer and a 205 nm thick Si on insulator (SOI) film on top, produced by the separation by implantation of oxygen (SIMOX) technology. After implantation a 10 s rapid thermal anneal (RTA) in dry nitrogen was applied at a temperature of  $1050^\circ$ . Two samples were prepared by implanting doses of  $3 \times 10^{14}$  and  $3 \times 10^{15} \text{ B/cm}^2$ .

The concentration profile of the implantation of  $3 \times 10^{15} \text{ B/cm}^2$  in a 200 nm thick Si layer has been estimated with SRIM calculations [4], assuming an implantation energy of 10 keV per B atom. The results are presented in Fig. 7.1. The width of the implantation profile is 80 nm and the highest B concentration is found at a depth of 49 nm. Since the solubility of B in Si is approximately  $5 \times 10^{20} \text{ cm}^{-3}$  [5], B-clusters are expected to be present in a depth interval of about 28-54 nm.

The ion-channeling experiments have been performed with 2 and 3.5 MeV  $\text{He}^+$  ion beams from the Philips AVF Cyclotron at the Eindhoven University of Technology. In order to compare the experiments quantitatively, a rotating vane with a gold film was placed in the ion beam. The  $\text{He}^+$  ions scattered from the rotating vane were measured

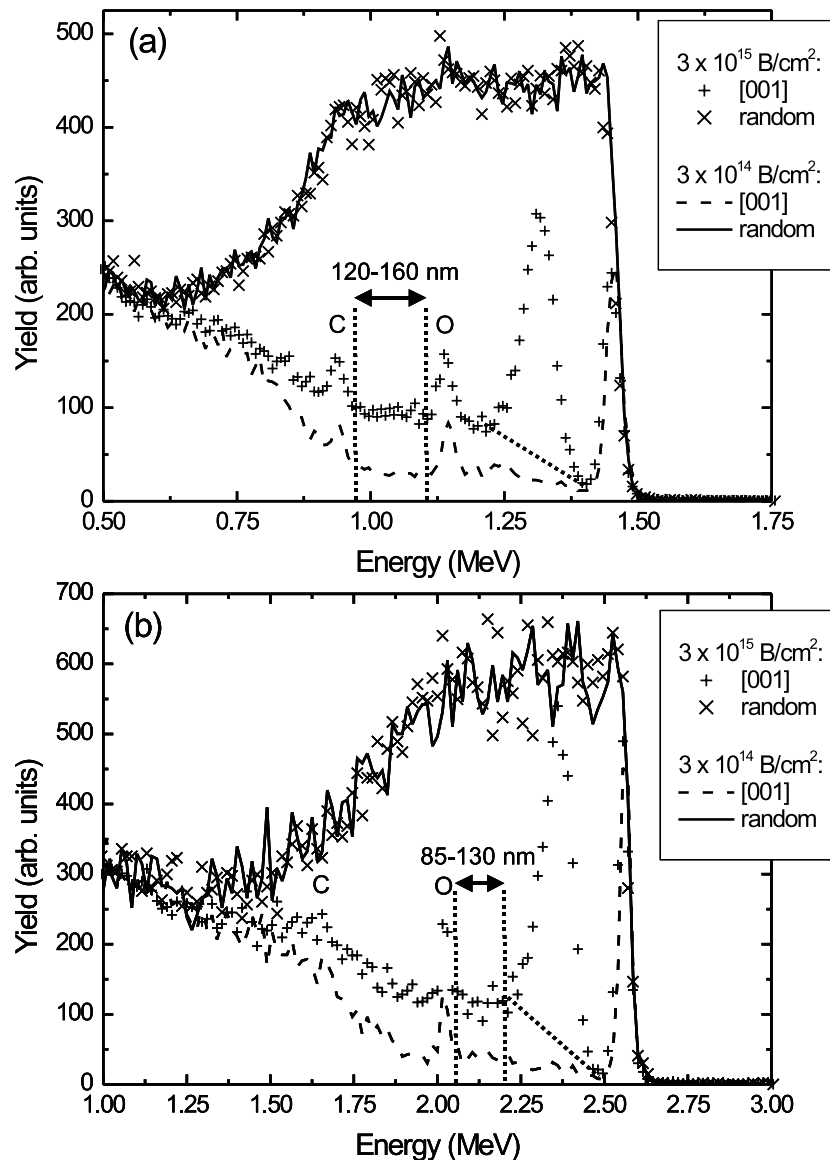


Figure 7.2: RBS spectra of the [001] axial and a non-channeling direction of the  $3 \times 10^{14}$  and  $3 \times 10^{15} \text{ B/cm}^2$  implanted Si samples measured with 2 (a) and 3.5 MeV  $\text{He}^+$  ions (b).

with a  $25 \text{ mm}^2$  Canberra Passivated Implanted Planar Silicon (PIPS) detector with an energy resolution of 20 keV. For the ion-channeling experiments, the samples were placed in a 3-axes goniometer with an angular resolution  $< 0.005^\circ$  [6]. With two sets of slits the beam divergence was limited to  $0.07^\circ$  FWHM. Backscattered ions were detected at a glancing exit angle with a  $25 \text{ mm}^2$  Canberra PIPS detector, and the energy resolution of the detection system was approximately 25 keV.

Figure 7.2 shows the [001] channeled spectra of the two B-implanted Si samples and the spectra for a non-channeling direction, measured at a backscattering angle of  $95^\circ$ . In the channeled spectrum of both samples, an oxygen peak due to the native oxide, a carbon surface impurity, and the Si surface peak (also partially due to the native oxide)



can easily be identified. In the channeled spectrum of the high dose implantation a direct scattering peak attributed to cluster formation can be found at a depth of approximately 45 nm.

Furthermore, for the high-dose-implanted sample the yield behind the direct scattering peak has clearly increased compared to the yield in a virgin Si sample. A direct scattering peak and a higher yield behind this peak are not observed for the low dose implanted sample. The values for the yield in the depth interval of 120-160 nm and 85-130 nm for He<sup>+</sup> ions with an energy of 2 and 3.5 MeV, respectively, and the content of the direct scattering peaks are tabulated in Table I. In case of 2 MeV the content of the direct scattering peak corresponds to  $4.9 \times 10^{16}$  Si/cm<sup>2</sup> equivalent to 36 ML. From Table I it can be seen that the increase of the yield behind the direct scattering peak is  $0.14 \pm 0.01$  and  $0.12 \pm 0.02$  for measurements with 2 and 3.5 MeV He<sup>+</sup> ions, respectively.

For B concentrations in silicon above the solubility, molecular dynamics (MD) calculations predict 4-5 atom stable cluster sizes [7]. This can be compared to an effective defect cluster size of 3 nm in diameter in the silicon as determined with diffuse X-ray scattering [8]. This cluster size was obtained from the Bragg tails (Huang scattering), which give the asymptotic long-range strain fields induced by point defects and point defect clusters [9]. An effective defect cluster of this size in the Si crystal contains about 700 Si atoms.

Assuming that all the B-atoms in the depth interval where the concentration is above the solubility of  $5 \times 10^{20}$  cm<sup>-3</sup>, i.e. 28-54 nm indicated by the dashed lines in Fig. 7.1, have formed clusters,  $1.6 \times 10^{15}$  B/cm<sup>2</sup> will be located in clusters. With an average of 4.5 B atoms per cluster, this would amount to  $3.6 \times 10^{14}$  B clusters/cm<sup>2</sup> and  $2.5 \times 10^{17}$  Si-atoms/cm<sup>2</sup> in effective clusters. Since the density of Si is  $5 \times 10^{22}$ /cm<sup>3</sup>, this corresponds to a deformed Si layer with a thickness of 50 nm. Assuming that all the clusters are situated within the depth interval of 28-54 nm, the calculated effective cluster size implies that defect clusters overlap.

### III Enhanced dechanneling and direct scattering

The presence of defects can lead to enhanced direct scattering and dechanneling compared to those in a perfect crystal. Enhanced direct scattering occurs when the channeled ions are scattered at large angles on the displaced atoms in the defect. The direct scattering

Table I: Values of the scattering yield in a channeling experiment in the depth interval of 120-160 nm (for 2 MeV) and 85-130 nm (for 3.5 MeV), and the content of the direct scattering peak of Si samples implanted with  $3 \times 10^{14}$  and  $3 \times 10^{15}$  B/cm<sup>2</sup> from RBS channeling measurements with 2 and 3.5 MeV He<sup>+</sup> ions.

	$3 \times 10^{14}$ B/cm <sup>2</sup>		$3 \times 10^{15}$ B/cm <sup>2</sup>	
	2 MeV	3.5 MeV	2 MeV	3.5 MeV
direct scattering	-	-	$36 \pm 2$ ML	$59 \pm 3$ ML
channeling yield	$0.070 \pm 0.005$	$0.07 \pm 0.01$	$0.208 \pm 0.008$	$0.19 \pm 0.01$

contribution depends on the geometry of the defect, and therefore, a defect scattering factor  $f$  is used to account for any difference between the number of defects and the effective number of scattering centers per defect [3].  $f$  can vary from 1, for a.o. single displaced atoms, to almost zero, for defects that consist of only small distortions from the ideal lattice, like a dislocation. In general, detailed knowledge about the defect is required to interpret direct scattering yields of defects quantitatively. For the distorted Si lattice around the B clusters, the value of  $f$  will be somewhere in between 1 and zero. Furthermore, the presence of defects in general increases the non-channeled fraction of the beam in the crystal, which leads to an increase in the scattering yield in a channeled spectrum. Enhanced dechanneling can arise from displaced atoms and extended defects. Dechanneling due to defect-induced distortions of the channels occurs when the angular distortions of the channels become significant relative to the channeling critical angle for the channeled ions.

At first, it is interesting to calculate the amount of dechanneling expected when all atoms involved would be in amorphous clusters. The upper limit of the number of atoms involved in the clusters can be estimated from the X-ray results ( $\sim 2.5 \times 10^{17}$ ). When the average number of atoms in clusters over the depth traversed by the beam exceeds  $10^{17}/\text{cm}^2$ , amorphous clusters can no longer be treated as isolated point defects in calculating the dechanneling due to these clusters, but multiple scattering theory has to be used to calculate the dechanneling [3]. For multiple scattering theory the dechanneling due to amorphous clusters containing  $2.5 \times 10^{17}$  Si-atoms/ $\text{cm}^2$  (based on the X-ray scattering results [8]) is equal to that of an amorphous Si layer containing the same amount of Si atoms. This corresponds to a layer with a thickness of 50 nm. Note that this layer is about twice as thick as the depth interval where the B clusters are presumed.

The mean number  $m$  of collisions of the ions with  $nt$  atoms/ $\text{cm}^2$  in an amorphous layer of thickness  $t$  and atomic density  $n$  is given by  $m = \pi a^2 nt$ , where the Thomas-Fermi screening distance  $a$  is taken as the cross-sectional radius for such scattering events [3],  $nt = 2.5 \times 10^{17} \text{ cm}^{-2}$ , and for  $\text{He}^+$  ions in Si  $a = 0.17 \text{ \AA}$ , which gives  $m = 2.3$ . From multiple scattering theory the non-channeled yield is given by  $\chi_{min} = P(\tilde{\theta}_c, m)$ , with the reduced critical angle  $\tilde{\theta}_c$  given by  $\tilde{\theta}_c = \frac{aE\psi_{1/2}}{8\pi\epsilon_0 Z_1 Z_2 e^2}$ , where  $E$  is the energy of the beam and  $\psi_{1/2}$  is given by Barrett's critical half-width  $\psi_c^B$  [10]. The fraction  $P(\tilde{\theta}_c, m)$  of particles scattered outside the reduced critical angle  $\tilde{\theta}_c$  is given by  $P(\tilde{\theta}_c, m) = \int_{\tilde{\theta}_c}^{\infty} f_1(m, \tilde{\theta}) \tilde{\theta} d\tilde{\theta}$ , which can be determined from numerical integration of the  $f_1$  tables in Sigmund and Winterbon [11]. With  $\psi_c^B$  7.5 and 5.7 mrad for 2 and 3.5 MeV  $\text{He}^+$  ions in Si, respectively, the values of  $P(\tilde{\theta}_c, m)$  are about 0.04 and 0.02 for 2 and 3.5 MeV, respectively. The amount of dechanneling thus decreases when the beam energy is increased, since the beam angular distribution narrows more than the critical angle decreases. This must be compared to strained regions, where the dechanneling increases with increasing energy [3].

Comparison of these values with the measured values of the increase in scattering yield from Table I shows that the calculated values for amorphous clusters are significantly lower than the values in the deformed Si crystal around the B clusters, which are 0.14 and 0.12 for measurements with 2 and 3.5 MeV  $\text{He}^+$  ions, respectively. Apparently, for a certain number of Si atoms, long range steering effects in a distorted lattice give rise to a larger increase of the scattering yield, than an amorphous layer. Furthermore, the energy

dependence of the increase in scattering yield in the measurements (see Table I) is by far not as strong as for an amorphous layer.

These calculations clearly show that the increased scattering yield in a lattice distorted by the presence of clusters is significantly different from the increased scattering yield due to amorphous clusters, and these calculations therefore rule out amorphous clusters of the size corresponding to the effective defect cluster size measured with X-ray scattering. In order to obtain more detailed information about a more plausible structure of the distortions, Monte Carlo (MC) channeling simulations were used.

## IV Monte Carlo simulations of defect clusters

For the Monte Carlo (MC) channeling calculations, the computer program FLUX7 was used, which is an improved and extended version of FLUX [12]. The physical model incorporated in FLUX7 is based on binary collisions of the incoming ion and the target nuclei governed by the well-known universal potential of Ziegler, Biersack, and Littmark [4]. One of the output parameters of FLUX7 is the nuclear encounter probability (NEP) with a target atom to cause an event such as large angle scattering (in RBS), a high-energy recoil of the target atom, or a nuclear reaction. The NEP is normalized by the probability for a random medium with the same density of atoms [12]. The FLUX7 simulation code is used to calculate the NEP as a function of depth.

In FLUX7, the  $xy$ -plane perpendicular to the string direction  $z$  is divided into rectangular cells, which are chosen such that they contain one atomic row each and can be carried over into one another by a simple translation and/or reflection. The calculation is confined to one of these unit cells, and when the ion leaves the cell during the course of its path it is put back at an equivalent position in the original cell by an appropriate symmetry operation on its coordinates and velocity components [12]. With FLUX7 different kinds of lattice deformations can be simulated: strained layers cause a kink along off-normal crystal axes and planes, which can be simulated by rotating the velocity vector at the interfaces, and a bent crystal can be simulated by the option 'curvature', which specifies a radius of the curvature and a plane perpendicular to the crystal axis by giving an angle  $\phi$  of the intersection with the  $xy$ -plane. In the calculations with FLUX7 however, only a homogeneous deformation of the total crystal can be simulated, which is different from the 3-dimensionally deformed Si crystal around the B clusters.

Regarding the overlap of the effective defect clusters, we assume that the complete Si crystal in the depth interval of 28-54 nm is slightly deformed due to the B clusters. To estimate the average deformation of the Si crystal with Monte Carlo calculations the 'curvature' option is used. Figure 7.3 (a) shows the deformation of the Si lattice as used in the calculations, where the channeled ions have to travel through a double chicane in the channel on traversing the lattice deformations around a B cluster. To imitate the 3-dimensionality of the lattice deformation around a B cluster, the direction of the curvature specified by  $\phi$  is randomly assigned at the beginning of the calculation of each ion trajectory. In these calculations two parameters are introduced: the distortion length and the maximum displacement, both indicated in Fig. 7.3 (a). In the calculations the depth, at which the maximum displacement is situated, is kept constant at 40 nm, which

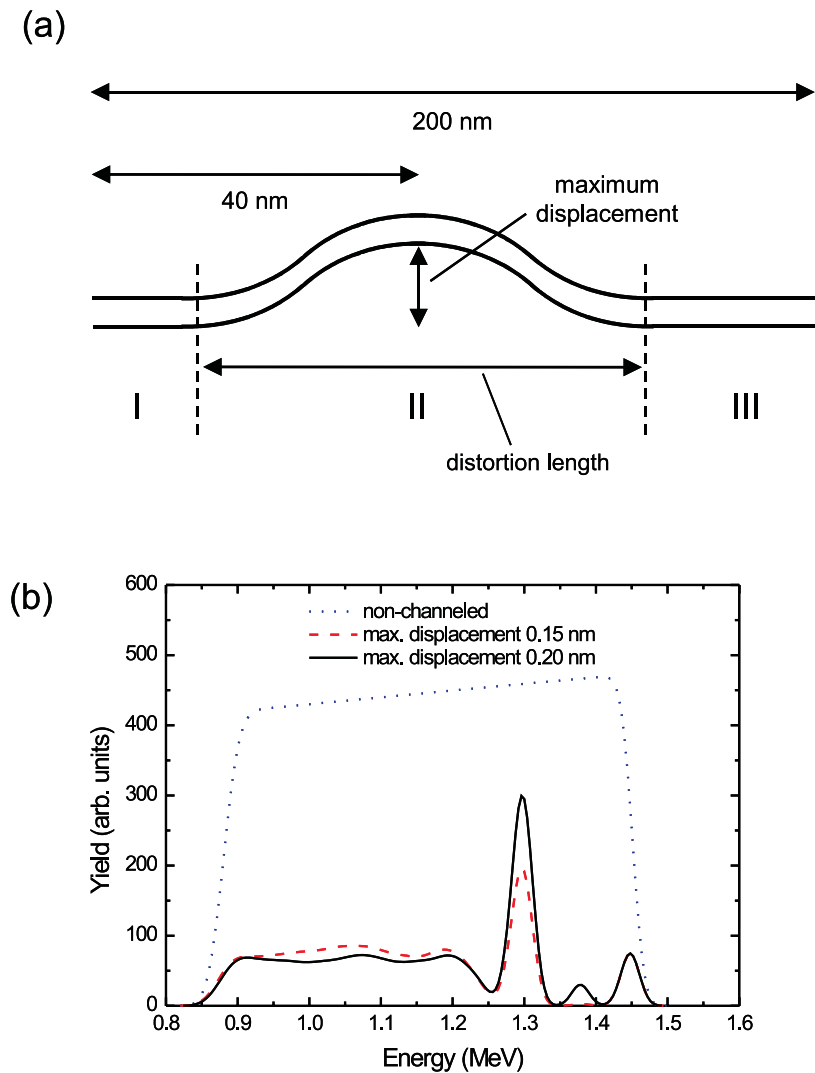


Figure 7.3: Deformation of the crystal lattice as used in the Monte Carlo calculations (a), and an example of the calculated NEP as a function of depth for a distortion length of 65 nm (240 ML) and a maximum displacement of 0.15 nm (b) with 2 MeV  $\text{He}^+$  ions.

corresponds to the middle of the depth interval where B clusters are expected to be present. Furthermore, the total sample length is kept constant at 200 nm. Since FLUX7 can handle only two different layers per calculation, the calculations are divided in three parts, as indicated in Fig. 7.3 (a).

The results of the FLUX7 simulations are presented as the NEP, energy loss, and straggling as a function of depth. These can be used to generate RBS spectra of scattered ions with the program RBSIM [12]. Examples of such calculated spectra are shown in Fig. 7.3 (b), for a non-channeled ion beam, and for [001] channeled ion beams in a crystal with deformations characterized by a distortion length of 65 nm (240 ML) and maximum displacements of 0.15 and 0.20 nm, respectively. The same backscattering angle and energy resolution are used as in the experiments. The first thing to note is that the calculated spectrum for a maximum displacement of 0.20 nm exhibits two peaks in the

region of the curved crystal. Depending on the ratio of the maximum displacement and the distortion length, one or two direct scattering peaks appear, as can be seen in Fig. 7.3 (b) for a maximum displacement of 0.15 and 0.20 nm, respectively. In the measurement, no fixed ratio between the maximum displacement and the distortion length occurs, and only one direct scattering peak is observed. It is assumed that the average ratio of the distortions in the sample with B clusters can be compared to the ratio adopted in the simulations. We will compare the contents of the direct scattering peaks in the measured and calculated spectra, to obtain information about the dimensions of the distortions around clusters.

Furthermore, the full width at half maximum (FWHM) of the direct scatter peaks occurring in the calculated channeling spectra is smaller than the FWHM of the direct scatter peak in the measured spectrum (see Fig. 7.2), which is mostly due to the fixed depth of the maximum displacement in the calculations, while an approximately Gaussian distribution of B clusters is assumed to be present in the measured sample. Finally, the surface peak in the measured spectrum is larger than in the calculated spectra due to the presence of carbon and silicon-oxide at the surface of the measured sample. The overall shape of the calculated spectra is nevertheless in satisfactory agreement with the shape of the measured spectrum.

For a comparison of the calculations with the measurements, the average NEP in the interval of the curvature is compared to that for a perfect crystal, and the difference is a measure for the direct scattering contribution, which can be compared to the content of the measured direct scattering peak. The same is done for the average NEP in the intervals of 120-160 and 85-130 nm for simulations with 2 and 3.5 MeV He<sup>+</sup> ions, respectively, and the results can be compared to the measured increase in scattering yield due to dechanneling by the lattice distortions. The calculated direct scattering and scattering yield due to dechanneling are plotted in Fig. 7.4 and 7.5, for 2 and 3.5 MeV He<sup>+</sup> ions, respectively.

Figures 7.4 (a) and 7.5 (a) show the increased average NEP in the intervals of 120-160 and 85-130 nm, respectively, as a function of the maximum displacement. The different curves are for calculations with different distortion lengths, expressed in ML, where 1 ML is 0.271 nm for Si, along the [001] axis. For increasing maximum displacement, the scattering yield due to dechanneling goes to a maximum value, which roughly scales linearly with the distortion length. The maximum displacement where the plateau in the scattering yield values starts, depends on the curvature and the value of the maximum displacement relative to the distance of opposite rows in the [001] channels. Figures 7.4 (b) and 7.5 (b) show the calculated direct scattering in units of the direct scattering from 1 ML of randomly oriented Si. The direct scattering increases with increasing distortion length for values of the maximum displacement larger than 0.20 nm. For maximum displacement values between 0.05 and 0.20 nm, the direct scattering depends differently on the distortion length. In Fig. 7.6, the direct scattering is plotted as a function of the distortion length for different values of the maximum displacement. For values of the maximum displacement of 0.10 and 0.15 nm, clearly a maximum appears in the curve of the direct scattering value. Apparently, when the value of the curvature drops beneath a critical value, part of the ions is more or less able to 'follow' the curvature in the crystal, and this part increases with decreasing curvature. Furthermore, from a comparison of Fig. 7.6 (a) and (b) it can be seen that this critical value increases with increasing energy

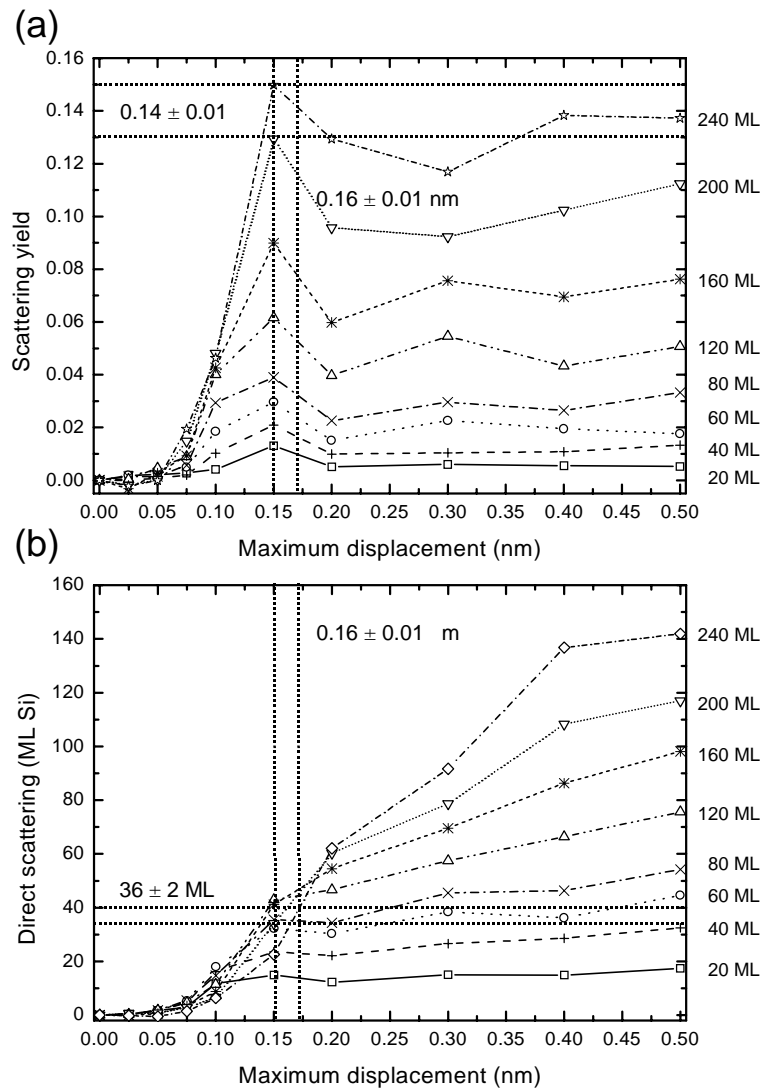


Figure 7.4: Calculated increased scattering (a) and direct scattering (b) for distortion lengths between 20 and 240 ML, and maximum displacements between 0.025 and 0.50 nm, for 2 MeV He<sup>+</sup> ions.

of the channeled ions. This is plausible since the critical angle  $\psi_1$  for channeling decreases with increasing energy; for channeling along the [001] axis in Si,  $\psi_1$  is 0.49 and 0.37° for 2 and 3.5 MeV He<sup>+</sup> ions, respectively.

In the measurements, an increase of the scattering yield in the depth interval 120-160 nm of  $0.14 \pm 0.01$  was found for 2 MeV He<sup>+</sup> ions. Comparing this with the results of Fig. 7.4 (a), we must conclude that this corresponds with a distortion length of at least 200 ML, i.e. 54.2 nm. The content of the direct scattering peak in the measured spectrum is  $36 \pm 2$  ML, and when this is compared to the direct scattering values in Fig. 7.4 (b), a maximum displacement value of  $0.16 \pm 0.01$  nm is found for distortion lengths of 200 ML and up. This value is in good agreement with Fig. 7.4 (a). The conclusion can be drawn that in the measurements, the ions on average experience a distortion of the Si lattice over a length of about 200-240 ML, which corresponds to 54-65 nm, and with a

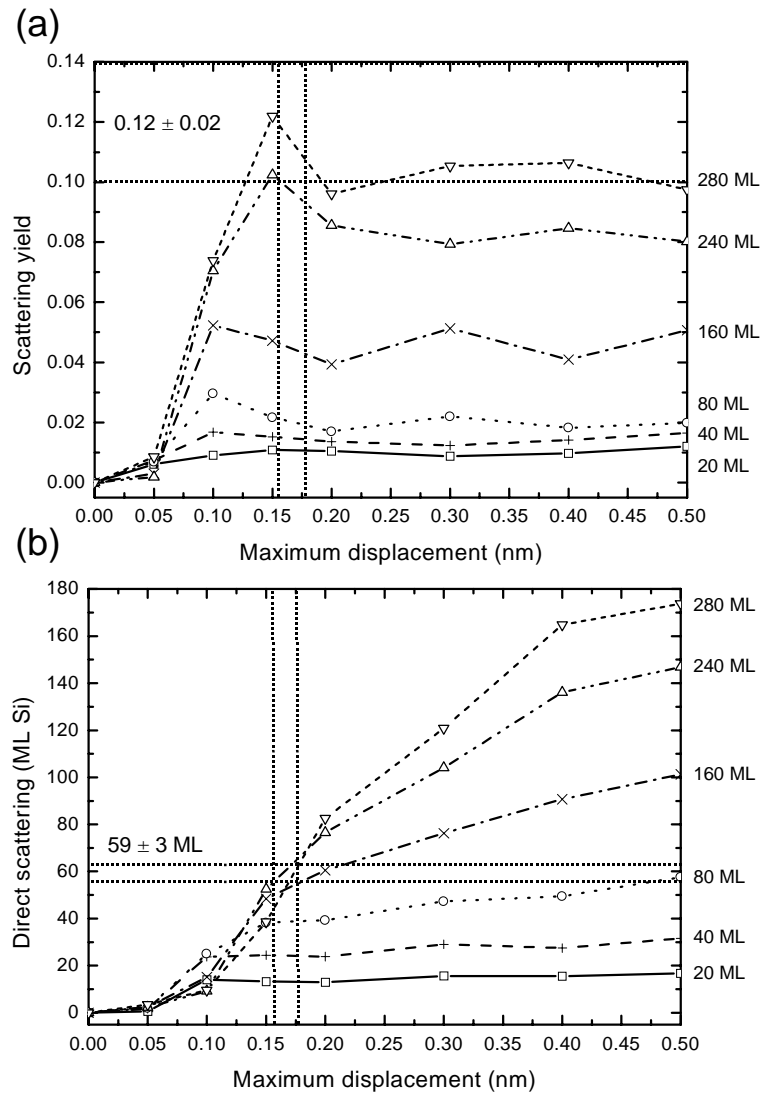


Figure 7.5: Calculated increased scattering (a) and direct scattering (b) for distortion lengths between 20 and 280 ML, and maximum displacements between 0.05 and 0.50 nm, for 3.5 MeV  $\text{He}^+$  ions.

maximum displacement of the crystal channels of  $0.16 \pm 0.01$  nm.

The same procedure can be followed for 3.5 MeV  $\text{He}^+$  ions by comparing the measured values of Table I with the results of the calculations in Fig. 7.5. For a dechanneling value of  $0.12 \pm 2$  and a direct scattering value of  $59 \pm 3$  ML Si, a distortion length of about 240-280 ML (65-76 nm) and a maximum displacement value of  $0.17 \pm 0.01$  nm can be extracted from Fig. 7.5. These values are in good agreement with the results for 2 MeV  $\text{He}^+$  ions. Note that a distortion length of more than 80 nm (295 ML) has no meaning, since the maximum displacement is situated at a depth of 40 nm.

The size of a 4-5 atom B cluster as predicted by the MD-calculations is approximately 0.3 nm, which can be used as an upper limit for the maximum displacement appearing in the channels of the distorted Si crystal. These values are of the same order of magnitude as the values found from the comparison of measurements and calculations above. The

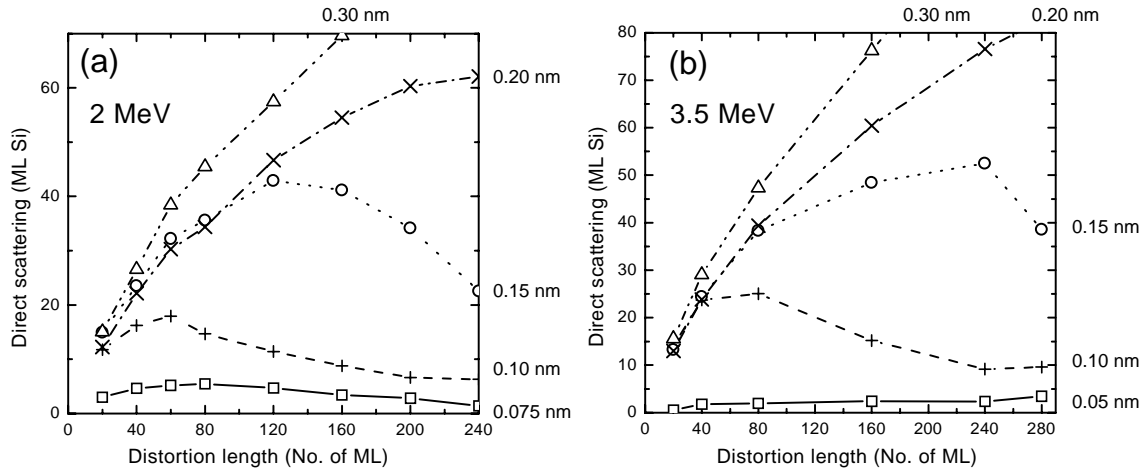


Figure 7.6: Calculated direct scattering as a function of the distortion length for maximum displacements between 0.05 and 0.30 nm, for 2 (a) and 3.5 MeV  $\text{He}^+$  ions (b).

curved crystal is thus clearly a more plausible structure for the distortions in the silicon crystal lattice due to the presence of clusters, than the amorphous clusters regarded in section III.

The results from our measurements and MC calculations support the relieve of strain induced by clusters with strain fields over a scale of tenths of nanometers, which is in agreement with the long range strain fields measured in the Bragg tails of XRD [8]. A similar situation occurs for quantum dots (QDs). The strain in and around buried quantum dots is relieved via extended strain fields, which also results in inhomogeneous deformations in the host lattice. It is known from strain measurements and calculations on buried quantum dots, that those strain fields extend up to tenths of nm into the host crystal [13, 14], which can be compared to the values for the distortion length we found above.

## V Conclusions

Channeling is a sensitive tool for measuring lattice deformations in silicon induced by B clusters. Low energy ion implantation at high doses of B ( $> 10^{15} \text{ cm}^{-2}$ ) in Si give rise to the presence of clusters, which lead to enhanced dechanneling and a direct scattering peak in a channeled RBS spectrum. The lattice distortions in the implanted Si give rise to increased yields in a RBS channeling spectrum due to dechanneling and direct scattering in the clustered region. By comparison of these increased yields with the increased yields in a calculated NEP spectrum on a curved crystal structure, we obtain values for the dimensions of the lattice distortions in the implanted Si. In the calculations a curved crystal is used with the direction of the curvature chosen randomly at the beginning of each ion's trajectory. By comparing the outcome of the calculations with the measurements, realistic values are found for the dimensions of the distortions in the Si lattice: the distortion length is about 65 nm, and the maximum displacement  $0.17 \pm 0.01$  nm. By comparison with RBS channeling measurements, MC calculations prove to be an interesting auxiliary



tool for the characterization of crystal deformations around clusters.

## Acknowledgements

The authors are indebted to Pascal Bancken (Philips Research Laboratories Eindhoven), who implanted the Si samples.

## References

- [\*] Author to whom correspondence should be addressed. FAX: +31 40 243 80 60. Present address: Cyclotron Laboratory, Department of Applied Physics, Eindhoven University of Technology, P.O. Box 513, 5600 MB Eindhoven, The Netherlands. Electronic address: L.J.van.IJzendoorn@tue.nl.
- [1] A. G. Dirks, P. H. L. Bancken, J. Politiek, N. E. B. Cowern, J. H. M. Sniijders, J. G. M. van Berkum, and M. A. Verheijen, *IIT conference proceedings*, Kyoto (1998).
- [2] A. Agarwal, H.-J. Gossmann, D. C. Jacobson, D. J. Eaglesham, M. Sosnowski, J. M. Poate, I. Yamada, J. Matsuo, and T. E. Haynes, *Appl. Phys. Lett.* **73**, 2015 (1998).
- [3] L. C. Feldman, J. W. Mayer, and S. T. Picraux, *Materials Analysis by Ion Channeling* (Academic Press, New York, 1982).
- [4] J. F. Ziegler, J. P. Biersack, and U. Littmark, *The Stopping and Range of Ions in Solids* (Pergamon Press, New York, 1985).
- [5] W. C. O'Mara, R. B. Herring, and L. P. Hunt, *Handbook of Semiconductor Silicon Technology* (Park Ridge, Noyes, 1990).
- [6] P. W. L. Van Dijk, Ph.D. thesis, Eindhoven University of Technology, 1997.
- [7] A. Agarwal, H. Gossmann, D. J. Eaglesham, D. C. Jacobson, T. E. Haynes, J. Jackson, Yu. E. Erokhin, and J. M. Poate, *4th International Workshop on Measurement, Characterization and Modeling of Ultra-Shallow Doping Profiles*, 1997, pp. 39.139.9.
- [8] U. Beck, T. H. Metzger, J. Peisl, and J. R. Patel, *Appl. Phys. Lett.* **76**, 2698 (2000).
- [9] S. Grotehans, G. Wallner, E. Burkel, H. Metzger, J. Peisl, and H. Wagner, *Appl. Phys. Lett.* **50**, 416 (1987).
- [10] J. H. Barrett, *Phys. Rev. B* **3**, 1527 (1971).
- [11] P. Sigmund and W. K. Winterbon, *Nucl. Instrum. and Meth.* **119**, 541 (1974).
- [12] P. J. M. Smulders and D. O. Boerma, *Nucl. Instrum. and Meth. B* **29**, 471 (1987).
- [13] M. Grundmann, O. Stier, and D. Bimberg, *Phys. Rev. B* **52**, 11969 (1995).
- [14] L. J. M. Selen, L. J. van IJzendoorn, M. J. A. de Voigt, and P. M. Koenraad, *Phys. Rev. B* **61**, 8270 (2000).

# 8. Transmitted ion energy loss distributions to detect cluster formation in silicon

L. J. M. Selen, A. van Loon, L. J. van IJzendoorn [\*], and M. J. A. de Voigt

*Research Institutes CPS and COBRA, Cyclotron Laboratory, Department of Applied Physics, Eindhoven University of Technology, P.O. Box 513, 5600 MB Eindhoven, The Netherlands*

The energy loss distribution of ions transmitted through a  $5.7 \pm 0.2$   $\mu\text{m}$  thick Si crystal was measured and simulated with the Monte Carlo channeling simulation code FLUX. A general resemblance between the measured and simulated energy loss distributions was obtained after incorporation of an energy dependent energy loss in the simulation program. The energy loss calculations are used to investigate the feasibility to detect the presence of light element dopant clusters in a host crystal from the shape of the energy loss distribution, with transmission ion-channeling. A curved crystal structure is used as a model for a region in the host crystal with clusters. The presence of the curvature does have a large influence on the transmitted energy distribution, which offers the possibility to determine the presence of dopant clusters in a host crystal with transmission ion-channeling.

## I Introduction

In the development of semiconductor devices, the dimensions of implanted layers keep on decreasing. For the formation of ultra-shallow junctions, low-energy ion implantation can be applied, and for boron (B) doping in Si this is suitably achieved by implanting decaborane ( $\text{B}_{10}\text{H}_{14}^+$ ) ions [1, 2]. For low energy implantations, high B concentrations approaching the solid solubility are produced, and undesired cluster formation easily occurs. The threshold for cluster formation is however not easily established due to the small cluster size.

MeV ion-channeling in combination with Rutherford backscattering spectrometry (RBS) is a well-known technique to investigate strain and defects in thin films. Defects lead to dechanneling and direct scattering in a channeled RBS spectrum, and the relationship between both depends on the type of defect. For point defects, dislocations, and stacking faults this relation is straightforward, which makes it possible to calculate the number of

defects from a measured RBS channeling spectrum, but for clusters no definite relation is available [3].

Transmission techniques are used for different kinds of analysis, of which measuring stopping powers is one of the most well-known. By measuring the energy loss of particles passing through thin self-supporting foils of which the areal density is known exactly, the stopping power can directly be determined [4–6]. Another well-known transmission technique is scanning transmission ion microscopy (STIM), which is mostly applied to measure the mean energy loss for imaging differences in the local layer thickness in biological samples. Combination of transmission ion-channeling with a nuclear microprobe, brings imaging of stacking faults or interface dislocations within reach, as is demonstrated in the channeling scanning transmission ion microscopy (CSTIM) technique [7,8]. In this technique, which is usually applied with proton beams on samples with a thickness of typically 20-50  $\mu\text{m}$ , only the mean energy loss is considered. When the transmission technique is combined with ion-channeling for crystals of several microns thick, also an energy loss distribution can be measured. From this energy loss distribution it was concluded that the energy loss of channeled ions is typically about 60% of the energy loss experienced by non-channeled ions, and that the average energy loss experienced by channeled ions depends on their transverse energy in the channel [9, 10]. Simulations which reproduce these energy loss distributions have not been reported in literature.

If precipitates or clusters are present in a host crystal, they will induce lattice deformations, and consequently, part of the channeled fraction of the ion beam will dechannel. If the effect of dopant clusters on the morphology of the host crystal is large enough to change the energy distribution of the transmitted ion beam, this can provide a method to determine the critical implantation dose for clustering, with transmission ion-channeling.

In this paper it will be investigated whether energy loss *distributions* can be simulated and used to detect lattice deformations in crystals. In particular, the possibility of detecting B clusters in a silicon wafer with an unfocused ion beam will be investigated. To obtain detailed information on the transmitted energy distribution, Monte Carlo (MC) calculations are needed. Most of the MC channeling simulation codes exhibit an energy independent stopping power, which is only valid for thin samples where the total energy loss of the ions through the sample is small compared to the incident energy of the ions. Therefore, a study is performed first to investigate the required energy loss model incorporated in the MC calculations.

## II Experiments

The range of 4 MeV He ions in silicon is about 11  $\mu\text{m}$ , which limits the thickness of samples for transmission channeling experiments. Consequently, wafers with thin-etched windows are required to perform transmission channeling experiments. Furthermore, a uniform thickness of the etched window is a necessity for measuring energy loss distributions. The most common chemical etching technique for Si uses B ion implantation or diffusion at 1050° to obtain an etch stop in the Si wafer [11]. This method poses severe limitations in the context of lattice deformation studies, since the intrinsic sample properties are modified due to lattice deformation by B doping. That makes this method unsuitable for

studying B clusters. In order to investigate the energy loss distribution, measurements were performed on a commercially available thin-etched self-supporting 2 inch Si wafer obtained from Virginia Semiconductors of several microns thick. The wafer was cut into pieces of about 1 cm<sup>2</sup>, and the pieces were clamped on a target holder with teflon rings in order to obtain a flat sample.

The ion-channeling experiments have been performed with 4 MeV He<sup>+</sup> ion beams from the Philips AVF Cyclotron at the Eindhoven University of Technology. The Cyclotron was tuned to an energy of 4 MeV, but the exact energy of the beam can have a systematic uncertainty of at most 20 keV with the nominal value of 4.000 MeV. The corresponding systematic uncertainty in the stopping of He ions in silicon is at most 0.3% of the value at 4 MeV. Note that in the present paper the shape of the energy loss distribution is investigated without pretending to measure the absolute value of the stopping. In the remainder of this paper a beam energy of 4.000 MeV is adopted. The samples were placed in a 3-axes goniometer with an angular resolution < 0.005° [10]. With two sets of slits the beam divergence was limited to 0.01° FWHM. The transmitted ions were detected in transmission geometry at a forward scattering angle of 0° (bright field transmission channeling) with a 100 mm<sup>2</sup> Canberra passivated implanted planar silicon (PIPS) detector at a distance of 120 mm from the target. The overall energy resolution of the detection system was about 22 keV. The count rate in the detector was limited to < 10.000 counts per second by means of two energy dispersive slits in the beam guiding system. In order to find the transmission location, a scan with the detector was made in the angular region of -5 to +5°. Alignment of the beam with the [001] axial and {011} planar directions of the Si wafer was found with the detector positioned at a forward scattering angle of 30° (dark field transmission channeling).

Figure 8.1 shows the measured transmitted energy distributions for the [001] axial channeled, the {011} planar channeled, a non-channeling direction, and for the incident beam itself. The {011} planar channeled spectrum was measured with the beam tilted 2° out of the [001] axis. The random spectrum is measured during spinning the sample 90° around its surface normal, after the beam was tilted away from the [001] axis by 3°. Normalization of the spectra was carried out with respect to the number of ions detected.

For a better mutual comparison of their shapes, the energy spectra in Fig. 8.1 have been scaled, with the scaling factors indicated for each spectrum. The non-channeled spectrum shows a peak in the energy distribution with a maximum at  $2957 \pm 2$  keV, and a full width at half maximum (FWHM) of 70 keV due to energy straggling, to variations in the thickness of the sample, and to the resolution of the detection system. Notice that the non-channeling energy distribution has a small tail towards the low-energy-loss side due to incidentally channeled ions. The average stopping power, i.e. the energy loss per unit of distance, experienced by non-channeled transmitted ions can be approximated by [6]:

$$S(\bar{E}) = S(E_i - \bar{\Delta E}/2) = \bar{\Delta E}/x, \quad (8.1)$$

where  $E_i$  is the beam energy,  $\bar{\Delta E}$  the mean energy loss in the target of thickness  $x$ , and  $E_i - \bar{\Delta E}/2$  the arithmetic mean energy of the beam in the target. In this approximation,  $S(\bar{E})$  is found to be overestimated no more than 0.05% for decreasing values of the stopping powers in the Bethe region and for  $\bar{\Delta E}/E_i < 0.6$ . We use formula (8.1) and the Ziegler value [4] for the stopping power at  $\bar{E}$  in our measurement to estimate the thickness

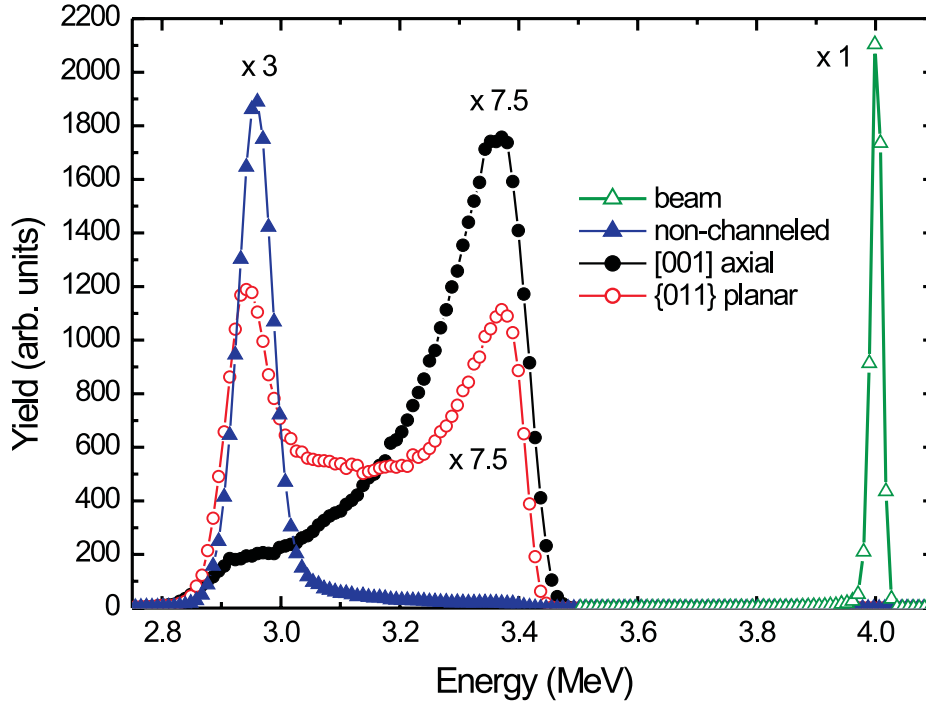


Figure 8.1: Measured energy distributions for the [001] axial channeled, the {011} planar channeled, a non-channeled direction, and the incident beam for 4 MeV  $\text{He}^+$  ions directed on a 5.7  $\mu\text{m}$  thick Si wafer.

of the sample. The *average* energy of the measured transmitted non-channeled energy distribution is  $2972 \pm 2$  keV, which implies that  $\overline{E} = 3486 \pm 2$  keV and  $\overline{\Delta E} = 1028 \pm 2$  keV. The energy loss of He ions in Si with  $\overline{E} = 3486$  keV is  $180 \pm 7$  eV/nm [4]. From these values we find that the thickness of the traversed sample is  $5.7 \pm 0.2$   $\mu\text{m}$ .

The [001] axial channeled spectrum shows huge differences in the energy loss distribution compared to the non-channeled spectrum. The peak in the distribution is found at a much higher energy in the spectrum, a tail towards the non-channeled energy loss peak occurs, and the FWHM is far larger for the peak in the [001] channeled energy distribution ( $\sim 170$  keV). The width of the peak can be assigned to the differences in electron density as experienced by channeled ions with different transverse energies in the channels. The maximum yield in the measured [001] channeled energy distribution occurs at an energy of  $3360 \pm 5$  keV. The corresponding energy loss is  $640 \pm 5$  keV, and the energy loss corresponding to the peak value in the energy distribution of the non-channeled ions is  $1043 \pm 2$  keV. Here we define the ratio in energy loss corresponding to these peak values as the channeled-to-non-channeled energy-loss-ratio, which is  $0.61 \pm 0.01$  in the measurements.

The spectrum of the {011} planar channeled ions shows a contribution of best channeled ions with an energy comparable to that of the best axial channeled ions in the [001] spectrum. Furthermore, a large contribution of non-channeled ions is observed in the energy distribution. The reason is that only about 75% of the ions in the incoming beam becomes initially channeled in the {011} planes, which must be compared to about 97% in case of [001] axial channeling. The difference is due to a larger surface coverage

of atomic planes compared to that of atomic strings. Finally, the high-energy-loss part of the {011} planar channeled energy distribution shows a component with a larger energy loss, than for a non-channeled direction. This implies that some ions experienced a more than average electron density along their trajectories, which can be assigned to ions with a high transverse energy. These ions have strongly oscillating trajectories in between the {011} planes, and spend a large part of their trajectory close to the core electron density in the vicinity of the planes.

### III Monte Carlo calculations and energy loss

For the Monte Carlo (MC) channeling calculations, the computer program FLUX7 was used, which is an improved and extended version of FLUX [12]. The physical model, incorporated in FLUX7 for the angular deflection, consists of contributions from interactions of the ions with the target atoms in the nearest string (described with binary collisions governed by a screened Coulomb potential), the atoms in surrounding strings (described with a thermally modified continuum potential), and the target electrons (treated in a multiple scattering approximation). The calculations were performed with the well-known universal potential of Ziegler, Biersack, and Littmark [4]. The treatment of the energy loss in FLUX7 consists of two components. The energy loss due to interaction with target atom cores is approximated by  $\frac{\Delta E}{E} \cong \frac{M_1}{M_2} \theta^2$ , under the assumptions that the mass  $M_2$  of the target atoms is much larger than the mass  $M_1$  of the incident ion, and that the scatter angle  $\theta$  is small. For MeV He ions this contribution is negligibly small [4], and the main contribution to the energy loss originates from inelastic collisions with target electrons. In FLUX7, the ion-electron interaction is split into contributions of the strongly bound inner shell electrons (core electrons) and the loosely bound outer shell electrons (valence electrons). The contribution of the core electrons is a function of the impact parameter and is based on the energy loss model of Dettmann and Robinson [13]. The energy loss due to the valence electrons can be split again into collisions with small impact parameters (the local valence contribution), and interactions with distant electrons in the form of excitation of plasma oscillations. In FLUX7, both terms are described by the model of Melvin and Tombrello [14], assuming a uniform valence electron distribution throughout the target sample.

The stopping power calculated by these models does not sum up exactly to the empirically measured stopping. In order to compare calculated energy spectra with measured energy spectra, the FLUX7 program allows to normalize the calculated stopping to the empirical values published by Ziegler *et al.* [12]. The core electron contribution is not altered, but the valence electron contribution is scaled. The deviations in the valence contribution obtained in this way is typically about 10% compared to Melvin and Tombrello.

The FLUX7 program is able to calculate the difference in energy loss of channeled ions with different transverse energies in the channel. An important assumption in FLUX7 is that the valence and impact parameter dependent core electron contributions to the electronic energy loss are assumed to be independent of the ion energy along the calculated trajectory, based on the idea that the total energy loss over the range in which the ion trajectory is followed is usually relatively small. The energy loss distribution can not be

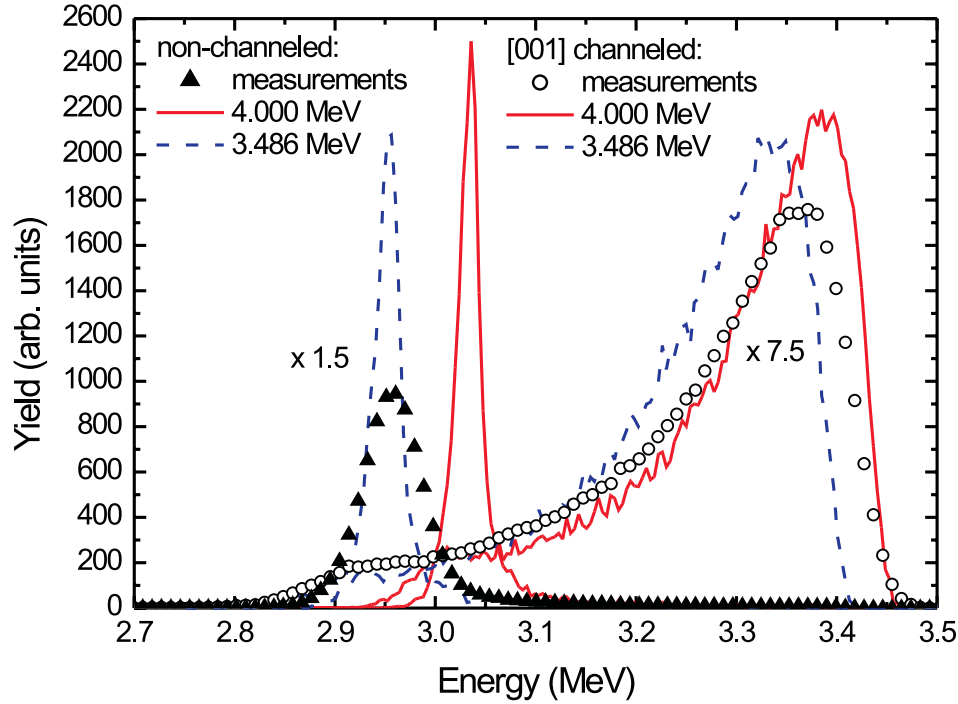


Figure 8.2: Calculated energy spectra (lines) assuming constant stopping values at He energies of 4.000 and 3.486 MeV together with the measured energy spectra (symbols), for the [001] channeling and a non-channeling direction. Note that the incident ion energy is 4 MeV for both cases.

calculated using a constant energy loss in the case of a  $5.7 \mu\text{m}$  thick sample. Introducing an energy dependence of the energy loss model in the FLUX7 calculations is however relatively straightforward.

One of the output parameters of the FLUX7 calculations, is an energy histogram of the transmitted ions. This option was used to calculate the energy distributions for  $5 \times 10^4$  He ions transmitted through a  $5.714 \mu\text{m}$  thick Si crystal with an incident energy of 4 MeV. In Fig. 8.2 the results are shown for calculations with 4 MeV He ions and constant stopping values at energies of 4.000 and 3.486 MeV together with the measured energy spectra, for the [001] channeled and a non-channeled direction. The energy of 3.486 MeV is the average energy according to the approximation used in equation (8.1). Since the electronic stopping decreases with increasing energy for MeV He ions in silicon, the calculations with stopping values at 4.000 MeV result in an underestimation of the total energy loss. For the calculations with constant stopping values at 3.486 MeV, the average transmitted energy for the non-channeled direction is  $2968 \pm 5 \text{ keV}$ , which corresponds to an energy loss of  $1032 \pm 5 \text{ keV}$ . This is in agreement with the approximation of equation (8.1), which predicts an energy loss of  $1028 \pm 2 \text{ keV}$ . As can be seen in Fig. 8.2 for a stopping at 3.486 MeV, the energy loss of the [001] channeled ions is overestimated in the calculations, since the average energy of the best channeled ions is about 3.68 instead of 3.486 MeV. The ratio of the channeled-to-non-channeled energy loss is 0.64 for both cases. A fixed energy is thus not applicable to obtain satisfactory resemblance between

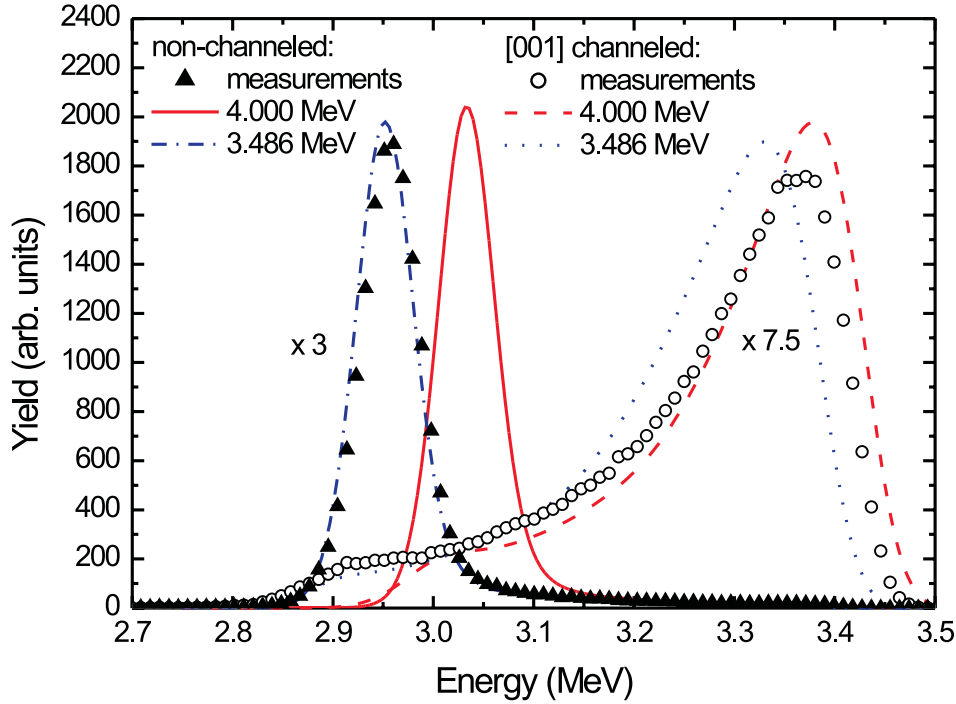


Figure 8.3: Calculated energy spectra from Fig. 8.2 convoluted with a Gaussian distribution with standard deviation  $\sigma = 24$  keV (lines), and the measured energy spectra (symbols).

simulated and measured transmitted energy loss distributions.

Furthermore, the shapes of the calculated non-channeled energy distributions significantly deviate from the measured energy spectrum: the width of the non-channeled peak is much wider in the measurements ( $\sim 70$  keV) than in the calculations ( $\sim 28$  keV). In the calculated energy distribution the width of the peak stems from the energy straggling, which can be estimated with the Bohr value of energy straggling [17]:

$$\Omega_B^2 = 4\pi Z_1^2 Z_2 e^4 N \Delta t, \quad (8.2)$$

which is independent of energy and where  $Z_1$  and  $Z_2$  are the atomic numbers of the incoming and target particle, respectively, and  $N \Delta t$  is the number of target atoms per unit area. This gives a contribution of about 20 keV FWHM, which is roughly in agreement with the width of the calculated non-channeled energy spectra. In the measurements, the detector resolution of about 22 keV contributes to the width of the peak, but this contribution is not large enough to account for the difference in peak width in the measured and calculated non-channeled energy spectra. The remaining contribution to the measured peak width most probably stems from variations in the thickness of the sample. Considering the contributions from the energy straggling and the detector resolution, the contribution from thickness variations can be accounted for by a Gaussian distribution with a FWHM of about 60 keV. If we compare this to the value of the energy loss ( $\pm 1030$  keV), the thickness variations are estimated to be about 3% over the area of the sample irradiated with the ion beam, which is estimated to be about  $0.25 \text{ mm}^2$ . In Fig. 8.3 the spectra of Fig. 8.2 have been convoluted with a Gaussian distribution with a standard



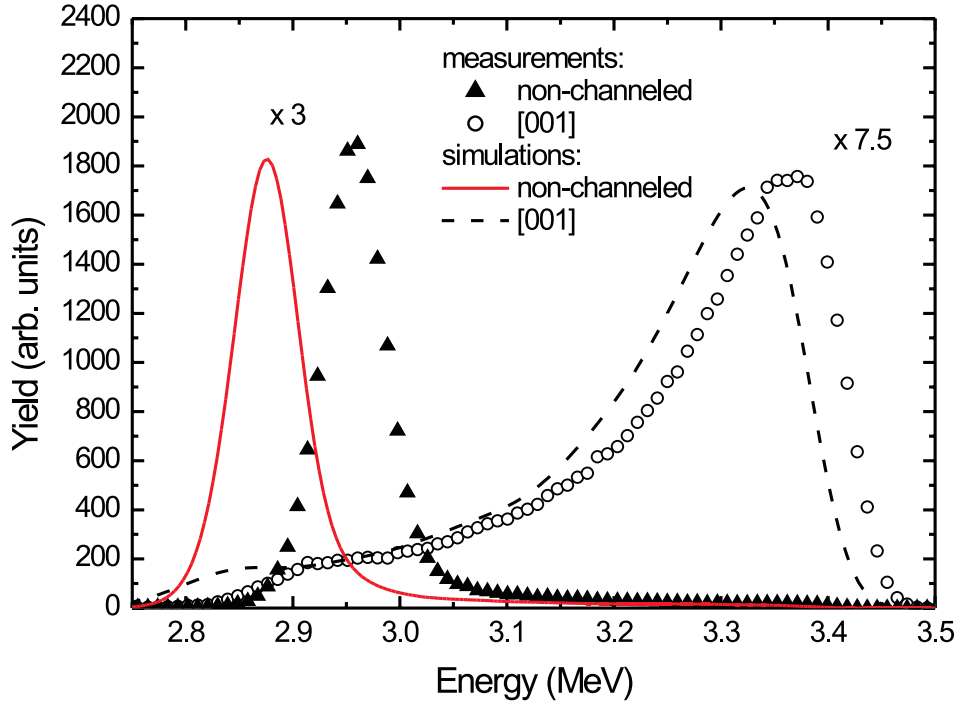


Figure 8.4: Calculated energy spectra (lines) assuming a  $1/E$  energy dependence of the electronic stopping power, for the [001] channeling and a non-channeling direction. The measured energy spectra are also shown (symbols).

deviation  $\sigma = 24$  keV, which corresponds to a FWHM of about 56 keV. The shapes of the calculated non-channelled energy spectra are now in good agreement with the shape of the measured non-channelled energy spectrum. In the remainder of this section, the calculated energy distributions, which are presented, have been convoluted with this same Gaussian distribution.

To obtain a better resemblance between the calculated and measured [001] channelled transmission energy distributions, energy dependent energy loss was incorporated in the FLUX7 calculations. The standard FLUX7 simulation code calculates the energy loss at each collision. The energy dependence of the stopping is incorporated by scaling the stopping values at 4 MeV with  $1/E$  at each collision. This implies that both the core and valence contributions to the stopping are scaled with  $1/E$ , which is a first order approximation of the models mentioned in literature [13,14]. The results of the convoluted energy distributions, calculated with this energy dependence in the stopping, are shown in Fig. 8.4 for the [001] channeling and a non-channeling direction, together with the measured energy spectra. Clearly, the non-channelled energy loss is overestimated in the calculations with a  $1/E$  dependency in the energy loss. Remarkably, the channelled to non-channelled energy loss ratios is  $0.60 \pm 0.01$ , which is in agreement with the measured ratio of  $0.61 \pm 0.01$ .

Another approach to incorporate an energy dependent energy loss of the ions along the trajectory, is the introduction of a large number of stopping values for different energies which occur along the path. The stopping values are calculated for each energy with

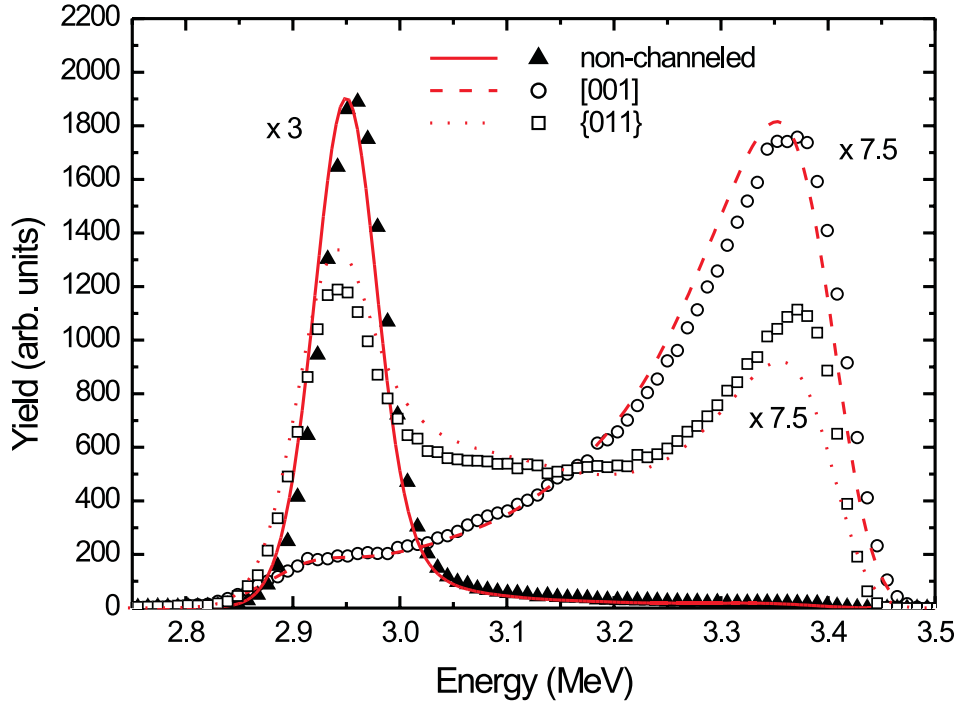


Figure 8.5: Calculated energy spectra (lines) for electronic stopping based on interpolation of stopping values for different energies, for the [001] axial channeling, the {011} planar channeling, and a non-channeling direction. The measured energy spectra are also shown (symbols).

the procedure using both core electrons through the model of Dettmann and Robinson, and the valence electrons through the model of Melvin and Tombrello scaled to empirical values as described earlier. The stopping is calculated from a linear interpolation of the stopping values for the energies in the input file nearest to the momentaneous energy of the ion, at each binary collision in the trajectory. We will refer to this energy dependence of the stopping as the interpolation-model. In the FLUX7 input file, stopping values were entered for He ions in a Si target at energies of 4.0, 3.9, 3.8 MeV, etc., decreasing with steps of 100 keV.

The convoluted energy distributions calculated with the interpolation-model are plotted in Fig. 8.5 for  $10^5$  He ions incident along the [001] axial, {001} planar channeled, and a non-channeled direction. The average energy of the ions transmitted in a non-channeling direction is  $2967 \pm 3$  keV. This implies that the average energy loss is  $1033 \pm 3$  keV, which is close to the measured energy loss of  $1028 \pm 2$  keV (deviation of 0.5%). The energies corresponding to the peak values of the channeled and non-channeled energy spectra are  $3353 \pm 5$  and  $2948 \pm 1$  keV, respectively, which results in a channeled-to-non-channeled energy-loss-ratio of  $0.62 \pm 0.01$ . These numbers are in good agreement with the experiments.

Furthermore, the shapes of the calculated energy distributions are in satisfactory agreement with the shapes of the measurements, except for the {011} planar channeling experiments for which the channeled fraction seems to be underestimated in the MC

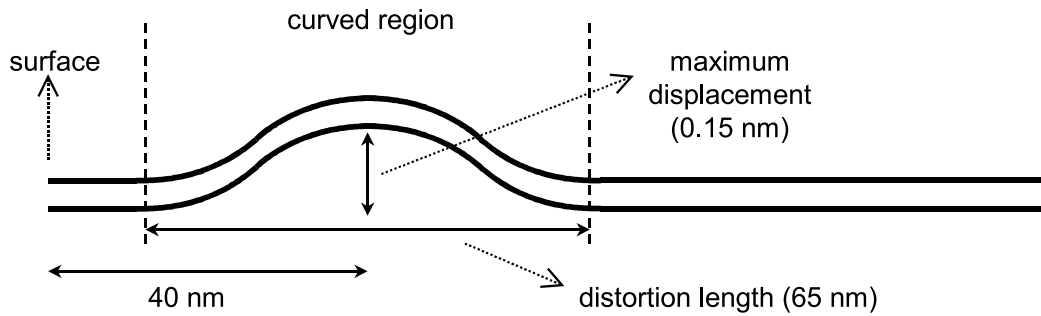


Figure 8.6: Deformation of the crystal lattice as used in the Monte Carlo calculations with the option curvature, to simulate the lattice distortions induced by the presence of clusters. The distortion length and maximum displacement are indicated, and the centre of the curved crystal structure is situated at a depth of 40 nm in the crystal.

simulations. Planar channeling simulations have proven to be sensitive to the ion-atom potential incorporated [18], and it might be emphasized that the number of particles that initially become channeled are underestimated or that the amount of initially channeled ions that become dechanneled along the trajectory are overestimated by the universal potential.

The energies corresponding to the peaks in the calculated energy spectra are only in satisfactory agreement with those from the measured spectra for simulations with the electronic stopping calculated from linear interpolation between stopping values based on the Ziegler values at nearby energies. Furthermore, only for the interpolation-model the overall shapes of the energy spectra are in satisfactory agreement with the measured spectra.

## IV Transmission channeling and clusters

The presence of defects in a crystal can lead to enhanced direct scattering and dechanneling compared to a perfect crystal. Enhanced dechanneling can arise from displaced atoms and extended defects such as strain fields, and the increase of the non-channeled fraction of the beam in the crystal potentially leads to a change in the energy distribution in transmission channeling experiments.

As was already mentioned, the fabrication of sharp, ultra-shallow profiles with high concentrations of electrically active B by ion implantation is not straightforward due to amongst others the formation of electrically inactive B clusters. In previous work, we showed that the presence of B clusters in silicon leads to strain fields in the implanted Si, which give rise to 3-dimensional lattice distortions around each B cluster [19]. The dimensions of the lattice distortions could be successfully characterized by comparison of RBS channeling measurements on a Si crystal containing B clusters with Monte Carlo channeling simulations on a curved crystal lattice structure.

In this work we will use the same curved crystal structure to simulate the presence of B clusters, and investigate whether transmission experiments provide an alternative approach to detect cluster formation. Figure 8.6 shows the deformation of the Si lat-

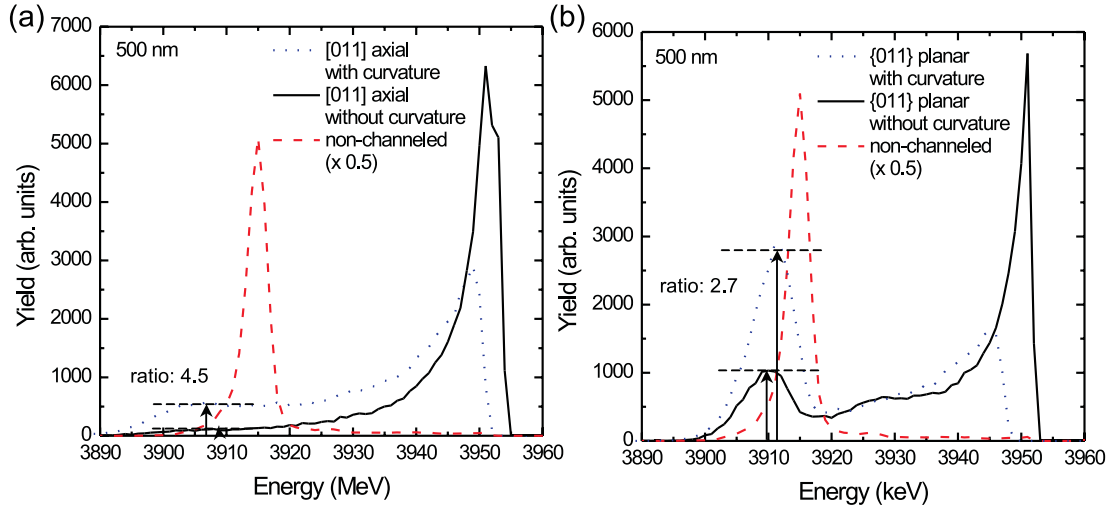


Figure 8.7: Calculated [001] axial channeled (a),  $\{011\}$  planar channeled (b), and non-channeled transmitted energy distributions (a-b) for samples with a total thickness of 500 nm. Simulations were performed on a virgin crystal and a crystal with a curvature to simulate the presence of clusters. The arrows indicate the maximum yield in the high-energy-loss parts of the energy spectra, and the ratio between the values for the curved and virgin crystal is indicated.

tice as used in the calculations; the channeled ions have to go through a double chicane in the channel to simulate the lattice deformations around a B cluster. To imitate the 3-dimensionality of the lattice deformation around a B cluster, the direction of the curvature specified by  $\phi$  is randomly assigned at the beginning of the calculation of each ion trajectory.

In the calculations presented in this section, the distortion length and the maximum displacement are taken 65 and 0.15 nm, respectively (indicated in Fig. 8.6). The calculated values for the enhanced direct scattering and scattering yield due to dechanneling induced by a curved lattice structure with these parameters, are comparable to the measured enhanced direct scattering and scattering yield due to dechanneling for a silicon sample implanted with  $3 \times 10^{15}$  B/cm<sup>2</sup> at an implantation energy of  $\sim 10$  keV per B atom. The implantation was performed with decaborane ( $B_{10}H_{14}^+$ ) ions at an energy of 120 keV, which corresponds to  $\sim 10$  keV per B-atom [1]. After a rapid thermal anneal in dry nitrogen applied at a temperature of 1050°, the implanted sample exhibits an estimated number of  $1.6 \times 10^{15}$  B clusters/cm<sup>2</sup> in a depth interval of 26-54 nm. The center of the curved crystal is positioned at a depth of 40 nm in the simulations, corresponding to the middle of this region with clusters. The enhanced dechanneling, which is of our interest here, is typically about 13% at a depth of 200 nm in the sample, for RBS channeling measurements with 2-3.5 MeV He ions [19].

Simulations were performed on samples with a total thickness of 500 and 5000 nm. Figures 8.7 and 8.8 show the results for [001] axial and  $\{011\}$  planar transmission channeling simulations on samples with a curvature. The calculated energy spectra of a virgin crystal for the [001] axial, the  $\{011\}$  planar, and a non-channeling direction are added

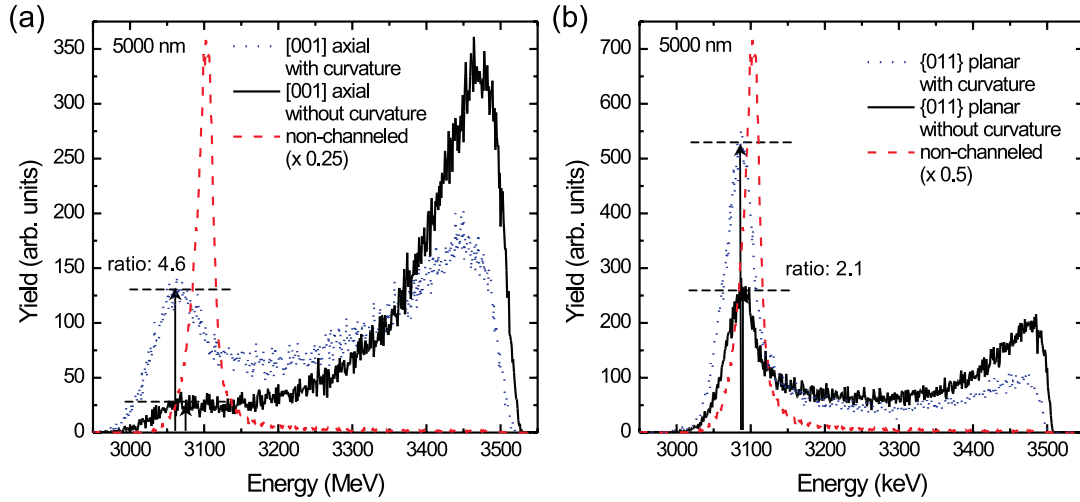


Figure 8.8: Same as Fig. 8.7, but for a sample with a total thickness of 5000 nm (c-d).

for a comparison. The presence of the curvature in the simulated crystal clearly affects the transmitted energy distributions, which have a large non-channeling component compared to the [001] axial and {011} planar channeled energy distributions of the virgin crystal. The arrows with dashed lines in Fig. 8.7 and 8.8 indicate the maximum yield in the high-energy-loss parts of the channeled energy distributions. The ratios of these maximum yields of the curved and virgin crystal are indicated, and is on average about 4.6 and 2.4 for the [001] axial and {011} planar channeled energy distributions, respectively. Note, that when the energy resolution of the detection system is taken into account, many details in the energy spectra of the 500 nm thick sample are lost. This is illustrated in Fig. 8.9, where the calculations of Fig. 8.7 have been convoluted with a Gaussian distribution with a standard deviation  $\sigma = 9$  keV to simulate a detector resolution of 22 keV FWHM. Furthermore, it can be seen in Fig. 8.7 and 8.8 that the best channeled ions in the curved crystals have lost more energy than those in the virgin crystals. The calculated spectrum of the curved crystal can thus clearly be distinguished from a virgin sample, and energy loss distributions in transmission channeling experiments can be a valuable tool in addition to channeling RBS to measure the onset of cluster formation in silicon.

## V Conclusions

A thin etched silicon wafer with a thickness of  $5.7 \pm 0.2 \mu\text{m}$  is studied with transmission ion-channeling to investigate the treatment of energy loss in the Monte Carlo channeling simulation code FLUX7. Appropriate handling of the energy loss in MC calculations is necessary to be able to reproduce and understand the shape of measured transmission channeling energy distributions. It appears that only a model based on the interpolation between stopping power values from Ziegler results in a satisfactory resemblance between calculated and measured transmission energy loss distributions.

The presence of precipitates or clusters in a semiconductor film, will induce lattice deformations, and consequently, part of the channeled fraction of the ion beam will dechan-

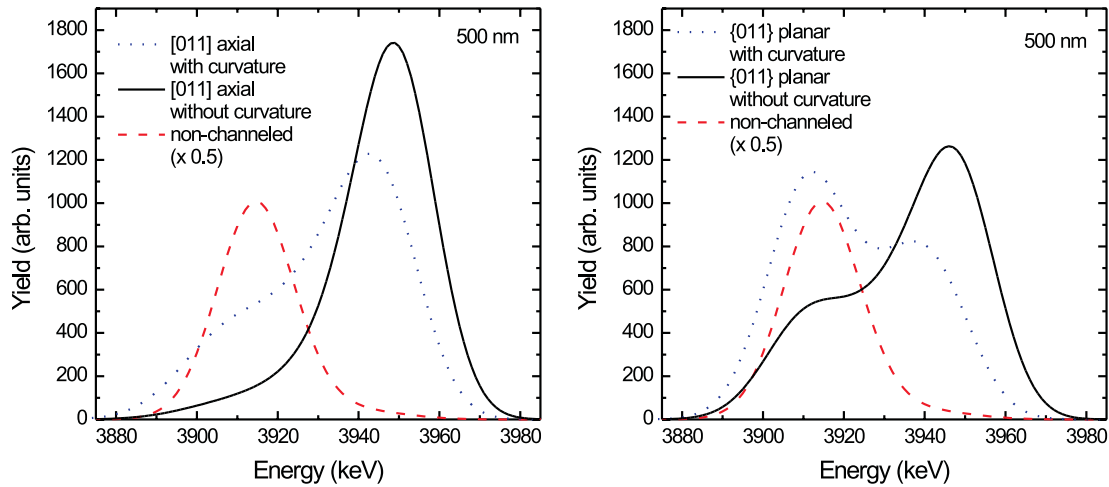


Figure 8.9: Calculated spectra from Fig. 8.7 convoluted with a Gaussian distribution with standard deviation  $\sigma = 9$  keV to simulate a detector resolution of 22 keV FWHM.

nel, which leads to a higher average energy loss of the transmitted ions. The feasibility to detect cluster induced lattice distortions in transmission channeling experiments is studied with MC calculations on a curved crystal. The dimensions of the curvature are chosen such that the enhanced direct scattering and dechanneling in the curved crystal are comparable to those for a crystal with B clusters, originating from implantation above the solid solubility. The presence of the curvature in the crystal clearly influences the calculated transmitted energy distribution, and transmission ion-channeling therefore seems to offer a way to determine the presence of light element dopant clusters in a host crystal. At the moment however, the methods to produce silicon transmission channeling samples are not appropriate for investigating lattice deformations. The authors therefore would like to emphasize the development of an alternative method for thinning silicon samples, which does not change the intrinsic sample properties.

## References

[\*] Author to whom correspondence should be addressed. FAX: +31 40 243 80 60. Present address: Cyclotron Laboratory, Department of Applied Physics, Eindhoven University of Technology, P.O. Box 513, 5600 MB Eindhoven, The Netherlands. Electronic address: L.J.van.IJzendoorn@tue.nl.

- [1] A. G. Dirks, P. H. L. Bancken, J. Politiek, N. E. B. Cowern, J. H. M. Snijders, J. G. M. van Berkum, and M. A. Verheijen, *IIT conference proceedings*, Kyoto (1998).
- [2] A. Agarwal, H.-J. Gossmann, D. C. Jacobson, D. J. Eaglesham, M. Sosnowski, J. M. Poate, I. Yamada, J. Matsuo, and T. E. Haynes, *Appl. Phys. Lett.* **73**, 2015 (1998).
- [3] L. C. Feldman, J. W. Mayer, and S. T. Picraux, *Materials Analysis by Ion Channeling* (Academic Press, New York, 1982).

- [4] J. F. Ziegler, J. P. Biersack, and U. Littmark, *The Stopping and Range of Ions in Solids* (Pergamon Press, New York, 1985).
- [5] H. H. Andersen, J. F. Bak, H. Knudsen, and B. R. Nielsen, *Phys. Rev. A* **16**, 1929 (1977).
- [6] A. L'Hoir and D. Schmaus, *Nucl. Instr. and Meth. B* **4**, 1 (1984).
- [7] M. B. H. Breese, P. J. C. King, J. Whitehurst, G. R. Booker, G. W. Grime, F. Watt, L. T. Romano, and E. H. C. Parker, *J. Appl. Phys.* **73**, 2640 (1993).
- [8] P. J. C. King, M. B. H. Breese, P. R. Wilshaw, and G. W. Grime, *Phys. Rev. B* **51**, 2732 (1995).
- [9] F. H. Eisen, G. J. Clark, J. Bottiger, and J. M. Poate, *Radiat. Eff.* **13**, 93 (1972).
- [10] P. W. L. Van Dijk, Ph.D. thesis, Eindhoven University of Technology, 1997.
- [11] N. W. Cheung, *Rev. Sci. Instrum.* **51**, 1212 (1980).
- [12] P. J. M. Smulders and D. O. Boerma, *Nucl. Instrum. and Meth. B* **29**, 471 (1987).
- [13] K. Dettmann and M. T. Robinson, *Phys. Rev. B* **10**, 1 (1974).
- [14] J. D. Melvin and T. A. Tombrello, *Radiat. Eff.* **26**, 113 (1975).
- [15] T. J. Lenosky, B. Sadigh, S. K. Theiss, M. Caturla, and T. D. de la Rubia, *Appl. Phys. Lett.* **77**, 1834 (2000).
- [16] T. Wang, A. G. Cullis, E. J. H. Collart, A. J. Murrell, and M. A. Foad, *Appl. Phys. Lett.* **77**, 3586 (2000).
- [17] N. Bohr, *Mat. Fys. Medd. Dan. Vid. Selsk* **8** (1948).
- [18] L. J. M. Selen, P. J. M. Smulders, L. J. van IJzendoorn, and M. J. A. de Voigt, chapter 4 of this thesis (unpublished).
- [19] L. J. M. Selen, L. J. van IJzendoorn, A. van Loon, and M. J. A. de Voigt, chapter 7 of this thesis (unpublished).

# Summary

MeV ion-channeling combined with Rutherford backscattering spectrometry (RBS) is a well-known technique to investigate lattice deformations in (buried) strained crystalline films. By measuring angular scans, the change in direction of crystal axes and planes can be determined, which is a measure for the strain in the crystal. This method is however not applicable when the thickness of the investigated film becomes below typically 20 nm, or when the deformations have a 3-dimensional character.

The size and dimensionality of state of the art semiconductor structures continuously decreases due to the demand for faster devices and developments in growth and ion implantation techniques. Examples of small and low-dimensional semiconductor structures are quantum dots, strained films with a thickness of only a few nanometers, and ultra-shallow junctions. As a common element, all these semiconductor structures exhibit strain induced lattice deformations.

Characterization of these state of the art semiconductor devices therefore asks for innovative methods or applications of ion-channeling. In this thesis, these novel methods and applications are introduced on quantum dots (chapter 2), strained buried thin films (chapters 3-6), and Si samples exhibiting dopant clusters after B implantation (chapters 7-8). Furthermore, this thesis shows that Monte Carlo channeling calculations are very essential to obtain quantitative information from the ion-channeling measurements.

InAs quantum dots in a GaAs matrix are expected to be strained in order to explain their optical properties. This is investigated in chapter 2 by measuring angular scans of the InAs quantum dots and the surrounding GaAs matrix. The observed channeling behaviour in the angular scans implies the absence of dislocations and a gradual transition from the cubic GaAs lattice to the strained InAs lattice in the quantum dots. This means that extended strain fields are present in the GaAs matrix around the InAs quantum dots. These strain fields induce a steering of the channeled ions from the GaAs channels into the InAs channels, which explains the observed channeling behaviour. The ion-channeling measurements in chapter 2 therefore establish the presence of strain fields in and around the InAs quantum dots.

Characterization of the tetragonal distortion in a buried strained film with a thickness of only a few nanometer demands an innovative methodology. The key to this method relates to the translation of the off-normal atomic strings and planes of the host crystal across the strained film. This is demonstrated in chapter 3, where the tetragonal distortion of 2.2 nm thick strained buried  $\text{Si}_{1-x}\text{Ge}_x$  films is determined from axial ion-channeling measurements along the [011] direction. The translation of the atomic strings and planes of the host crystal is induced by a kink in the directions of the axes and planes at the interfaces of the  $\text{Si}_{1-x}\text{Ge}_x$  nano-film and the surrounding Si crystal, and leads to a step in a channeled RBS spectrum. The step height depends on the magnitude of the translation and the incident angle of the ion beam. With Monte Carlo simulations the angular



dependence of the step height in the channeled spectra can be related to the magnitude of the translation, and therefore to the tetragonal deformation in the  $\text{Si}_{1-x}\text{Ge}_x$  nano-film. The magnitude of the translation, and thus the tetragonal distortion, can be determined with an accuracy better than 10%, and it is shown that this is comparable to the accuracy obtained with high resolution X-ray diffraction measurements.

In chapter 4 the same method is applied in combination with planar channeling. For planar channeling on the same buried  $\text{Si}_{1-x}\text{Ge}_x$  nano-films from chapter 3, a higher step occurs in the channeled RBS spectra. Furthermore, the channeled flux distribution is still oscillating at the depth of the buried  $\text{Si}_{1-x}\text{Ge}_x$  nano-films, which can be concluded from the highly asymmetric measured step height curves. Monte Carlo simulations of these planar channeling measurements appear to be very sensitive to the ion-atom potential, which determines the wave-length of the oscillating trajectories of the channeled ions. It is shown that only with a Hartree-Fock potential incorporated, the simulated step height curves resemble the measured step height curves satisfactorily.

With this Hartree-Fock potential incorporated, planar channeling measurements can also be used to determine the tetragonal distortion in buried nano-films. This is demonstrated in chapter 5 for the buried  $\text{Si}_{1-x}\text{Ge}_x$  nano-films, which are also used in chapters 3 and 4. It can be concluded that due to the non-equilibrium distribution of channeled ions between the planes, the tetragonal distortion can not be determined more accurately than with axial channeling measurements, in spite of the higher steps in planar channeling measurements.

In chapter 6 the tetragonal distortion is determined for separate InAs nano-films in a sample with a stack of InAs monolayers in a GaAs matrix. It appears that the angular dependence of the step height curve is determined by the separate contributions from the individual InAs films, although the contributions of the separate InAs layers to the step in a channeled RBS spectrum can not be resolved. From axial channeling measurements and Monte Carlo simulations the translation of the GaAs [011] lattice strings across each InAs layer can be determined with an accuracy of 0.004 nm, which is almost twice as good as that for the experiments and simulations on a single  $\text{Si}_{1-x}\text{Ge}_x$  nano-film (chapters 3 and 5), which is about 0.006 nm.

Another interesting subject investigated with ion-channeling, is the undesired formation of dopant clusters due to implantation above the solid solubility, which is the subject of chapter 7. The effect of the lattice distortions in silicon induced by the presence of boron clusters, is readily observed in a channeled RBS spectrum as an increase in the direct scattering yield and an increase in the yield due to enhanced dechanneling. The average dimensions of these lattice distortions are estimated by comparing these increased yields with those obtained from Monte Carlo simulations on a curved crystal structure. Comparison at 2 different energies of the incident  $\text{He}^+$  beam shows that the length of the lattice distortions is typically about 65 nm, and that the maximum displacement of the perturbed crystal channels is  $0.17 \pm 0.01$  nm during the passage of the region with clusters. These are realistic values for the lattice distortions in a strain field, which shows that Monte Carlo calculations are an interesting auxiliary tool for the characterization of crystal distortions around clusters.

Finally, in chapter 8 a feasibility study is performed on the possibility of detecting dopant clusters with transmission ion-channeling. The presence of clusters induces lattice

distortions, which lead to enhanced dechanneling, which in turn leads to a different shape of the energy loss distribution of the transmitted ions. To obtain information about the dimensions of the lattice distortions, Monte Carlo calculations are needed which appropriately handle the stopping of the transmitted ions. Therefore, the well-known channeling simulation code FLUX7 is modified by introducing energy dependence in the electronic stopping power, after which the measured transmission energy distributions can be reproduced satisfactorily. With the extended simulation code, transmission energy spectra are calculated for crystals containing a curvature, which have channeling characteristics comparable to those of crystals with a region containing dopant clusters. The presence of the curvature in the crystal clearly influences the calculated transmitted energy distribution, and transmission ion-channeling therefore offers a way to determine the presence of dopant clusters in a host crystal.

# Samenvatting

Channeling in combinatie met Rutherford backscattering spectrometry (RBS) is een bekende techniek om roostervormingen in (begraven) dunne films te onderzoeken. Door het meten van de hoekafhankelijke verstrooiing kan de afwijking in de richting van kristalassen of -vlakken bepaald worden, waarmee roosterdeformaties kunnen worden vastgesteld. Deze methode is echter niet bruikbaar wanneer de dikte van de vervormde lagen minder is dan 20 nm of wanneer de vervormingen een 3-dimensionaal karakter hebben.

Door de vraag naar steeds snellere halfgeleidercomponenten en verdergaande ontwikkelingen van 'groei'- en implantatietechnieken, nemen de afmetingen van 'state-of-the-art' halfgeleiderstructuren en het aantal dimensies waarbinnen de ladingsdragers vrij kunnen bewegen steeds verder af. Voorbeelden van dit soort halfgeleiderstructuren zijn quantumdoosjes, vervormde lagen met een dikte van slechts enkele nanometers, en zeer ondiepe  $pn$ -overgangen. Al deze halfgeleiderstructuren hebben een gemeenschappelijk element, te weten roostervormingen ten gevolge van mechanische spanningen in het kristalrooster.

Om deze 'state-of-the-art' halfgeleidercomponenten te kunnen karakteriseren zijn vernieuwende channeling methoden noodzakelijk. In dit proefschrift worden die toegepast op quantumdoosjes (hoofdstuk 2), vervormde begraven dunne lagen (hoofdstukken 3 t/m 6) en Si preparaten die borium (B) clusters bevatten na B-implantatie (hoofdstukken 7 en 8). Monte Carlo berekeningen spelen een belangrijke rol en zijn essentieel om kwantitatieve informatie te verkrijgen uit de metingen.

De optische eigenschappen van InAs quantumdoosjes in een GaAs matrix doen vermoeden dat het kristalrooster van deze quantumdoosjes vervormd is. Dit is verder onderzocht in hoofdstuk 2 door de hoekafhankelijke opbrengst te meten van zowel de quantumdoosjes als de GaAs matrix. Uit de verstrooiingsopbrengst kan worden opgemaakt dat er geen dislocaties in het kristalrooster aanwezig zijn en dat er een geleidelijke overgang plaatsvindt van het kubische GaAs kristalrooster naar het vervormde InAs kristalrooster in de quantumdoosjes. Dit houdt in dat er uitgestrekte spanningsvelden aanwezig zijn in de GaAs matrix rondom de quantumdoosjes, die er voor zorgen dat de ionen van de GaAs kanalen in de InAs kanalen worden gestuurd. De channeling metingen in hoofdstuk 2 tonen daarmee de aanwezigheid van uitgestrekte spanningsvelden aan in en rondom de InAs quantumdoosjes.

In hoofdstuk 3 is een innovatieve methode bedacht om met axiale channeling de tetragonale vervorming te kunnen meten in een vervormde  $\text{Si}_{1-x}\text{Ge}_x$  film met een dikte van slechts 2.2 nm. De methode is gebaseerd op de verschuiving van de kristalassen en kristalvlakken voor richtingen niet parallel aan de normaal van het oppervlak. De verschuiving is het gevolg van een knik in de richtingen van de kristalassen en -vlakken bij de overgangen tussen de nano-film en het omringende rooster, en leidt tot een stap in het RBS spectrum. De hoogte van de stap hangt af van de grootte van de verschuiving en

van de inkomende hoek van de ionenbundel met de kristalassen. De hoekafhankelijkheid van de staphoogte in de spectra kan met Monte Carlo berekeningen gekoppeld worden aan de grootte van de verschuiving en dus ook aan de tetragonale vervorming in de  $\text{Si}_{1-x}\text{Ge}_x$  film. De grootte van de verschuiving, en daarmee ook de tetragonale vervorming, kan bepaald worden met een nauwkeurigheid van 10%. Dit is vergelijkbaar met de nauwkeurigheid die bereikt wordt met hoge-resolutie röntgendiffractie.

Dezelfde methode wordt ook toegepast in combinatie met channeling in kristalvlakken in hoofdstuk 4. Dezelfde  $\text{Si}_{1-x}\text{Ge}_x$  films zijn gebruikt als in hoofdstuk 3 en het blijkt dat de stap in de RBS spectra groter is voor channeling in vlakken. Ook kan uit de asymmetrische stap-hoogte-curves geconcludeerd worden, dat de flux verdeling van ionen in het vlak nog oscilleert in het sample op de diepte van de  $\text{Si}_{1-x}\text{Ge}_x$  nano-film. Monte Carlo simulaties van deze metingen blijken zeer gevoelig te zijn voor de ion-atoom potentiaal, die de golflengte van de oscillerende deeltjesbanen bepaalt. Er wordt aangetoond dat de gesimuleerde stap-hoogte-curves alleen met een Hartree-Fock potentiaal voldoende gelijkenis vertonen met de gemeten curves.

Met deze Hartree-Fock potentiaal in de simulaties, kan ook channeling in vlakken gebruikt worden om de tetragonale vervorming in begraven nano-films te bepalen, zoals beschreven in hoofdstuk 5. Ondanks dat de stap in het RBS spectrum groter is voor channeling in vlakken, kan de tetragonale vervorming niet nauwkeuriger bepaald worden dan met axiale channeling. Dit is het gevolg van de nog oscillerende flux verdeling van ionen tussen de kristalvlakken.

In hoofdstuk 6 wordt de methode gebruikt om de tetragonale vervorming van individuele InAs nano-films te bepalen in een sample dat tien gestapelde InAs monolagen in een GaAs matrix bevat. Het blijkt dat de hoekafhankelijkheid van de stap-hoogte-curve wordt bepaald door de afzonderlijke bijdragen van de individuele InAs films, ook al kunnen de bijdragen van de afzonderlijke InAs laagjes niet van elkaar opgelost worden in het RBS spectrum. Met axiale channeling metingen en Monte Carlo simulaties kan de verschuiving van de GaAs [011] kristalassen met een nauwkeurigheid van 0.004 nm bepaald worden, terwijl de breedte van een kanaal typisch enkele nm is. Daarmee zijn deze metingen bijna twee keer zo nauwkeurig als de metingen aan een enkelvoudige  $\text{Si}_{1-x}\text{Ge}_x$  nano-film (hoofdstuk 3), die een nauwkeurigheid van 0.006 nm halen.

Een ander interessant onderwerp, is de ongewenste vorming van clusters van doteringen die ontstaan na implantatie met een hoge dosis. Dit wordt onderzocht in hoofdstuk 7. Het effect van roostervervormingen ten gevolge van borium (B) clusters in Si is duidelijk zichtbaar als een toename van de verstrooiingsopbrengst in het RBS spectrum. De ionen worden uit het kanaal gestuurd door directe verstrooiing aan defecten en door vervorming van de kanalen in de nabijheid van een cluster. De gemiddelde afmetingen van de roostervervormingen zijn afgeschat door de verhoogde verstrooiingsopbrengst te vergelijken met die uit Monte Carlo berekeningen aan een gebogen kristalstructuur. Vergelijking van de resultaten bij twee verschillende energieën van de inkomende  $\text{He}^+$  bundel laat zien dat de lengte van de roostervervormingen typisch ongeveer 65 nm is en dat de maximale afwijking van de vervormde kristalassen  $0.17 \pm 0.01$  nm is bij het doorlopen van een gebied met clusters. Dit zijn realistische waarden voor de afmetingen van roostervervormingen in een spanningsveld. Daarmee wordt aangetoond dat Monte Carlo simulaties een interessant hulpmiddel kunnen zijn voor de karakterisering van kristalroostervervormingen rondom

clusters.

In hoofdstuk 8 is er tenslotte een haalbaarheidsstudie gedaan naar de mogelijkheid om clusters van doteringen op te sporen met transmissie channeling. De aanwezigheid van clusters veroorzaakt roostervormingen, waardoor ionen uit de kanalen kunnen worden gestuurd, wat weer leidt tot een verandering van de vorm van de energieverdeling van de ionen die door het preparaat heen zijn gegaan. Om informatie te verkrijgen omtrent de afmetingen van de roostervormingen zijn Monte Carlo simulaties nodig die de afremming van ionen in de kanalen op de goede manier meenemen tijdens de berekeningen van de deeltjesbanen. Daarvoor is de bekende simulatiecode FLUX uitgebreid met de energie-afhankelijkheid van de afremming door elektronen, waarna gemeten energieverdelingen voldoende nauwkeurig gereproduceerd kunnen worden. Met de simulatiecode zijn energieverdelingen in transmissie berekend voor gebogen kristalstructuren die corresponderen met kristallen waarin clusters van doteringen aanwezig zijn. De buiging van het kristal heeft een duidelijke invloed op de berekende energieverdeling, wat betekent dat transmissie channeling inderdaad gebruikt zou kunnen worden om clusters van doteringen op te sporen in een kristal.

# List of publications

## **Evidence for strain in and around InAs quantum dots in GaAs from ion-channeling experiments**

L. J. M. Selen, L. J. van IJzendoorn, P. M. Koenraad, and M. J. A. de Voigt, Phys. Rev. B **61**, 8270 (2000)

## **Strain measurements in ultra-thin buried films ( $<50 \text{ \AA}$ ) with RBS ion channeling**

L. J. M. Selen, F. J. J. Janssen, L. J. van IJzendoorn, M. J. J. Theunissen, P. J. M. Smulders, and M. J. A. de Voigt, Nucl. Instrum. and Meth. B **161-163**, 492 (2000)

## **Ion-channeling for strain analysis in buried nano-films ( $< 6 \text{ nm}$ )**

L. J. M. Selen, F. J. J. Janssen, L. J. van IJzendoorn, M. J. J. Theunissen, P. J. M. Smulders, T. J. Eijkemans, and M. J. A. de Voigt, submitted for publication in J. Appl. Phys.

## **Planar ion-channeling on buried nano-films discriminates between ion-atom potentials**

L. J. M. Selen, L. J. van IJzendoorn, P. J. M. Smulders, and M. J. A. de Voigt, submitted for publication in Phys. Rev. Lett.

## **Planar ion-channeling measurements on buried nano-films**

L. J. M. Selen, F. J. J. Janssen, L. J. van IJzendoorn, P. J. M. Smulders, M. J. J. Theunissen, and M. J. A. de Voigt, submitted for publication in Nucl. Instrum. and Meth. B

## **Lattice deformation in InAs/GaAs superlattices characterized by MeV ion-channeling**

L. J. M. Selen, L. J. van IJzendoorn, F. J. J. Janssen, P. J. M. Smulders, and M. J. A. de Voigt, submitted for publication in Phys. Rev. B

## **A channeling study of boron clusters in silicon**

L. J. M. Selen, L. J. van IJzendoorn, A. van Loon, and M. J. A. de Voigt, submitted for publication in J. Appl. Phys.

## **Transmitted ion energy loss distributions to detect cluster formation in silicon**

L. J. M. Selen, A. van Loon, L. J. van IJzendoorn, and M. J. A. de Voigt, submitted for publication in Nucl. Instrum. and Meth. B

# Dankwoord

Op de kaft van dit proefschrift staat slechts één naam, die van mij, maar om mijn promotie-onderzoek tot een goed einde te brengen, hebben nogal wat mensen een bijdrage moeten leveren. Mijn dank voor die personen wil ik hier in enkele woorden proberen samen te vatten.

Als eerste wil ik mijn copromotor Leo van IJzendoorn bedanken, omdat hij het meest geholpen heeft bij het tot stand komen van dit proefschrift. Leo, door je nimmer tanende enthousiasme en altijd positieve kritiek, heeft iedereen die dit nu leest een prima stuk werk in handen. Bedankt, en ik hoop dat je nog veel tijd in onderzoek mag stoppen als de nieuwe versneller er eenmaal staat.

Ook aan mijn 1<sup>e</sup> promotor Martien de Voigt ben ik veel dank verschuldigd. Martien, met jouw niet geringe overredingskracht heb je een grote bijdrage gehad in mijn keuze voor een promotie-plaats in het Cyclotron-gebouw. Mijn dank daarvoor, want in jouw groep heb ik 4 jaar lang in een prettige en inspirerende omgeving gewerkt en van veel vrijheid mogen genieten, en dat was precies wat ik zocht. Tenslotte wil ik je nog bedanken voor je gulle sponsoringen aan de Faculty Pub!

Een andere belangrijke bijdrage aan dit werk is geleverd door Peter Smulders. Hij is de geestelijke vader van de simulatie-code FLUX, die een essentieel onderdeel van mijn promotie-onderzoek is gebleken. Ook hebben de meeste hoofdstukken de test van zijn behoorlijk kritische oog ondergaan, waarvoor ik hem zeer erkentelijk ben. Peter, bedankt, ook jouw bijdrage is heel erg belangrijk geweest.

Mijn 2<sup>e</sup> promotor prof. Joachim Wolter wil ik bedanken voor het leesbaarder maken van mijn proefschrift voor niet-ionenbundelanalysemannen en -vrouwen. Verder heb ik veel samengewerkt met mensen uit zijn groep, te weten Paul Koenraad, die mij een eerste sample wist te regelen om aan te meten, Maarten Leijs, die mij wist uit te leggen wat voor een sample het nou eigenlijk was, en Tom Eijkemans, met wiens hulp ik de XRD-metingen van hoofdstuk 3 heb gedaan.

Ook heb ik het niet slecht getroffen met 'mijn' afstudeerders Frank Janssen en Arjan van Loon en 'mijn' enige stagiair Jim Heirbaut. Frank is gewoon altijd goed bezig (behalve als hij aan het schieten is misschien). Daardoor heeft hij een groot aandeel gehad in meerdere hoofdstukken van dit proefschrift en is nu zelf intussen aan het promoveren. Het etsen van Si door/met Jim is nooit helemaal lekker uit de verf gekomen, maar de ideeën die tijdens zijn stage naar boven zijn gekomen hebben wel de basis gelegd voor de laatste hoofdstukken in dit werk. Arjan heeft uiteindelijk meegeholpen met het uitwerken van die ideeën, wat heeft geleid tot de laatste 2 hoofdstukken. Ik ben trouwens benieuwd wie van ons er het eerste klaar is uiteindelijk...

Om alle metingen en simulaties te kunnen uitvoeren is een goed functioneren van alle hard- en software een vereiste. Dat het Cyclotron meestal naar behoren draaide en dat

de channeling-opstelling dan tegelijkertijd ook nog werkte is te danken aan mannen als Rinus Queens ('Je moet gewoon niet met  $\alpha$ 's meten, jongen!'), Frits van Hirtum, Jan van den Berg, Eric van den Eerden, Leo de Folter, Henk Heller (wereldkampioen opstellingen uit elkaar draaien), Huib Schouten, Harry van Doorn en Ad en Wim Kemper. Vooral ook die andere wlm ben ik veel dank verschuldigd voor zijn hulp bij het draaiende krijgen van FLUX, wat geschreven is voor een operating systeem uit de jaren '80, maar nu dus ook draait op eentje uit de jaren '70! Verder heeft Peter Mutsaers zo af en toe een beetje moeten toveren met de inhoud van PhyDAS rekken (vooral de verdwijntruck ben ik een paar keer tegen gekomen).

De sfeer is met name op onze AIO-kamer de afgelopen 4 jaar fantastisch geweest, vooral door de gulle bijdragen daaraan van Addo Hammen (je hebt de goede keus gemaakt, Hammen), Michel de Jong (de VS was een goede reis, ja!) en Fred Kiewiet (ons eerste 'Big-Dick-Team'-lid dat papa is). Al die andere (oud-)collega's hebben ook bijgedragen aan een leuke tijd en wil ik zonder namen te noemen danken daarvoor. Mede door de inspanningen van Annette Eliëns leeft verder de Faculty Pub gelukkig weer, wat een keer per maand een gezellige vrijdagmiddag oplevert. Ook de donderdagmiddag uurtjes met (alweer) Addo en Michel, Erwin van der Werf, Ad Wellens, Leo de Folter, Frits van Hirtum (mag nog maar af en toe komen) en Henk Heller (mag nog maar 1 keer per jaar komen) zijn altijd vlotjes voorbij gegaan.

Natuurlijk is een goede avondmaaltijd en zo af en toe een feestje tussendoor ook vrij belangrijk om de moraal hoog te houden. In Sjef 'DJ Pils' Tempelaars heb ik daarom de perfecte huisgenoot gehad, zodat de Schoolstraat 13 ondertussen wijd en zijd bekend staat als een van de beste feesttempels ten noorden van het station.

Ook Igor Martin verdient dank. Hij heeft me de afgelopen jaren als een persoonlijke conditie-trainer steeds in topvorm weten te houden met squashen, hobbelen, huizen opknappen en niet te vergeten skiën. Daar komt binnenkort misschien ook nog fietsen bij, maar ik hoop vooral dat we samen nog vele ski-reizen mogen organiseren.

Omdat ik niet 24 uur per dag met promoveren bezig wilde zijn, ben ik de volgende mensen dank verschuldigd voor de broodnodige afleiding tussendoor: de feestcommissie (Antje, Dr. Lu, Andrea en Cocktail Henkie) voor een paar knallende jaarwisselingen, de wat-voor-leden-dan-ook van Fysisch Genootschap Nwyvre voor de altijd gezellige traditionele activiteiten, de Brassers uit Maasbree voor een wat meer landelijke dekking van die afleiding, café Drieneke voor de opvang in het weekend en de sparerib-sessies, en de mensen van het (voormalige) kantineteam van M.V.C.'19 6 voor de nuttige besteding van mijn zondagmiddagen.

Mijn ouders wil ik tenslotte bedanken voor alle steun en liefde die ik altijd van hun heb gekregen en voor het feit dat ik me eigenlijk nog altijd niet heb kunnen losmaken van het plaatsje waar ik ben opgegroeid.



# Curriculum Vitae

12 juli 1973	geboren te Düsseldorf
juni 1991	diploma gymnasium, St-Thomas college te Venlo
1991-1997	Studie Technische Natuurkunde, Technische Universiteit Eindhoven, doctoraal examen februari 1997
1997-2001	Assistent-In-Opleiding bij de capaciteitsgroep Fysica en Toepassingen van Ionen-Bundels, Faculteit Technische Natuurkunde, Technische Universiteit Eindhoven
2001-	vrij man (?)